Dynamics of Functional Magnetic Microstructures

Dissertation

zur Erlangung des akademischen Grades

Doktor der Naturwissenschaften (Dr. rer. nat.)

Rasmus Bahne Holländer

Supervisor: Prof. Dr-Ing. Jeffrey McCord
Technische Fakultät
Christian-Albrechts-Universität zu Kiel

2018

1. Gutachter: Prof. Dr.-ing. Jeffrey McCord
2. Gutachter: Prof. Dr.-ing. Eckhard Quandt

Datum der mündlichen Prüfung: 13.02.2019

To *youth* and *inspiration* -
to *young inspired* people
and those *inspired* by the *young*.
May *inspiration* never die,
and make us forever *young*.

Abstract

This work is about the dynamics of functional magnetic microstructures. In the beginning it contains research on numerical modeling the motional response of superparamagnetic microbeads on top of patterned ferromagnetic surfaces. At first, an expression for the potential energy of the system is derived. After this, the details of the numerical modeling are explained, followed by a comparison to experimental data. Furthermore, a specialized microscope setup is discussed, which allows for performing stroboscopic measurements with picosecond time resolution. Based on this experimental setup the possibility of dynamic vector microscopy was investigated for the differential measurement of localized individual magnetization components. Then, switchable magnetization dynamics via magnetic domain states at zero-field is investigated. An asymmetric structure is used, which breaks the symmetry of the two remanent states by field history along the hard and easy axis of uniaxial anisotropy. In particular, the utilized specimen is investigated by pulsed inductive microwave magnetometry and dynamic magneto-optical vector microscopy. Here, switchable high-frequency properties result from local ferromagnetic resonances. The last part is then about the excitation of magnetostatic spin waves and elastic waves, visible in the dynamic magnetization. Here, a simplified two dimensional micromagnetic model is used for comparison to the high frequency experiments. The observed magnetostatic spin waves coincide for experiment and model. The experimentally observed elastic waves coincide with the phase velocity, calculated under assumption of literature values.

Zusammenfassung

Die vorliegende Arbeit beschäftigt sich mit der Dynamik von funktionellen magnetischen Mikrostrukturen. Zu Beginn handelt die Arbeit von der numerischen Modellierung superparamagnetischer Mikrokugeln und deren Bewegung auf strukturierten ferromagnetischen Oberflächen. Zunächst wird ein Ausdruck für die potentielle Gesamtenergie des Systems hergeleitet. Danach werden die Feinheiten der numerischen Modellierung erklärt, gefolgt vom Abgleich mit experimentellen Daten. Weiterhin wird ein spezialisierter Mikroskop-Aufbau besprochen, mit dem es möglich ist stroboskopische Messungen mit Pikosekundenzeitauflösung durchzuführen. Aufbauend auf diesem experimentellen Aufbau wurde die Möglichkeit der dynamischen Vektormikroskopie zur differentiellen Messung einzelner lokalisierter Magnetisierungskomponenten erforscht und dargelegt. Daraufhin wird schaltbare Magnisierungsdynamik durch magnetische Domänenzustände bei Nullfeld zu untersucht. Verwendet wird hier eine asymmetrische Struktur, die die Symmetrie der zwei remanenten Zustände durch Feldvorgeschichte entlang der harten und der weichen Achse uniaxialer Anisotropie bricht. Insbesondere wird die verwendete Schicht mit gepulster magnetischer Mikrowellen Magnetometrie und dynamischer magnetooptischer Vektormikroskopie untersucht. Hieraus ergeben sich dann über die Domänenstruktur schaltbare Hochfrequenzeigenschaften. Der letzte Teil beschäftigt sich dann mit der gezielten Anregung von magnetostatischen Spinwellen und elastischen Wellen, sichtbar in der dynamischen Magnetisierung. Hierbei wird ein vereinfachtes zweidimensionales mikromagnetisches Model zum Vergleich mit den Hochfrequenz-Experimenten verwendet. Die magnetostatischen Spinwellen sind deckungsgleich in Experiment und Modell. Die elastischen Wellen decken sich mit der Phasengeschwindigkeit, die unter Annahme von Literarturwerten zu erwarten wäre.

Contents

List of Abbreviations

AP	Aperture Plane
CDS	Canted Domain State
CPW	Coplanar Waveguide
CW-FMR	Continuous Wave - Ferromagnetic Resonance
FEM	Finite Element Method
FFT	Fast Fourier Transformation
FMR	Ferromagnetic Resonance
LLG	Landau-Lifshitz-Gilbert equation
MB	Microbead
MOKE	Magneto-Optical Kerr Effect
MSSW	Magnetostatic Surface Spin Waves
NDS	Narrow Domain State
ODE	Ordinary Differential Equation
SEM	Scanning Electron Microscopy
SPION	Superparamagnetic Iron Oxide Nanoparticle
TDR	Time-Domain Reflectometry
VNA	Vector Network Analyzer
WDS	Wide Domain State

1 Magnetization Dynamics on Different Time Scales

«The times they are a-changin'. »

Bob Dylan

Magnetization dynamics is the study of a magnetic system evolving over time. Different relevant time scales exist. By changing the time scale very different magnetic phenomena might be observed and applied. Generally, magnetic systems can exhibit dynamics on a very large time scale ($\gg 1$ s), such as domain wall creep [Middelhoek67] or effects called magnetic after-effect [Chikazumi97]. Thermally activated processes can play a role on this timescale, for example superparamagnetism [Bean59], the diffusion after-effect [Chikazumi97] or material aging processes.

On a large time scale (≈ 1 s) and in a saturated magnetization state of a ferromagnet, the magnetization may simply follow the external field stimulus in phase. A possible application of such quasistatic dynamics of magnetization is the motion of micrometer-sized superparamagnetic microbeads on ferromagnetic surfaces offering a reconfigurable platform for lab on a chip applications. Microbeads can have a functional surface, allowing for attaching and detaching of chemical and biological specimen. Programmable motion of microbeads provides the foundation for automatizing processes in biomedical applications. The one-dimensional motion of microbeads has been studied in [Ehresmann11] by moving head to head and tail to tail domain walls on a parent structure consisting of an alternating antiparallel exchange-bias pattern. Also, magnetic domain walls could be used to trap and manipulate individual yeast cells labeled by microbeads [Donolato11]. The trapping and positioning of cells has been shown in [Pivetal15]. Magnetic flow

cytometry using a focusing effect of specialized magnetic structures has been investigated in [Helou13]. Furthermore, magnetic microbeads could be used as programmable integrated micropumps using synchronized microbead motion rotating around a disk array to generate on-chip flow of aqueous solutions [Beld15]. A common phenomenon observed when using superparamagnetic microbeads is the formation of clusters of multiple microbeads. The generation and motion of such superstructures of multiple microbeads were subject to investigation in [Eickenberg13]. There are modeling approaches towards the motional response of superparamagnetic microbeads as in [Lim14], utilizing a semi-analytical approach considering the magnetic free pole density, but the all-numerical connection between micromagnetic stray field and microbead motion has not been covered so far. The advantage of such an algorithm would be the exact treatment of the micromagnetic state of the parent structure (the patterned ferromagnetic thin film) leading to quantitative simulation results. In order to investigate different magnetic parent structures and different magnetic microbeads for a controlled motional response, such a numerical algorithm was developed relying on micromagnetic simulations. The algorithm utilizes the stray field of the parent structure obtained by micromagnetic simulations. Furthermore, a spatial distribution of the superparamagnetic particles in the shell of the microbead is assumed. The external magnetic bias field and the stray-field exerted from the disk are then multiplied by the magnetization of the microbead and the product is then integrated over the volume of the magnetic shell. Using this potential energy the local potential gradients can be calculated and the equation of motion in the fluid medium can be solved. Here, the motion of the magnetic microbead around a ferromagnetic disk is driven by in-plane rotating external magnetic fields. Apart from circular motion, another regime of motion can be found, where the microbead is exhibiting a looping motion [Hu15]. The enhanced numerical modeling using micromagnetic simulations and investigation of radial looping are published in [Sajjad17]. In this work, Chapter 3 is dedicated to the numerical investigation of superparamagnetic microbead motion. In the case of microbead motion, the time scale is limited by the achievable potential gradient and the fluid damping leading to dynamics on a time scale of $\approx 1\,\mathrm{s}$.

By increasing the excitation frequency additional phenomena become relevant also magnetically. Furthermore, considering multi-domain states leads to local dynamics. Also, inductive devices may depend on the magnetization reversal mechanism. Espe-

cially domain wall displacement processes can result in high permeability. However, irregularities in the domain structure can lead to noise and higher losses as in the case of transformer sheets. Therefore, an engineering of a regular domain structure can benefit the performance of these devices. A good overview on domain structures in electrical steel is given in [Hubert08]. In the case of electrical steel (FeSi), which is used for example in transformer sheets, multiple steps can be applied in order to achieve a low loss magnetic material. For example the polycrystalline material can be grain-oriented leading to a more regular domain pattern of wide in-plane domains separated by $180°$ walls and consequently to lower losses. Also, the width of these domains can be reduced by scratching or laser scribing introducing local stresses and acting like an artificial grain boundary. Smaller domain widths then lead to reduced anomalous losses due to eddy currents, which can dominate over increased hysteretic losses at higher frequency. By changing the domain structure a control over the total losses and their frequency dependence is gained. So electrical steel can be tailored to the operating frequency by controlling the magnetic microstructures. The application relevant frequency regime of inductive transformer devices starts at $f = 50\ \mathrm{Hz}$ corresponding to a time scale of $20\ \mathrm{ms}$.

Moreover, research on magnetic materials has been ignited by the application of magnetic data storage. A possible candidate for future magnetic memory systems is the racetrack memory, which is reviewed in [Parkin08, Parkin15]. The racetrack memory relies on the injection, movement and readout of magnetic domain walls in ferromagnetic nanowires. Here, the shifting is operated by spin transfer torque due to a spin-polarized current in the ferromagnet. Furthermore, the idea of the racetrack memory involves that the nanowires can be arranged in a three dimensional array, overcoming the limitations of two dimensional data storage. Naturally, the controllable formation of magnetic microstructures is of key interest. One possibility to achieve a high domain wall speed, is to move chiral Néel walls in perpendicularly magnetized synthetic antiferromagnets as shown in [Yang15a]. These synthetic antiferromagnets consist of two ferromagnetic layers coupled antiferromagnetically via a thin Ru interlayer [Parkin90]. Perpendicular magnetic anisotropy can be reached via a dominating surface anisotropy [Aharoni96]. Furthermore, an interfacial Dzyaloshinskii-Moriya interaction [Dzyaloshinsky58, Moriya60] leads to a chirality of the domain walls. In [Yang15a] propagation velocities of $750\ \mathrm{m/s}$ were achieved on a track length of $50\ \mu\mathrm{m}$ correspond-

ing to a time-scale of $\approx 66\ \mathrm{ns}$.

Application of alternating magnetic fields to magnetic materials at even lower timescales may lead to ferromagnetic resonance phenomena. Ferromagnetic resonance is the uniform collective excitation of the spin system. Many inductive microwave devices are based on the strong absorption of microwave power at ferromagnetic resonance in a microwave cavity. Examples for magnetic microwave devices are tunable microwave filters [Cramer00, Harward14, Kuanr03, Kuanr05, Li15, Salahun02, Song09, Tsai99, Tsai05, Yang15b, Adam02], circulators [Adam02, Saib05] and phase shifters [Kuanr03, Adam02, Saib05]. By using magnetic microwave materials the relevant frequency regime can be hard and soft-tuned. Here, hard-tuning is a tuning process by an inherent material configuration, which cannot be changed post-production. Hard tuning involves the magnetic [Kuanr03] and electric geometry [Salahun02] or the deposition angle [Li15]. Soft tuning includes post-production tuning and can be reached by applying an external magnetic field [Cramer00, Harward14, Kuanr03, Salahun02, Song09, Tsai99, Tsai05, Yang15b, Adam02]. Materials used in such devices range from yttrium iron garnet (YIG) [Tsai05, Adam02] to ferrites [Harward14, Song09, Adam02] and Fe-based [Cramer00, Kuanr03, Tsai99]. Other candidates for magnetic microwave materials are amorphous alloys as $\mathrm{Co_{40}Fe_{40}B_{20}}$ offering high saturation magnetization [Herzer97] and low Gilbert damping [Oogane06]. By controlling the shape anisotropy of a micro-stripline high zero-field operation frequencies can be achieved for band-stop filters [Kuanr03]. Other devices were built utilizing the bi-stability of magnetic nanowires. In this case, different remanent states could be found by using minor-loops [Saib05, Medina10]. Changing the magnetic microstructure of a given ferromagnetic specimen can drastically change the inductive microwave response of the material. Phenomenologically this can be modeled by assuming that the material consists of areas (magnetic microstructures) with different local permeability [Schoenstein05]. Ferromagnetic microstripes exhibit shifts of the local resonance frequency by changing the width of the domains via magnetic field history [Hengst14, Queitsch06]. This phenomenon is attributed to the introduction of a domain shape anisotropy accounting for the local effective fields in a multi-domain state. It offers the possibility to tune the magneto-dynamic response at zero-field by prior application of a magnetic field history. In a device, requiring only few changes of the frequency band per unit time, this would lead to a drastic

decrease in consumed power, when compared to a device where a constant current is needed for the application of a magnetic bias field. Therefore, motivation for investigating different domain structures magneto-dynamically is to find a functional material with a high domain structure dependent shift of the ferromagnetic resonance frequency and a ferromagnetic resonance frequency close to one of the relevant frequency bands in high frequency electrical engineering. Also, a high active magnetic volume per area of the thin film would be beneficial, since the amplitude of the inductive signals scales with it. Another way to vary local effective fields is by patterning the magnetic material with antidots lattices [Cowburn98, Kaidatzis16, Heyderman06, Vavassori02, Hu11]. These exhibit a higher active magnetic volume per area of the thin film compared to single magnetic elements. Antidot lattices often show domain patterns of Néel spikes [Néel88]. Here, we tailored our magneto-dynamic response by using diamond-shaped antidots [Bhat13] in a rectangular lattice arrangement. By using field history the formed Néel spikes can either overlap along the short or long axis of the rectangular lattice. Overlapping along the short array axis then leads to the formation of a special domain structure, when the direction of the previously applied field is nearly perpendicular to the axis of uniaxial anisotropy. When the field is applied along the axis of uniaxial anisotropy, the formation of such domains is suppressed by the uniaxial anisotropy. Therefore, the energy and local effective fields of these two different domain states vary. In this way the symmetry of the magneto-dynamic response is broken for the two remanent magnetization states leading to different maximum amplitude frequencies. For switching between the two states only low magnetic fields are required in the order of $2\ \mathrm{kA/m}$. The maximum amplitude frequency could be switched from $1.3\ \mathrm{GHz}$ to $2.3\ \mathrm{GHz}$ reproducibly and close to the relevant frequency band at $2.4\ \mathrm{GHz}$. In Chapter 5 this local resonance behavior is investigated. Here, the relevant time scale is smaller than $1\ \mathrm{ns}$.

A proposal for future technology superseding modern semiconductor technology deals with the study of spin waves and their quanta *magnons*, because they provide low wavelengths, high frequencies and transfer of information without Joule-heating [Chumak15]. Spin waves can be excited in ferromagnetic materials at frequencies even higher than the ferromagnetic resonance depending on the excited mode. A promising way to control and manipulate spin waves is via the application of magnonic crystals. Magnonic crystals are artificially engineered magnetic materials with a periodic variation of magnetic prop-

erties in space. Due to the induced periodicity fundamentally different properties of the magnonic dispersion can be found such as magnonic band gaps. Reviews on magnonic crystals and spin wave technology can be found in [Serga10, Chumak15, Chumak17]. Following the treatment in [Chumak17], magnonic crystals can be used as spin wave conduits or microwaves filters. Other applications include for example magnetic field sensors [Inoue11, Atalay15] and spin wave logic gates [Khitun12, Nikitin15]. One approach to vary the local magnetic properties is to introduce reconfigurable magnetic microstructures, theoretically proposed by [Wang15]. Direct experimental evidence of this concept and a profound understanding of dynamic domain wall processes in magnonic crystals still await investigation. Functional magnetic microstructures can be applied in the field of magnonics also in different ways. Recently it has been shown that magnetic vortices can act as tunable emitter of spin waves [Wintz16]. Also, the guiding of spin waves through domain walls in a potential well due to localized effective fields [Wagner16] has been investigated. The emission of spin waves from magnetic microstructures has been subject to investigation for a long time [Winter61]. Recent studies include experiment and theory on the emission of spin waves from magnetic edges [Davies16, Lohman17, Mushenok17]. The simulation of emission of spin waves from pinned 90° symmetric Néel walls can be found in [Wiele16]. Domain walls were discussed for guiding and delimiting of spin waves [Trützschler16]. The coupling of spin waves and elastic waves is of key interest, because elastic waves exhibit much longer propagation paths. Propagating coupled magneto-elastic waves could be found in theory by tailoring a modulated magnetic and elastic structure with two materials [Graczyk17]. Also, the excitation of spin waves by strain was investigated by solving elastodynamic equations and Landau-Lifshitz-Gilbert equation in [Chen17]. Furthermore, it was shown that elastic waves or Surface acoustic waves (SAW) can excite local magnetization dynamics of magnetic microstructures [Foerster17]. Direct experimental evidence of spin wave emission by magnetic domain walls is sparsely researched [Mozooni15]. In this work, the emission of magneto-static spin waves and elastic waves is investigated experimentally and by micromagnetic simulation. The emission of elastic waves from vibrating 180° domain walls has been handled theoretically in [Lord67] for MHz-frequencies. Here, direct experimental evidence of elastic wave emission by magnetic domain walls is provided in the high MHz and GHz-regime. The results on the emission of spin waves and elastic waves by homogeneous excitation of magnetic

domain walls have been published in [Holländer18]. For the spin waves subject to this work the relevant time scale could be shorter than $100\ \mathrm{ps}$.

In order to measure such phenomena of the magnetic microstructure as described, powerful techniques are needed. Depending on the size of the magnetic microstructures, different characterization techniques can be applied. Static magneto-optical wide-field imaging is a versatile technique to measure the local magnetization distribution. A more complete review on the state of the art of magneto-optical domain imaging can be found in [McCord15]. Other techniques for the investigation of magnetic domain structure include scanning electron microscopy with polarization analysis (SEMPA) [Scheinfein90, Pierce11], Lorentz transmission electron microscopy (LTEM) [Chapman83, Chapman90] or synchrotron X-ray microscopy [Kim01]. Here, magneto-optical imaging is used, because it is feasible to apply magnetic fields to the specimen, there is no need for vacuum and no need for special sample preparation such as a deposition on a membrane. Also, magneto-optical imaging is low-cost, when compared to synchrotron radiation and although it does not offer a comparable spatial resolution, the optically achieved time resolution is excellent ($7.2\ \mathrm{ps}$). A typical time resolution of synchrotron based x-ray sources is $50\ \mathrm{ps}$ [Fischer15, Bonetti15]. In dynamic wide-field magneto-optical measurements at high frequencies, the magnetization precesses around the axis of the effective field. This leads to a non-negligible out-of-plane contrast even appearing in the longitudinal configuration (oblique incidence). This problem is solved is addressed and solved in Chapter 4. As a result the quantitative in-plane magnetization response can be obtained. The results on the component-selective imaging process are published in [Holländer17].

The time scale changes the physical phenomena we observe. The field of magnetization dynamics offers many possibilities for new evolving technologies. All in all, the famous musician and Nobel-prize winner Bob Dylan was right: The times are changing. Not only on a sociological level, but also new technologies arise and evolve over time.

.

2 Fundamentals

In 1935 *Landau and Lifshitz* published a profound work containing fundamental concepts about the calculation of magnetic microstructures [Landau35]: Instead of following an atomistic approach, they used the continuum limit of a magnetic material, in which a minimization of the total energy of the system would lead to the equilibrium domain configuration. Later on, this concept would be called *micromagnetics* [Brown59]. Moreover, in the same publication they introduced the nowadays called Landau-Lifshitz-Equation and the necessary effective magnetic field in the material. However, the proposed damping mechanism in the Landau-Lifshitz equation could not account for large non-eddy-current damping in thin Permalloy sheets, therefore a different damping term was introduced by *Gilbert* [Gilbert04] leading to the Landau-Lifshitz-Gilbert equation. Today investigating phenomena of the magnetic microstructure as magnetic domain state, domain wall configuration or demagnetization effects at the edges is as well a study of the magnetization state and the local effective magnetic field. Relying on the same principles as the early work of *Landau and Lifshitz*, it is suitable today, to apply numerical micromagnetic software as for example OOMMF [Donahue99], mumax^3 [Vansteenkiste14] or micromagus [Berkov93] to understand domain structures and their time-dependent magnetic processes. Most measurements and domain imaging techniques are not sensitive to the inner domain and domain wall structure. Therefore, micromagnetic simulations are useful to obtain information about the magnetization distribution inside the ferromagnetic body. In this chapter, the necessary energy terms for the calculations of magnetic microstructures in a micromagnetic code are discussed. Example calculations concerning the demagnetization effect, domain configuration and different domain walls are brought into context with the effective field. Then the connection between local effective fields and magnetization dynamics is discussed introducing ferromagnetic resonance and spin waves. At the end of the chapter a brief introduction to superparamagnetism is given.

2.1 Introduction to Micromagnetics

The study of ferromagnetic materials naturally involves the study of the local magnetization distribution and the inherent reversal mechanisms. In order to minimize its own energy, a ferromagnetic material can form *magnetic domains*, which are volumes of homogeneous magnetization. These domains are separated from each other by forming domain walls, small volumes, in which the magnetization rotates continuously. Magnetic domains and domain walls can be summarized under the term *magnetic microstructures*. In order to study the formation of magnetic microstructures, knowledge about the energy of the ferromagnetic system is required. The micromagnetic energy density of a ferromagnetic material can be written as a sum of different contributions [Hubert08]

$$e_{\mathrm{tot}} = e_{\mathrm{exchange}} + e_{\mathrm{anisotropy}} + e_{\mathrm{Zeeman}} + e_{\mathrm{magnetostatic}} + e_{\mathrm{magnetoelastic}}. \tag{2.1}$$

Here, e_{tot} denotes the total magnetic energy density, while the contributions are named according to their source of contribution, i.e. e_{exchange} is the contribution of the exchange interaction to the overall energy density, $e_{\mathrm{anisotropy}}$ is the anisotropy contribution, e_{Zeeman} the Zeeman-energy contribution, $e_{\mathrm{magnetostatic}}$ the magnetostatic contribution and $e_{\mathrm{magnetoelastic}}$ the magnetoelastic contribution to the total energy density. Here, energy densities are given, therefore the total energy E_{tot} is given by

$$E_{\mathrm{tot}} = \int_{V'} dV e_{\mathrm{tot}}(\mathbf{x}), \tag{2.2}$$

where e_{tot} is a function of the position $\mathbf{x}$ in the volume V' of the ferromagnetic body. Throughout this work vector quantities will be written in **bold** font. In general, the energy densities are a function of the position inside the ferromagnetic body, because the magnetization orientation varies throughout the magnetic specimens. However, the microscopically viewed absolute value of local magnetization does not change at constant temperature and therefore the normalized magnetization is written

$$\mathbf{m}(\mathbf{x}) = \frac{\mathbf{M}(\mathbf{x})}{M_{\mathrm{s}}}. \tag{2.3}$$

Here, $\mathbf{M}(\mathbf{x})$ is the local volume magnetization, M_s the saturation magnetization of the material and $\mathbf{m}(\mathbf{x})$ is the locally normalized magnetization. In order to obtain the spatially resolved magnetization distribution, the ferromagnetic body can be subdivided into multiple discrete cells each representing a local magnetization orientation. The subdivision can be performed with rectangular cells in finite difference algorithms such as mumax^3 [Vansteenkiste14] or micromagus [Berkov93] or triangular cells in finite element algorithms such as magnum.fe [Abert13]. For the presented work micromagus and mumax^3 were used, therefore the focus will be solely on these. The individual cell size of the subdivision should be chosen in the size of the exchange length

$$l_\mathrm{ex} = \sqrt{\frac{A}{K_i}}, \tag{2.4}$$

where A is the exchange stiffness constant and K_i is the value of the dominating anisotropy [Abo13]. By discretizing the ferromagnetic body, also the equations and boundary conditions of the individual cells become discrete. Then, from the corresponding discrete set of equations, the energetic minimum can be found numerically by a range of algorithms, such as the *Runge-Kutta-method*. Furthermore, the derivative of the energy density gives rise to the **effective magnetic field** [Pechan01, Fidler00, Landau35]

$$\mathbf{H}^\mathrm{eff} = -\frac{1}{\mu_0 M_\mathrm{s}} \nabla_\mathbf{m} e_\mathrm{tot}, \tag{2.5}$$

where μ_0 is the vacuum permeability, M_s is the saturation magnetization of the material and $\nabla_\mathbf{m}$ denotes the gradient with respect to $\mathbf{m}$. In general, the effective magnetic field depends on the position $\mathbf{x}$ in the ferromagnetic body, as well. Magnetic boundaries such as edges, surfaces and domain walls lead to local effective fields. In the following, the individual contributions to the total energy density and the effective magnetic field will be discussed.

2.1.1 Exchange Interaction

The crucial energy and effective field contribution for the existence of ordered magnetism (i.e. ferromagnetism, ferrimagnetism, antiferromagnetism) is the exchange interaction. It is of quantum mechanical nature. For the direct exchange (or Heisenberg exchange)

the electron-electron interaction can either favor parallel orientation of electron spins for ferromagnetism or antiparallel orientation for antiferromagnetism. This description is limited to direct exchange interaction. There are more mechanisms for the exchange interaction such as super exchange in oxides, indirect exchange for materials with partially filled f-orbitals and itinerant exchange for metals. However, these mechanisms exceed the scope of this work. The so-called Heisenberg-Hamiltonian $H_{\mathrm{Heisenberg}}$ expresses, that the spin-dependent energy of the Pauli exclusion principle can be written in a vector-model [O'Handley00, Aharoni96]

$$H_{\mathrm{Heisenberg}} = -\sum_{i \neq j} J_{ij} \mathbf{S}_i \cdot \mathbf{S}_j, \tag{2.6}$$

where $\mathbf{S}_i$ and $\mathbf{S}_j$ correspond to the spins at different atomic sites and J_{ij} is the exchange integral between atoms i and j. Then, J_{ij} is assumed to be different from zero only between the nearest neighbors $J = J_{12}$. If $J > 0$, parallel alignment of spins is favored (ferromagnetism), if $J < 0$, antiparallel alignment is preferred (antiferromagnetism). In macroscopic calculations the exchange energy can be approximated by classical spin-vectors

$$E_{\mathrm{exchange}} = -JS^2 \sum_{\mathrm{neighbors}} \cos\varphi_{i,j} \approx JS^2 \sum_{\mathrm{neighbors}} \varphi_{i,j}^2 + \mathrm{constant}. \tag{2.7}$$

Here, S is the expectation value of the spin and $\varphi_{i,j}$ is the angle between the classical spin-vectors. In the last step, a small-angle approximation is performed, which is valid since the exchange interaction is strong compared to the other remaining energy contributions, so that small angles are favored in the ferromagnetic case. Another small angle approximation and subsequent Taylor series then yields

$$|\varphi_{i,j}| \approx |\mathbf{m}_i - \mathbf{m}_j| \approx |(\mathbf{s}_i \cdot \nabla)\mathbf{m}|, \tag{2.8}$$

where $\mathbf{m}$ corresponds to a unit vector parallel to the local spin direction and $\mathbf{s}_i$ is the position vector from lattice point i to j. Substituting and changing the summation to an integral in the fashion of Eq. 2.2 then leads to the exchange energy density [Hubert08,

Aharoni96, O'Handley00]

$$e_{\text{exchange}} = A\left[(\nabla m_x)^2 + (\nabla m_y)^2 + (\nabla m_z)^2\right]. \tag{2.9}$$

In this expression m_x, m_y, m_z are the components of the normalized magnetization $\mathbf{m}$ and $A = JS^2n/a$ is the exchange stiffness constant with a being the distance between nearest neighbors and n a constant depending on the crystal structure. More details on this derivation can be found in [Aharoni96] and [O'Handley00]. Eq. 2.9 is the form of exchange energy utilized in micromagus [Berkov93] and mumax^3 [Vansteenkiste14]. In order to obtain valid results from the micromagnetic simulation, an appropriate value of A is needed for the specific material.

2.1.2 Anisotropy Contribution

The Heisenberg-Hamiltonian and the resulting exchange interaction is isotropic in nature, but generally magnetic materials exhibit an anisotropic magnetization contribution. For single crystals the magnetocrystalline anisotropy originating from spin-orbit coupling is a common mechanism of anisotropy. Depending on the crystal structure the anisotropy of single crystals can either be cubic or uniaxial. Further mechanisms are stress-induced anisotropy mediated by the magnetoelastic effect, shape anisotropy by the magnetostatic energy, exchange bias induced by adjacent antiferromagnetic layers, surface anisotropy in very thin films originating in the broken symmetry on the interface to another material and magnetization induced anisotropy in amorphous or polycrystalline materials. Sputtered amorphous alloys as $(\mathrm{Fe_{90}Co_{10}})_{78}\mathrm{Si_{12}B_{10}}$ or $\mathrm{Co_{40}Fe_{40}B_{20}}$ exhibit a uniaxial magnetization induced anisotropy either homogeneously aligned along one axis by a magnetic field applied during deposition or inhomogeneously aligned due to the magnetostatic interaction. If the magnetization was not aligned during deposition, the magnetic sample can still be heated and field-cooled ex-situ after the deposition. Also, the deposition angle contributes to the alignment of anisotropy. Polycrystalline Permalloy can as well exhibit a very small uniaxial induced anisotropy. Throughout this work only materials exhibiting uniaxial anisotropy will be used, i.e. polycrystalline Permalloy and amorphous alloys. The corresponding anisotropy energy can be written as [Aharoni96]

$$e_{\text{anisotropy}} = -K_{\text{u}}(\mathbf{c}\cdot\mathbf{m})^2, \tag{2.10}$$

where K_u is a constant determining the magnitude of the anisotropy, $\mathbf{c}$ is a unit vector parallel to the easy axis of magnetization and $\mathbf{m}$ is the unit vector along the magnetization direction. Higher order terms of uniaxial anisotropy are not shown here, because they were neglected for the simulations in this work. By combining Eq. 2.5 and Eq. 2.10 an effective anisotropy field can be calculated as

$$\mathbf{H}^{\mathrm{eff}}_{\mathrm{anisotropy}} = -\frac{1}{\mu_0 M_\mathrm{s}} \nabla_{\mathbf{m}} e_{\mathrm{anisotropy}} = \frac{2K_\mathrm{u}}{\mu_0 M_\mathrm{s}} (\mathbf{c} \cdot \mathbf{m})\mathbf{c} \tag{2.11}$$

In a macrospin model the necessary field to completely switch the magnetization along the easy axis (and hard axis) of magnetization is then the anisotropy field [Stoner48]

$$H_k = \frac{2K_\mathrm{u}}{\mu_0 M_\mathrm{s}}. \tag{2.12}$$

For this macrospin model, also the Zeeman contribution is required (see next Section).

2.1.3 Zeeman Contribution

Another contribution is the Zeeman energy. It favors an alignment of the magnetization parallel to the external magnetic field $\mathbf{H}$ and can be written locally as

$$e_{\mathrm{Zeeman}} = -\mu_0 M_\mathrm{s} \mathbf{H} \cdot \mathbf{m}. \tag{2.13}$$

2.1.4 Magnetostatic Contribution

The magnetostatic contribution largely depends on the demagnetizing field $\mathbf{H}_\mathrm{d}$, also called the magnetic stray field outside of the material. Inside the ferromagnetic body, the demagnetizing field is proportional to the density of free magnetic poles on the surface and points into the opposite direction of the magnetization. The magnetostatic energy density is then

$$e_{\mathrm{magnetostatic}} = -\frac{\mu_0 M_\mathrm{s}}{2} \mathbf{H}_\mathrm{d} \cdot \mathbf{m}. \tag{2.14}$$

Since the demagnetizing field and the magnetization have opposite signs, the magnetostatic energy density is always positive. In conclusion, the demagnetizing field should be minimized, possibly avoiding any free poles on the surface of the ferromagnetic

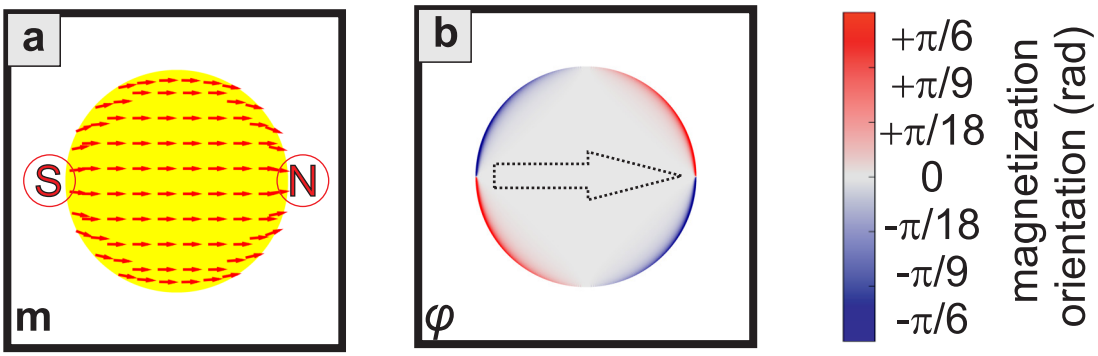

Figure 2.1: Magnetization state of a 30 nm thin magnetic Permalloy disk with a diameter of 30 μm at an external field of 16 kA/m. a) Vector representation of the magnetization: Red arrows indicate the local magnetization. S indicates the magnetic south pole, N the magnetic north pole. b) Azimuthal magnetization angle φ representation. Both representations indicate a bending of the local magnetization at the edges towards the magnetic poles. This local bending occurs due to the high demagnetizing field at the edges. This figure was adapted from [Sajjad17].

body. This is called *pole-avoidance principle* [Aharoni96]. Due to this concept, the magnetostatic contribution highly depends on the shape of the ferromagnetic body and can even give rise to a shape anisotropy for asymmetric bodies. In order to demonstrate the effect of the magnetostatic energy, the magnetization configuration of a Permalloy disk is calculated using mumax^3 and depicted in Fig. 2.1. The disk has a diameter of 30 μm and a thickness of 30 nm. The exchange stiffness constant is $A = 13$ pJ/m, the applied external field 16 KA/m along x-direction, the saturation magnetization $M_s = 800$ kA/m and the uniaxial anisotropy is neglected, because it is small compared to the external magnetic field. For the finite differences calculation, the grid was set to $1700 \times 1700 \times 3$ cells with a cellsize of $dx \times dy \times dz = 18 \times 18 \times 10$ nm^3. Fig. 2.1a shows the magnetization state in a vector plot. It can be seen, that the magnetization in the middle of the ferromagnetic body aligns along the external magnetic field. More close to the edges, however, the demagnetizing energy leads to a local magnetization orientation almost parallel to the surface in order to avoid free poles on the surface. In Fig. 2.1b the

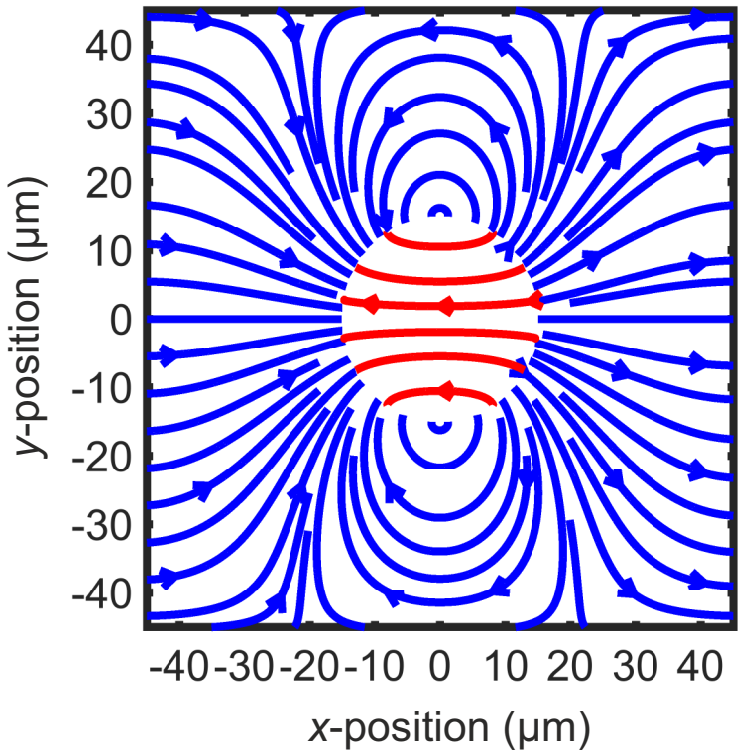

Figure 2.2: Field line representation of the micromagnetic stray field directly on top of a $30\ \mathrm{nm}$ thin magnetic Permalloy disk with a diameter of $30\ \mu\mathrm{m}$ at an external field of $16\ \mathrm{kA/m}$ (compare Fig. 2.1). The blue field lines indicate the stray field outside of the ferromagnetic material, the red lines indicate the internal demagnetizing field on the outermost ferromagnetic layer. The density of red and blue field lines is not to scale.

in-plane magnetization orientation φ is depicted in a color plot. It is evident that the local reorientation of magnetization due to the demagnetizing field happens only in a very narrow region next to the surface. Outside of the ferromagnetic body the magnetic stray field closes the flux of the free magnetic poles. Fig. 2.2 displays the in-plane magnetic stray field inside and outside, in the top most layer of the ferromagnetic disk (compare Fig. 2.1). Inside of the material the red field lines are aligned almost antiparallel to the direction of the external field (along positive x-direction), while outside the blue field lines close the flux of the surface poles. The density of the magnetic field lines increases close to the magnetic north and south pole of the ferromagnetic disc, since

the ferromagnetic material concentrates the flux. The density of red and blue field lines is not to scale. In a micromagnetic code, the magnetostatic contribution is often the complicated part to implement, because in principle each reorientation of magnetization in only a single cell demands a change in local demagnetization fields for all other cells. Therefore, the calculation of local demagnetization fields is the computationally most exhaustive part of micromagnetic simulations [Berkov93].

2.1.5 Magnetoelastic Contribution

Generally ferromagnetic materials exhibit also *magnetostriction*, i.e. if the magnetization orientation changes, the strain and stress state of the ferromagnetic material also changes. Therefore, the elastic energy is also subject to change by magnetization reorientation. The free magnetostrictive deformation of an isotropic material can be written as [Hubert08]

$$\epsilon_{ik}^0 = \frac{3}{2}\lambda_s(m_i m_k - \frac{1}{3}\delta_{ik}). \tag{2.15}$$

Here, ϵ_{ik}^0 denotes the tensor components of the free magnetostrictive deformation, λ_s is the saturation magnetostriction, m_i, m_k are the corresponding magnetization components and δ_{ik} is the Kronecker delta. Then, the magnetoelastic energy contribution can be written as [Hubert08]

$$e_{\text{magnetoelastic}} = \frac{1}{2}(\mathbf{p}_e - \epsilon^0)\mathbf{c}(\mathbf{p}_e - \epsilon^0), \tag{2.16}$$

where $\mathbf{p}_e$ is the tensor of elastic distortion, $\mathbf{c}$ is the elastic stiffness tensor and ϵ^0 is the full free magnetostrictive deformation tensor. Most micromagnetic codes ignore the presence of magnetostriction in ferromagnetic materials, since it is not as relevant as other contributions for basic micromagnetic problems. A micromagnetic approach using a mechanically coupled model is presented in [Liang14]. Furthermore, the concept of calculating the actual distortion in an iterative process needs an additional computationally exhaustive routine: Changing the local magnetization varies the local elastic energy and vice versa.

2.2 Magnetic Domain Walls

Domain walls are natural boundaries dividing the spatial magnetization distribution into volumes of locally homogeneous magnetization orientation, magnetic domains (see Section 2.3). In order to minimize the total energy of the system, ferromagnetic materials form magnetic domains. The formation of abrupt jumps of magnetization, however, would increase the exchange energy drastically. Therefore magnetic domain walls form, in which the magnetization changes continuously. Moreover magnetic domain walls can have a complicated structure, whereas the structure crucially depends on the local energy density contributions. The most simple domain walls are the one dimensional symmetric 180° Bloch and Néel walls, which both can be written as a function of the spatial coordinates x, y and z in the form [Aharoni96]

$$\begin{aligned} m_x &= \frac{q^2 \cos\phi}{q^2 + y^2}, \\ m_y &= \frac{y\sqrt{2q^2 + y^2}}{q^2 + y^2}, \\ m_z &= \frac{q^2 \sin\phi}{q^2 + y^2}. \end{aligned} \tag{2.17}$$

Here, q denotes an adjustable parameter, determining the width of the domain wall, ϕ is an additional parameter changing from Bloch to Néel type and vice versa: In the case of $\phi = 0$ Eq. 2.17 describes the symmetric Néel wall and in the case of $\phi = \pi/2$ the symmetric Bloch wall, both at a position of $y = 0$. Fig. 2.3 displays the one dimensional symmetric domain walls. Here, the same q was used in order to fit both domain walls into one figure. The symmetric Bloch wall is depicted in Fig. 2.3a. As shown, in the Bloch wall case, the magnetization orientation rotates out of the film plane, creating a surface charge. Therefore the symmetric Bloch wall occurs only in Bulk materials, not in magnetic thin films. Fig. 2.3b exhibits the case of the symmetric 180° Néel wall, where the magnetization rotates in the film plane. Symmetric Néel walls can be found in very thin magnetic films, also depending on the wall angle: In [Hubert08] phase diagrams are shown for this purpose, however these diagrams should be handled with care since their resolution is also determined by the computing power of the date of creation.

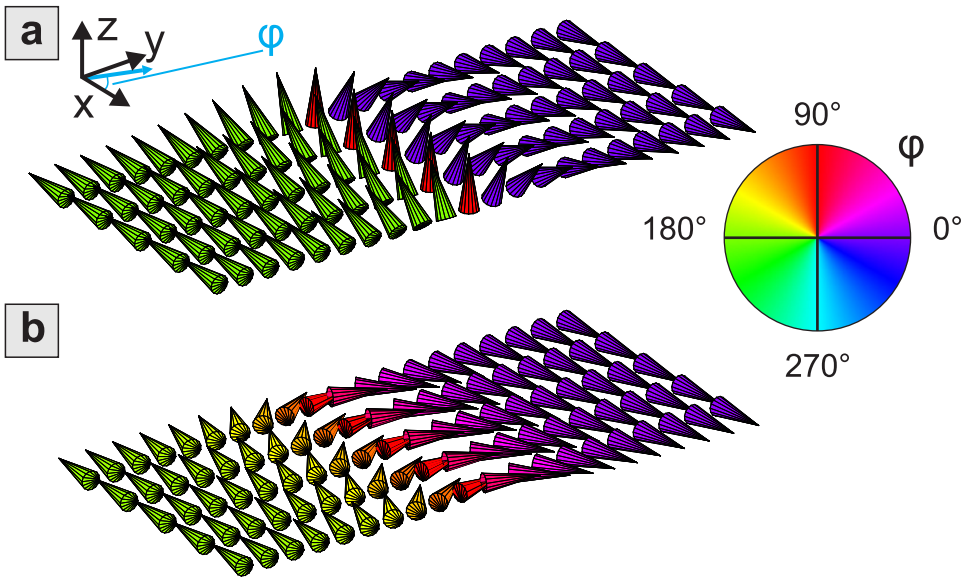

Figure 2.3: Symmetric 180° walls shown as a cone plot. The color scale represents the in-plane azimuthal magnetization angle φ. a) Symmetric Bloch wall: The magnetic moment rotates outside the film plane (x-y-plane). b) Symmetric Néel wall: The magnetic moment rotates inside the film plane (x-y-plane).

By allowing a two-dimensional magnetization distribution over the thickness of an magnetic thin film, the asymmetric Bloch and asymmetric Néel domain walls can be found. There are analytical approaches towards finding an expression for these two dimensional domain walls [Hubert69], however, calculating the exact solution numerically is more convenient and more reliable close to domain wall transitions. In Fig. 2.4 numerically simulated asymmetric Bloch and Néel walls are depicted. To simulate the asymmetric walls, a grid of $1 \times 12500 \times 30$ cells with periodic boundary conditions along x and y-axis was chosen with a cell size of $dx \times dy \times dz = 4 \times 4 \times 4\,\mathrm{nm}^3$. The parameters were chosen in accordance with material parameters for amorphous $Co_{40}Fe_{40}B_{20}$: the exchange stiffness constant $A = 15\ \frac{\mathrm{pJ}}{\mathrm{m}}$ [Conca13], the saturation magnetization $M_s = 1200\ \frac{\mathrm{kA}}{\mathrm{m}}$ and an uniaxial anisotropy of $K_\mathrm{u} = 1300\ \frac{\mathrm{J}}{\mathrm{m}^3}$ along the x-direction. In order to fulfill the periodic boundary conditions, a pair of two domain walls was calculated. Fig. 2.4a shows the magnetization components of a calculated

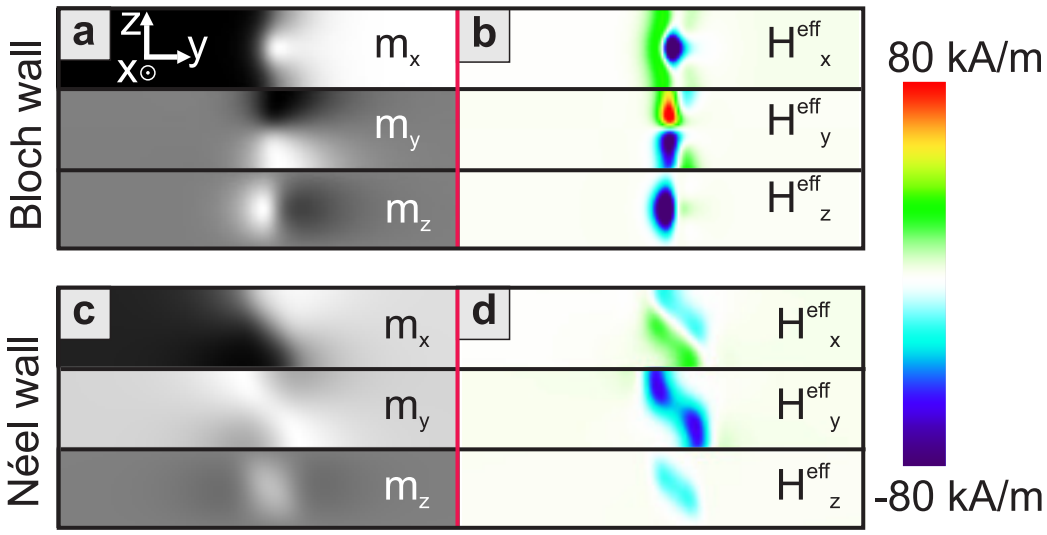

Figure 2.4: Asymmetric domain walls depicted in a cross section through the film plane (domain wall $\parallel$ x-direction, depicted in y-z-plane). a) Magnetization components of a $180°$ asymmetric Bloch Wall. b) Effective field in the same $180°$ asymmetric Bloch wall. c) Magnetization components of a $95°$ asymmetric Néel Wall. d) Effective field in the same $95°$ asymmetric Néel wall.

asymmetric Bloch wall. The film is the $x-y-$plane, the cross section is shown. It is directly evident, that the wall structure is not at all homogeneous along the z-axis. This is due to varying demagnetization fields on the film surface compared to the inside of the material. In Fig. 2.4b the local effective fields of the same asymmetric Bloch wall are plotted. It can be seen here, that the distribution of effective field is similar to the magnetization pattern. Furthermore, the local effective fields inside the domain walls reach values as high as $80\ \frac{\mathrm{kA}}{\mathrm{m}}$. This is a quite high value, especially when thinking about the spatial extent of the domain wall being only a few hundred nanometers. A similar behavior can be seen for the asymmetric Néel wall, exhibited in Fig. 2.4c in magnetization and in Fig. 2.4d as local effective field. The simulation of the asymmetric Néel wall was performed by using the same parameter set as in the asymmetric Bloch wall calculation but applying a small bias field of $640\ \frac{\mathrm{A}}{\mathrm{m}}$ along the y-axis, hereby reducing the wall angle from $180°$ to $95°$. Detailed phase diagrams showing the wall transitions can be found in [Hubert08]. Also, for a three-dimensional magnetization distribution, the so called cross-tie wall can arise, this wall will be handled in Section 2.3.

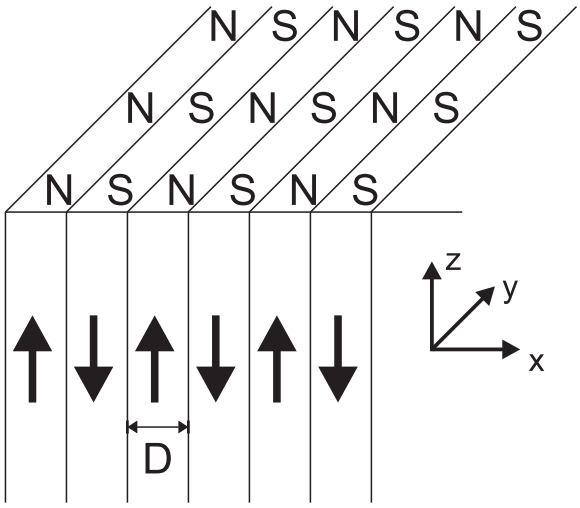

Figure 2.5: Schematic periodic domain pattern with domain width D. A ferromagnetic body with a surface at $z = 0$ is assumed, which is divided into plate-like domains separated by 180°-walls parallel to the y-z-plane. The ferromagnetic body is assumed to extend infinitely along $-z$, $\pm x$ and $\pm y$. Figure created according to [Chikazumi97].

2.3 Magnetic Domains

The formation of magnetic domain walls increases the exchange energy, since the exchange contribution favors parallel alignment of the local magnetization and the magnetization distribution inside the domain walls is far from parallel (see Section 2.1.1). Also, the formation of a domain wall increases the anisotropy energy. However, by subdivision into magnetic domains the ferromagnetic body decreases its magnetostatic energy, therefore the number and size distribution of magnetic domains usually is an interplay of these energy contributions. In Fig. 2.5 a schematic is presented showing an infinitely extended array of domains along the z-axis, separated by 180°-walls and having only one surface at $z = 0$. In such a geometry, it can be calculated that the magnetostatic energy scales proportional with the domain width $\propto D$ [Chikazumi97, Kittel49]. So, by doubling the number of domains, the magnetostatic energy halves. The presented model of infinitely many plate-like domains is simplified. It neglects the domain wall structure and is only applicable for high anisotropy materials. The closure domains form at the edge of a sample to further decrease the magnetostatic energy. In Fig. 2.6 a typical magnetization configuration for a rectangular prism is shown. The prism was

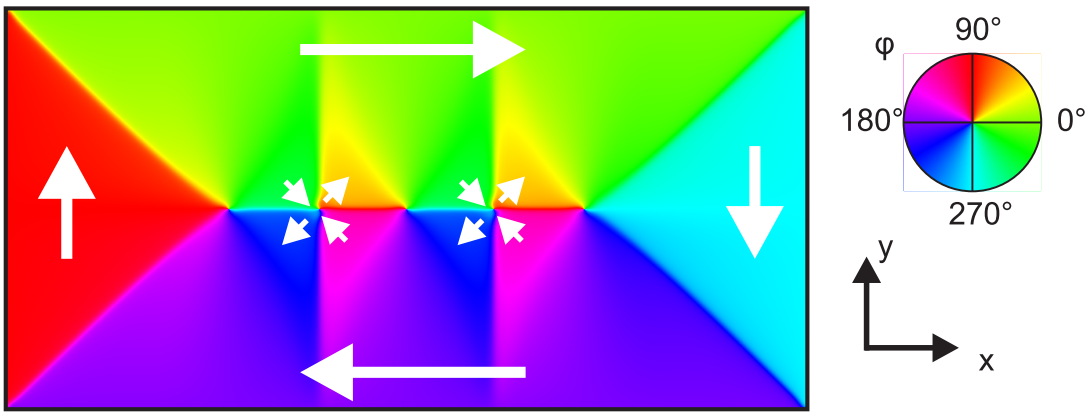

Figure 2.6: Domain state of a $4096 \times 2048 \times 48\ \mathrm{nm}^3$ sized rectangular prism at zero-field. The magnetization in the domains is oriented parallel to the surface to minimize the magnetostatic energy. In the middle of the specimen a cross-tie-wall was formed.

$4096 \times 2048 \times 48\ \mathrm{nm}^3$ big with a cell size of $4 \times 4 \times 4\ \mathrm{nm}^3$, and was calculated for amorphous $\mathrm{Co_{40}Fe_{40}B_{20}}$ using the following parameter set: exchange stiffness $A = 15\ \mathrm{pJ/m}$ [Conca13], a (low) uniaxial anisotropy of $K_\mathrm{u} = 1300\ \mathrm{J/m^3}$ along the x-axis and a saturation magnetization $M_\mathrm{s} = 1200\ \mathrm{kA/m}$. As can be seen from Fig. 2.6, the ferromagnetic body forms closure domains at the left and right edges in order to minimize the magnetostatic energy by closing the flux in the high-permeable magnetic material instead of creating more additional stray-field. Furthermore, in the middle of the specimen a 180°-cross-tie-wall is formed. As mentioned in Section 2.2 three-dimensional simulations are needed for this wall. Cross-tie-walls are yet another kind of «domain wall». They are formed in magnetic thin films in a thickness regime, where the 180° Néel wall is energetically unfavorable compared to generating multiple 90° Néel walls, vortices and antivortices [Hubert08]. Therefore, the cross-tie wall is basically an ensemble of multiple domains and domain walls. At last, the magnetic domain structure largely depends on the magnetic history, i.e. the initial magnetization and field directions determine in which energetic minimum the final magnetization will reside.

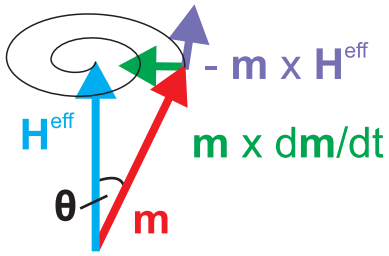

Figure 2.7: Illustration of the step response for a single domain particle and the fundamental dynamics governed by the Landau-Lifshitz-Gilbert equation: The LLG describes a damped precession of the magnetization vector around the effective field.

2.4 Magnetization Dynamics

Up to this Section only quasi-static processes were involved, i.e. the ferromagnetic body has enough time to relax into a new equilibrium after application of a new magnetic field. By exciting the ferromagnetic material with signals, which are faster than or equally fast as the intrinsic relaxation time of the material, additional dynamic processes get involved. In this dynamic regime the fundamental Landau-Lifshitz-Gilbert (LLG) equation becomes important [Gilbert04] describing the time evolution of the magnetization vector

$$\frac{d\mathbf{m}}{dt} = -\gamma\mu_0\mathbf{m} \times \mathbf{H}^{\text{eff}} + \alpha\mathbf{m} \times \frac{d\mathbf{m}}{dt}, \tag{2.18}$$

where α is the Gilbert damping, γ the gyromagnetic ratio, t is the time and μ_0 the vacuum permeability. The LLG is valid locally and can be integrated numerically using a micromagnetic software such as mumax^3 [Vansteenkiste14] or micromagus [Berkov93] in order to gain time-dependent information on the magnetization evolution. The solution to the discrete field step response for a single domain particle is a damped precession of the magnetization and illustrated in Fig. 2.7. Details on the derivation can be found in [Stancil09]. The first cross product of the LLG (Eq. 2.18) describes the precession around the effective magnetic field, while the second cross product describes a restoring torque to the equilibrium, where $\mathbf{m} \parallel \mathbf{H}^{\text{eff}}$. For a non-uniform magnetization distribution the simple picture of a damped precession is not completely applicable anymore. However,

by revisiting the static magnetization configuration shown in Fig. 2.1, it is directly clear, that even though the material is saturated (at least as far as saturating a finite magnetic material is possible), dynamically there would be additional contributions from the edges as a small correction to the uniform solution.

Subsequently two basic dynamic processes will be discussed for the case of a single domain ferromagnetic material, where analytical solutions of the LLG are possible: Ferromagnetic resonance and spin waves.

2.4.1 Ferromagnetic Resonance

While the step response of a soft ferromagnetic material with sufficiently low damping will yield an underdamped precession on the eigenfrequency, the ferromagnetic material can also be driven into *ferromagnetic resonance* (FMR). Analogue to mechanic oscillations, by using an alternating magnetic field of the right frequency, the ferromagnetic precession can be driven into resonance. Assuming a ferromagnetic material with a sufficiently low damping α, a saturation magnetization M_s, an anisotropy field H_k and an external magnetic field H parallel to the easy anisotropy axis and assuming a small excitation field perpendicular to the single domain magnetization orientation with angular frequency ω, the dynamic susceptibility χ_{yy} of a ferromagnetic thin film can be written as [Sun02]

$$\chi_{yy}(\omega) = \frac{M_\mathrm{s}^2 + M_\mathrm{s}(H_\mathrm{k} + H) + \frac{i\omega\alpha M_\mathrm{s}}{\gamma\mu_0}}{M_\mathrm{s}(H_\mathrm{k} + H) + \frac{i\omega\alpha M_\mathrm{s}}{\gamma\mu_0} - \frac{\omega^2}{(\gamma\mu_0)^2}}. \tag{2.19}$$

Here, the ferromagnetic material is saturated in the sample plane parallel to the axis of uniaxial anisotropy along the x-axis and the continuous wave excitation is aligned in the sample plane perpendicular to the axis of uniaxial anisotropy (along the y-axis). In Fig. 2.8 this complex dynamic susceptibility is depicted for a $\mathrm{Co_{40}Fe_{40}B_{20}}$-parameter set: saturation Magnetization $M_\mathrm{s} = 1200\ \mathrm{kA/m}$, anisotropy field $H_\mathrm{k} = 1700\ \mathrm{A/m}$, absolute external field $|\mathbf{H}| = H = 2000\ \mathrm{A/m}$ and Gilbert damping $\alpha = 0.008$. Fig. 2.8 shows two representations of this complex susceptibility, real and imaginary part or magnitude and phase, respectively. It can be seen directly, that the real part of the susceptibility starts off positively as expected for a ferromagnetic material, crosses zero and converges to zero at high frequencies. The zero crossing of the real part coincides with the maximum phase

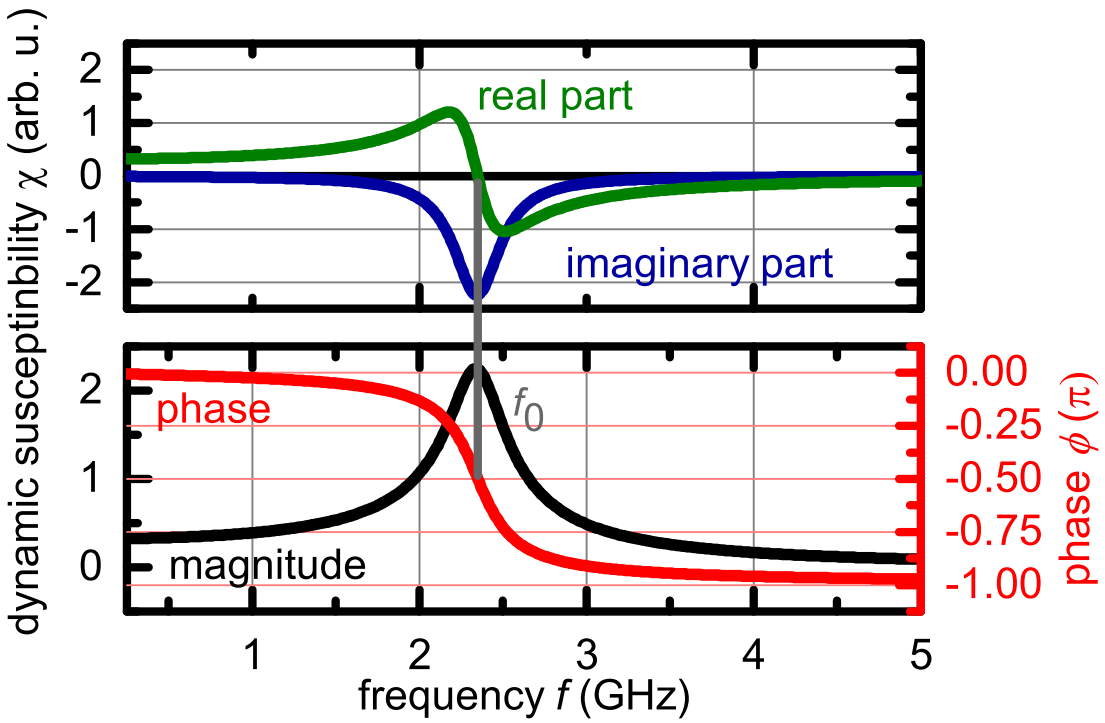

Figure 2.8: Dynamic susceptibility spectrum of a ferromagnetic material: The resonance frequency is reached at the zero crossing of the real part or when the phase reaches $-\pi/2$, respectively.

slope at $\phi = -\pi/2$ and marks the resonance frequency of the ferromagnetic material. Furthermore, the resonance frequency is approximately marked by the maximum of the magnitude and the minimum of the imaginary part. However, as pointed out in [Sun02], the maximum of magnitude and minimum of imaginary part coincide, as well do the zero-crossing of the real part and the frequency point were $\phi = -\pi/2$, but the zero-crossing frequency and maximum of magnitude can be different from each other depending on the magnitude of the Gilbert damping. In the absence of damping, the FMR frequency f_0 is given by [Kittel48]

$$f_0 = \frac{\mu_0 \gamma}{2\pi} \sqrt{[M_\mathrm{s}(N_z - N_x) + H_k + H]\,[M_\mathrm{s}(N_x - N_y) + H_k + H]}. \tag{2.20}$$

In this equation N_x, N_y, N_z denote the components of the demagnetization tensor. For a

thin full film they can be approximated by $N_x \approx 0$, $N_y \approx 0$, $N_z \approx 1$ leading to

$$f_0 \approx \frac{\mu_0 \gamma}{2\pi} \sqrt{[M_\mathrm{s} + H_k + H]\,[H_k + H]}. \tag{2.21}$$

By using $M_s \gg H_k + H$ (soft magnetic sample and small fields) for further approximation, a simplified Kittel-formula can be found to be [Silva99]

$$f_0 \approx \frac{\mu_0 \gamma}{2\pi} \sqrt{M_\mathrm{s}\,[H_k + H]}. \tag{2.22}$$

2.4.2 Spin Waves

Up to now, the whole spin-system of a ferromagnetic body was excited with a uniform mode of precession, but the local precession of magnetization can also advance in waveforms called spin waves. In spin waves, each local spin precesses around the direction of the effective field and the neighboring spins precess with a fixed phase relationship. Spin waves are fundamental collective excitations of ferromagnetic bodies, they can be treated as quantized quasi-particles called magnons. Similar to phonons, decoherent magnons are thermally excited at room temperature. In Fig. 2.9 three basic magnetostatic modes are displayed: the magnetostatic surface spin waves in the Damon-Eshbach-configuration, where the wave vector is in-plane of the sample orthogonal to the local effective field ($\mathbf{k} \perp \mathbf{H}^{\mathrm{eff}}$), backward volume magnetostatic spin waves, where the wave vector and the effective field are in-plane and parallel $\mathbf{k} \parallel \mathbf{H}^{\mathrm{eff}}$, and forward volume magnetostatic spin waves in the configuration, where the wave vector is in-plane and the effective field is oriented out-of-plane ($\mathbf{k} \perp \mathbf{H}^{\mathrm{eff}}$). Also, there are exchange spin wave modes arising for high wave vectors. In this work we will deal only with spin waves in the Damon-Eshbach configuration. The dispersion of the magnetostatic surface spin waves can be written as [Stancil09]

$$\omega^2 = \omega_0(\omega_0 + \omega_\mathrm{M}) + \frac{\omega_\mathrm{M}^2}{4}\left[1 - \exp(-2kd)\right]. \tag{2.23}$$

Here $\omega_0 = 2\pi f_0$ is the angular resonance frequency of the material, d is the thickness of the film, k is the wave vector of the spin wave and $\omega_\mathrm{M} = 2\pi\gamma\mu_0 M_s$. The derivation of this dispersion relation and the dispersion relations of the magnetostatic volume modes including their derivation can be found for example in [Stancil09]. The forward volume

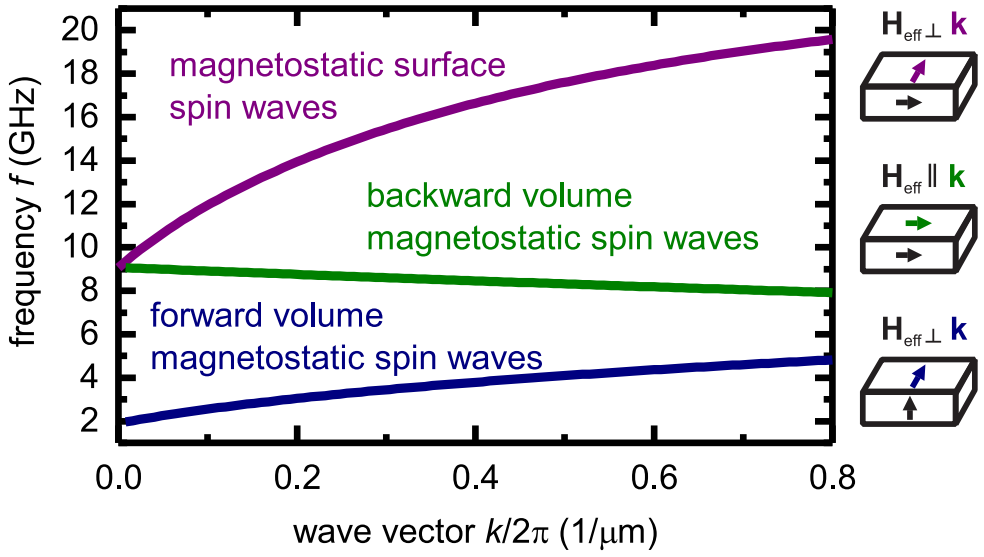

Figure 2.9: Calculated dispersion of magnetostatic spin wave modes: Magnetostatic surface spin waves occur in the so called Damon-Eshbach-configuration, where the wave vector is in-plane of the sample orthogonal to the local effective field ($\mathbf{k} \perp \mathbf{H}^{\mathrm{eff}}$). Backward volume magnetostatic spin waves, however, can be found in the configuration, where the wave vector and the effective field are in-plane and parallel ($\mathbf{k} \parallel \mathbf{H}^{\mathrm{eff}}$). Forward volume magnetostatic spin waves are found in the configuration, where the wave vector is in-plane and the effective field is oriented out-of-plane ($\mathbf{k} \perp \mathbf{H}^{\mathrm{eff}}$). The dispersion relations were calculated according to Eq. 2.23-2.25 using a resonance frequency of $f_0 = 1.9$ GHz, a saturation magnetization of $M_{\mathrm{s}} = 1200\,\mathrm{kA/m}$ and a thickness of $t = 120$ nm.

magnetostatic spin waves can be described by [Stancil09]

$$\omega^2 = \omega_0 \left[\omega_0 + \omega_{\mathrm{M}} \left(1 - \frac{1 - \exp(-kd)}{kd} \right) \right]. \tag{2.24}$$

The dispersion of the backward volume magnetostatic spin waves is found to be [Stancil09]

$$\omega^2 = \omega_0 \left[\omega_0 + \omega_{\mathrm{M}} \left(\frac{1 - \exp(-kd)}{kd} \right) \right]. \tag{2.25}$$

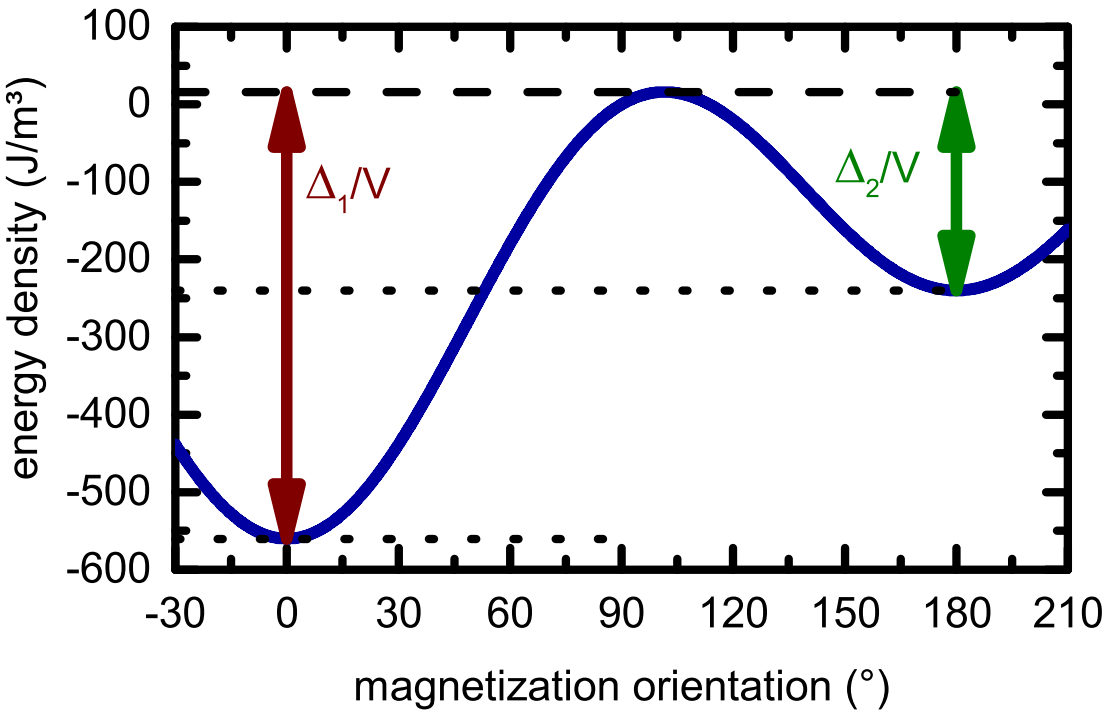

Figure 2.10: Energy barrier of a superparamagnetic (Stoner-Wolfarth) particle in an externally applied field. Δ_1 and Δ_2 denote the thermal energy needed to overcome the energy barrier to switch from $0°$ to $180°$ magnetization orientation or vice versa.

2.5 Superparamagnetism

As pointed out in Section 2.1, the magnetization orientation of ferromagnetic single domain particles relies on the relevant energy densities. However, if the particle size decreases, the total magnetic energy of the particle decreases with the volume V of the particle and a thermal activation leading to a magnetic reorientation becomes more probable. Following the approach of [Aharoni96], the energy density of a single domain particle only consisting of anisotropy and Zeeman energy is assumed

$$e_{\text{particle}} = e_{\text{anisotropy}} + e_{\text{Zeeman}} \tag{2.26}$$

$$= -K_{\text{u}} \cos^2\theta - \mu_0 M_s H \cos\theta, \tag{2.27}$$

where θ is the angle between the uniaxial easy axis and the magnetization direction. Here, the field is applied parallel to the uniaxial easy axis (both along the x-axis). Fig. 2.10 depicts this energy density for the parameter set $K_\mathrm{u} = 400\ \mathrm{J/m^3}$, $M_\mathrm{s} = 800\ \mathrm{kA/m}$ and $H = 160\ \mathrm{A/m}$. By applying an external magnetic field, the two energetic minima become different in energy, as well as the energetic barriers to jump from $\theta = 0°$ to $\theta = 180°$, Δ_1 and vice versa, Δ_2. Therefore, in a statistical ensemble of multiple single domain particles, the number of particles per unit time ν_{12} jumping from the minimum energy at $\theta = 0°$ to the minimum at $\theta = 180°$ can be written as

$$\nu_{12} = c_{12} \exp \frac{\Delta_1}{k_\mathrm{B} T}. \tag{2.28}$$

c_{12} is a constant rate. In the opposite direction, the number of particles jumping from $\theta = 180°$ to $\theta = 0°$ is

$$\nu_{21} = c_{21} \exp \frac{\Delta_2}{k_\mathrm{B} T}, \tag{2.29}$$

where c_{21} is a constant rate. c_{21} and c_{12} are constants if the energetic minima have a width of zero. For realistic cases the magnetization has a finite probability of orienting in the vicinity of the minimum and c_{21} as well as c_{12} are a function of external field and temperature. If the external magnetic field is zero, the energy barriers are equal $\Delta_1 = \Delta_2$. It is more convenient then, to consider the relaxation time τ, the average time, the system needs to jump from minimum to minimum.

$$\frac{1}{\tau} = \mathcal{F}_0 \exp\left(-\frac{K_\mathrm{u} V}{k_\mathrm{B} T}\right) \tag{2.30}$$

$\mathcal{F}_0 \approx 1\ \mathrm{GHz}$ is a material dependent parameter with dimensions of frequency [Aharoni96]. The thermal activation, then leads to a dependency on the measurement time t_meas. If $\tau \gg t_\mathrm{meas}$, there is no observed change in magnetization with time and the particle is in the range of stable ferromagnetism. If on the contrary the particles are small enough that $\tau \ll t_\mathrm{meas}$, there are many jumps from minimum to minimum and back. Without an external magnetic field, a measurement of magnetization will then yield zero. In a non-zero field the $\mathbf{M}(\mathbf{H})$ of the superparamagnetic ensemble will then take approximately the form of a Langevin-function with very high susceptibility compared to paramagnetism [Aharoni96, Bean59] and is therefore called *superparamagnetism*.

3 Modeling Superparamagnetic Microbeads on Ferromagnetic Parent Structures

Functionalized superparamagnetic microbeads (MBs) on ferromagnetic surfaces provide a platform for targeted motion of chemical and biological species in a microfluidic environment [Gijs04, Pankhurst03]. By patterning soft magnetic thin films, local effective fields are induced leading to a spatially inhomogeneous magnetic stray field distribution and energetic minima for the static equilibrium MB position. By applying time-dependent external magnetic fields the minima can be shifted in position, the motion of the MB is then determined by the interplay between the potential energy gradient varying over time and the fluid damping. Magnetic micro-disks under application of rotational magnetic fields were chosen as a model system. Previous studies discussed the looping motion [Hu15] and the maximum frequency for pure rotational motion [Beld15]. Semi-analytical models on the motion of superparamagnetic microbeads utilizing magnetic dipole models exist [Lim14, Hu15]. Here, the connection between the micromagnetic state and the magnetic stray field of the ferromagnetic parent structure and the potential energy landscape is drawn enabling the calculation of potential energy gradients for arbitrary magnetic parent structures. The equation of motion is then solved numerically. The simulation reproduces experimental results up to an excellent level of agreement. It is of deep interest to gain an understanding of the potential energy landscape for prototyping of future lab-on-a-chip devices. The results of this numerical investigation are published in [Sajjad17]. The experimental data shown in this chapter was acquired by Umer Sajjad. The simulation results were elaborated in close collaboration with Umer Sajjad and Finn Klingbeil.

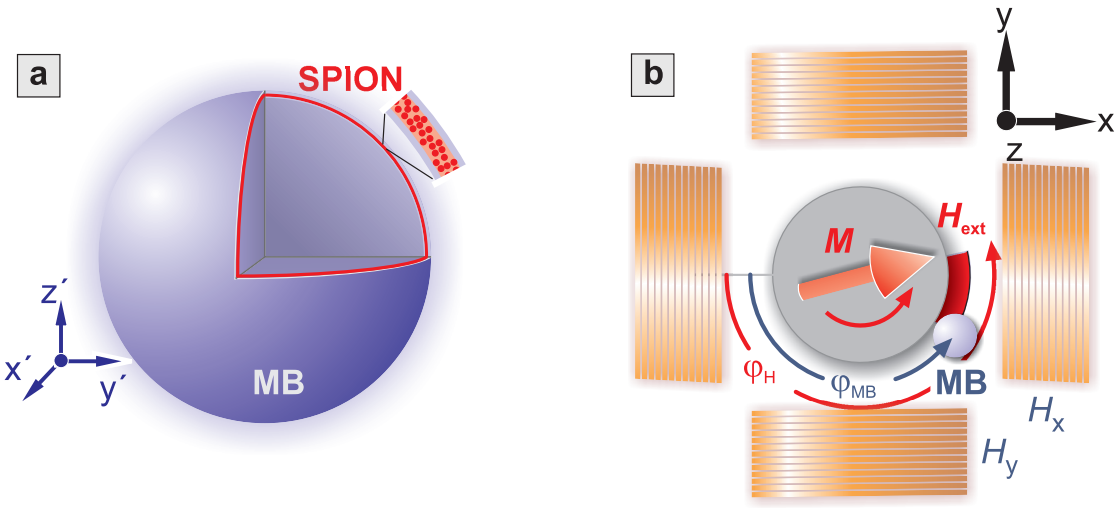

Figure 3.1: Schematic view of a) superparamagnetic iron oxide nanoparticles (SPIONs) embedded into the surface of a spherical polystyrene matrix. b) the experimental model system consisting of a microbead (MB) moving around a circular ferromagnetic disk controlled by an in-plane rotational external magnetic field at constant frequency. This figure was adapted from [Sajjad17].

3.1 Micromagnetic Configuration, Stray-Field and Potential-Energy of the System

Fig. 3.1 shows a schematic representation of the system of interest: The microbeads (MBs), schematically represented in Fig. 3.1a, consist of monodispersed magnetite nanoparticles embedded into the surface of a spherical polystyrene matrix and encapsulated by an outer polymer coating. The internal coordinate system of the MB denotes $\mathbf{x}' = (x', y', z')$, so that $\mathbf{x}'$ points towards every single superparamagnetic iron oxide nanoparticle (SPION) in the shell of the MB itself. The MB with a diameter of $8\ \mu\mathrm{m}$ is moved on a micromagnetic disk with a diameter of $30\ \mu\mathrm{m}$ and thickness of $30\ \mathrm{nm}$ controlled by a rotational external magnetic field as depicted schematically in Fig. 3.1b. The coordinate system in the reference frame of the disk is introduced as $\mathbf{x} = (x, y, z)$. φ_H is the orientation of the external magnetic field and φ_{MB} the angle of the MB, both defined with reference to the negative x-axis.

To calculate the motional response of the magnetic MBs on a ferromagnetic structure, an expression of the magnetic potential energy is needed. Furthermore, we are only interested in the local energy contributions, which change with the position of the MBs relative to the parent structure or change the energy state. Since we are interested in the motional response of MBs at external fields much higher than the anisotropy field $|\mathbf{H}_{\mathrm{ext}}| \gg H_{\mathrm{k}}$ of the parent structure material (i.e. Permalloy), and the MBs are magnetically isotropic, the anisotropy energy can be neglected. The potential energy of the system U can be written as a sum of the energy contribution of the MB E_{m} and the parent structure E_{p}

$$\begin{aligned} U(t,\mathbf{x}) &= E_{\mathrm{m}}(t,\mathbf{x}) + E_{\mathrm{p}}(t,\mathbf{x}) \\ &= -\mu_0 \int_{V_{\mathrm{m}}} dV' \mathbf{M}_{\mathrm{m}}(\mathbf{x}',t) \cdot \mathbf{H}_{\mathrm{m}}^{\mathrm{eff}}(\mathbf{x},\mathbf{x}',t) \\ &- \mu_0 \int_{V_p} dV \mathbf{M}_{\mathrm{p}}(\mathbf{x},\mathbf{t}) \cdot \mathbf{H}_{\mathrm{p}}^{\mathrm{eff}}(\mathbf{x},\mathbf{x}',t). \end{aligned} \tag{3.1}$$

t is the time, $\mathbf{M}_{\mathrm{m}}$ is the magnetization of the MB, $\mathbf{M}_{\mathrm{p}}$ the magnetization of the ferromagnetic parent structure (disk), $\mathbf{H}_{\mathrm{m}}^{\mathrm{eff}}$ the local effective field acting on the MB, $\mathbf{H}_{\mathrm{p}}^{\mathrm{eff}}$ the local effective field acting on the parent structure, V_{m} is the volume of the MB, V_{p} the volume of the parent structure. The local effective fields on MB and parent structure can then be specified by

$$\mathbf{H}_{\mathrm{m}}^{\mathrm{eff}} = \mathbf{H}_{\mathrm{ext}}(t) + \mathbf{H}_{\mathrm{p}}^{\mathrm{S}}(\mathbf{x}+\mathbf{x}',t) \text{ and} \tag{3.2}$$

$$\mathbf{H}_{\mathrm{p}}^{\mathrm{eff}} = \mathbf{H}_{\mathrm{ext}}(t) + \mathbf{H}_{\mathrm{m}}^{\mathrm{S}}(\mathbf{x}+\mathbf{x}',t). \tag{3.3}$$

$\mathbf{H}_{\mathrm{p}}^{\mathrm{S}}(\mathbf{x}+\mathbf{x}',t)$ is the outer stray field of the parent structure in the MB and $\mathbf{H}_{\mathrm{m}}^{\mathrm{S}}(\mathbf{x}+\mathbf{x}',t)$ the outer stray field of the MB in the parent structure. The internal demagnetizing fields generated by the disk are neglected due to the rotational symmetry. Also the internal demagnetizing field of the MB is not considered for reasons of simplicity and because the integral measurement of the susceptibility-field dependence, which is used later on, is not corrected by the demagnetizing field as well. Applying a rotational external magnetic field leads to a time dependent magnetization variation in the MB and the parent structure resulting in a time dependence of the corresponding magnetic stray fields. By substituting

and using the micromagnetic reciprocity theorem [Aharoni96], which states

$$\int_{V_1} dV \mathbf{H}_2 \cdot \mathbf{M}_1 = \int_{V_2} dV \mathbf{H}_1 \cdot \mathbf{M}_2, \tag{3.4}$$

Eq. 3.1 can be rewritten to

$$\begin{aligned} U(t,\mathbf{x}) &= -\mu_0 \int_{V_\mathrm{m}} dV' \mathbf{M}_\mathrm{m}(\mathbf{x}',t) \cdot (\mathbf{H}_\mathrm{ext}(t) + 2\mathbf{H}_\mathrm{p}^\mathrm{S}(\mathbf{x}+\mathbf{x}',t)) \\ &- \mu_0 \int_{V_p} dV \mathbf{M}_\mathrm{p}(\mathbf{x}',t) \cdot \mathbf{H}_\mathrm{ext}(t) \\ &= -\mu_0 \int_{V_\mathrm{m}} dV' \mathbf{M}_\mathrm{m}(\mathbf{x}') \cdot (\mathbf{H}_\mathrm{ext}(t) + 2\mathbf{H}_\mathrm{p}^\mathrm{S}(\mathbf{x}+\mathbf{x}',t)) + C_1, \end{aligned} \tag{3.5}$$

where C_1 is a constant contribution, arising since the magnetization is in its equilibrium for slow fields and $|\mathbf{H}_\mathrm{ext}| = \mathrm{constant}$ for simply rotational fields, so that the integration $\mathbf{M}_\mathrm{p}(\mathbf{x}',t) \cdot \mathbf{H}_\mathrm{ext}(t)$ yields the same value for each field orientation. Now, the magnetization of the superparamagnetic MB can be rewritten in terms of the susceptibility χ

$$\mathbf{M}_\mathrm{m} = \chi(\mathbf{x}')(\mathbf{H}_\mathrm{ext}(t) + \mathbf{H}_\mathrm{p}^\mathrm{S}(\mathbf{x}+\mathbf{x}',t)) \tag{3.6}$$

leading to

$$\begin{aligned} U(t,\mathbf{x}) &= -\mu_0 \int_{V_\mathrm{m}} dV' \chi(\mathbf{x}')(\mathbf{H}_\mathrm{ext}(t) + \mathbf{H}_\mathrm{p}^\mathrm{S}(\mathbf{x}+\mathbf{x}',t)) \cdot (\mathbf{H}_\mathrm{ext}(t) + 2\mathbf{H}_\mathrm{p}^\mathrm{S}(\mathbf{x}+\mathbf{x}',t)) \\ &+ C_1 \\ &= -\mu_0 \int_{V_\mathrm{m}} dV' \chi(\mathbf{x}')(2(\mathbf{H}_\mathrm{p}^\mathrm{S}(\mathbf{x}+\mathbf{x}',t))^2 + 3\mathbf{H}_\mathrm{p}^\mathrm{S}(\mathbf{x}+\mathbf{x}',t) \cdot \mathbf{H}_\mathrm{ext}(t)) \\ &+ C_1 + C_2. \end{aligned} \tag{3.7}$$

Here, C_2 is another constant contribution representing the time-dependence of the absolute value of the external magnetic field $|\mathbf{H}_\mathrm{ext}| = \mathrm{constant}$. In order to account for the distribution of SPIONs in the shell of the magnetic MB, an approach for the susceptibility is made to be

$$\chi(\mathbf{x}') = \chi(r') = \chi^\mathrm{eff} \Theta(r' - r_\mathrm{i}) \Theta(r_\mathrm{m} - r'). \tag{3.8}$$

In this expression $r' = |\mathbf{x}'|$ is the radial distance in the center of mass coordinate system of the MB, r_i is the inner radial distance determining the width of the magnetic shell,

r_m is the radius of the MB, $\Theta(x)$ is the Heaviside step function and χ^eff is the effective susceptibility of the magnetic shell. Substituting this into Eq. 3.7 and evaluating the Heaviside-functions then yields

$$\begin{aligned} U(t,\mathbf{x}) &= -\mu_0\chi^\mathrm{eff}\int_{V_\mathrm{s}} dV'(2(\mathbf{H}_\mathrm{p}^\mathrm{S}(\mathbf{x}+\mathbf{x}',t))^2+3\mathbf{H}_\mathrm{p}^\mathrm{S}(t,\mathbf{x}+\mathbf{x}')\cdot\mathbf{H}_\mathrm{ext}(t)) \\ &+ C, \end{aligned} \tag{3.9}$$

where $C = C_1 + C_2$ is a constant and V_s is the Volume of the shell containing SPIONs. χ^eff is safely assumed to be constant for one external magnetic field strength $|\mathbf{H}_\mathrm{ext}|$, because the numerical simulations show, that the mean magnetic field acting on the MB is dominated by the external magnetic field. Eq. 3.9 can now be evaluated numerically, by calculating the magnetic stray field distribution of the ferromagnetic disk using a micromagnetic software. Here, a magnetization configuration of a Permalloy ($\mathrm{Ni_{81}Fe_{19}}$) disk at an external field strength of $|\mathbf{H}_\mathrm{ext}| = 16\,\mathrm{kA/m}$ calculated by mumax^3 [Vansteenkiste14], already presented in Fig. 2.1 and discussed in Section 2.1.4 was used. To calculate long-range magnetostatic stray-fields, the magnetization was averaged in-plane over 5 neighboring cells, reducing the grid to $340 \times 340 \times 3$. Then the grid was extended by in-plane zero-padding into the area of zero magnetization to an input magnetization grid size of $1024 \times 1024 \times 3$ with a cell size of $90 \times 90 \times 10\ \mathrm{nm}^3$. By using Micromagus ® [Berkov93] the stray-field distribution on top of the disk was calculated on a total volume of $92160 \times 92160 \times 8100\ \mathrm{nm}^3$ using $90 \times 90 \times 100\ \mathrm{nm}^3$ big cells. The resulting energy landscape for a microbead of diameter $8\ \mu\mathrm{m}$ directly on top the ferromagnetic disk is depicted in Fig. 3.2. The integration of the micromagnetic stray field was carried out numerically using the trapezoidal rule. Two energy minima at the north and south pole of the ferromagnetic onion state (compare Fig. 2.1 with Fig. 3.2) are visible. Because the uniaxial anisotropy contribution was neglected for the soft magnetic disk, the time dependence of the potential energy landscape is simply given by a sinusoidal coherent rotation of the energy landscape shown in Fig. 3.2. In the following, the rotation of the potential energy is achieved by rotating the coordinate system and interpolating in the new system.

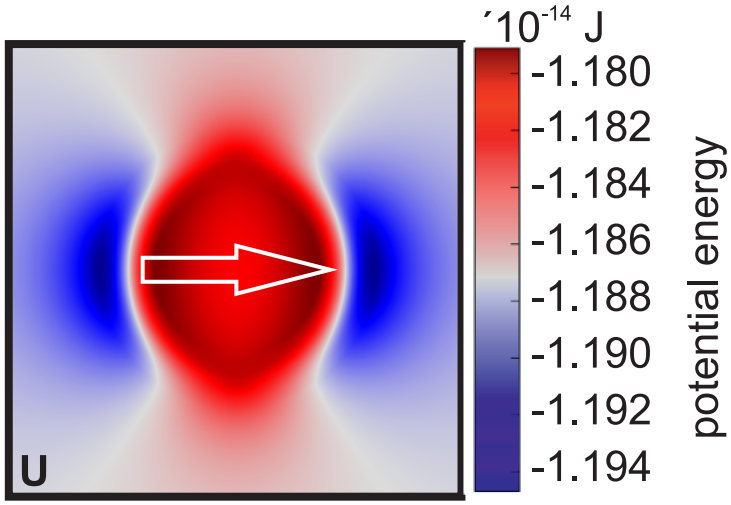

Figure 3.2: In-plane potential energy landscape obtained by integration of the magnetic stray field distribution (compare Eq. 3.9). This figure was adapted from [Sajjad17].

3.2 Equation of Motion in Fluid Medium

Knowing the magnetic potential energy of the system, the next step is the evaluation of the equation of motion in the hydrodynamic system. Non-hydrodynamic forces are the magnetostatic force, the gravitational force and the frictional force generated, when the MB touches the surface of the parent structure. Since no rolling on the surface is observed, the frictional force is neglected [Hu15]. Furthermore, the magnetostatic force along the z-axis is small and we assume that the gravitational force will constrain the MB into a two dimensional motion on the surface of the parent structure, so that the external force $\mathbf{Z}$ is specified as

$$\mathbf{Z}(t, \mathbf{x}) \approx -\nabla U(t, \mathbf{x}|_{z=r_\mathrm{m}}). \tag{3.10}$$

Experimentally it was found, that the MBs move in the regime of low Reynolds numbers

$$\mathrm{Re} = \rho_\mathrm{f} \cdot \mathrm{v_m} \cdot 2r_\mathrm{m}/\eta = 9 \cdot 10^{-4}. \tag{3.11}$$

$\rho_\mathrm{f} \approx 1000\ \mathrm{kg\,m^{-3}}$ is the fluid density of H_2O, $\mathrm{v_m} \approx 100\ \mu\mathrm{m\,s^{-1}}$ is the maximum rotational velocity reached in experiment, $2r_\mathrm{m} = 8\ \mu\mathrm{m}$ is the diameter of experimentally

used MBs and $\eta \approx 0.9\ \mathrm{mPa\,s}$ is the dynamic viscosity of H_2O at a temperature $T = 25\ ^\circ\mathrm{C}$ [Korosi68]. In this regime the flow is described by the Basset-Boussinesq-Oseen equation [Oseen27] including the assumption of vanishing fluid velocity

$$\rho_\mathrm{m}\frac{4\pi}{3}r_\mathrm{m}^3\cdot\frac{\mathrm{d}^2\mathbf{x}}{\mathrm{d}t^2} = -6\pi\eta r_\mathrm{m}\frac{\mathrm{d}\mathbf{x}}{\mathrm{d}t} - \frac{4\pi}{3}r_\mathrm{m}^3\nabla p - \rho_\mathrm{f}\frac{2\pi}{3}r_\mathrm{m}^3\frac{\mathrm{d}^2\mathbf{x}}{\mathrm{d}t^2} \\ -6r_\mathrm{m}\sqrt{\pi\rho_\mathrm{f}\eta}\int_{t_0}^{t}\mathrm{d}\tau\frac{1}{\sqrt{t-\tau}}\frac{\mathrm{d}}{\mathrm{d}\tau}\frac{\mathrm{d}\mathbf{x}}{\mathrm{d}t} + \mathbf{Z}. \tag{3.12}$$

p is the pressure in the fluid, $\rho_\mathrm{m} = 1030\ \mathrm{kg\ m^{-3}}$ is the overall mass density of the MB, t_0 the initial time and τ the integration time. The influence of the Basset-Force corresponding to the integral term in the Basset-Boussinesq-Oseen equation was estimated by numerical simulations to be in mean $0.5\ \mathrm{pN}$, which is about one order of magnitude smaller than the other relevant forces. Neglecting the Basset-Force corresponding to rather steady forces and assuming no pressure gradient leads to a more simplified equation of motion

$$m_\mathrm{eff}\cdot\frac{\mathrm{d}^2\mathbf{x}}{\mathrm{d}t^2} = -\Gamma_\mathrm{hd}\frac{\mathrm{d}\mathbf{x}}{\mathrm{d}t} + \mathbf{Z}. \tag{3.13}$$

$m_\mathrm{eff} = (4\pi/3)r_\mathrm{m}^3(\rho_\mathrm{m} + \rho_\mathrm{f}/2)$ is the effective mass and $\Gamma_\mathrm{hd} = 6\pi\eta r_\mathrm{m}$ is the linear hydrodynamic damping. Changing the temperature in the relevant range of $T = 20 - 30\ ^\circ\mathrm{C}$ already leads to a shift of approximately 20% in the hydrodynamic damping parameter due to the temperature dependence of the viscosity of water [Korosi68]. The first term on the right side of Eq. 3.13 will be called «drag force» in the following.

3.3 Micromechanical Numerical Algorithm

Interpolation of the global time-dependent potential energy landscape is computationally exhaustive and in order to solve the equation of motion numerically using a solver for ordinary differential equations (ODE), the interpolation would be called by the solver many times. Therefore, the time-dependence of the potential energy landscape was fitted using a standard discrete Fourier series algorithm up to an order of $N = 30$ in every pixel. After that, the spatial dependence of the obtained Fourier-coefficients was fitted using

polynomials up to an order of $P = 2$ in the local $2.79 \times 2.79\ \mu\mathrm{m}^2$-big circumference of the MB center of mass. Now, the potential energy can be written locally in matrix form

$$U(t, \mathbf{x}) = \mathbf{F}_1^T(t)\mathcal{A}\mathbf{p}(\mathbf{x}) + \mathbf{F}_2^T(t)\mathcal{B}\mathbf{p}(\mathbf{x}), \tag{3.14}$$

where $\mathbf{F}_1^T(t) = (1, \cos\omega t, ..., \cos N\omega t)$ and $\mathbf{F}_2^T(t) = (0, \sin\omega t, ..., \sin N\omega t)$ are vectors containing the time-dependence, the polynomials carry the spatial dependence $\mathbf{p}^T(\mathbf{x}) = (1, x, y, xy, x^2, y^2)$ and the matrices $\mathcal{A}$ and $\mathcal{B}$ contain the numerically obtained coefficients. Increasing the order of the polynomial or Fourier series coefficients beyond $P = 2$ and $N = 30$ did not have any noticeable effect on our numerical results. Using MATLAB's ODE-solver 'ode15s' [Shampine97, Shampine99], the equation of motion (Eq. 3.13) can now be solved. In order to maintain numerical accuracy, the equation of motion was solved for a maximum time of $\Delta t = 0.7$ ms, divided by 200 time steps in the local environment of the MB's center of mass. The solving time t_i is then chosen among the time-steps in a way that the metric between the local numerical solution $\mathbf{x}_i$ and the grid points $\mathcal{X}$ is minimized

$$t_i = t(\min(|\mathbf{x}_i - \mathcal{X}|)). \tag{3.15}$$

Also, the ratio between the grid discretization Δx and maximum MB velocity is kept larger than the maximum timestep

$$\Delta t \ll \Delta x / \mathrm{v_m}. \tag{3.16}$$

After solving the trajectory for a time t_i, the next local coefficients $\mathcal{A}$ and $\mathcal{B}$ are chosen for the now closest grid point and the next local equation of motion can be solved. The only free parameter used to fit the results was the effective susceptibility χ_{eff} deviating only by a factor of 2 ± 0.25 from the susceptibility curve obtained by the $\mathbf{M}(\mathbf{H})$ measurement of the vendor [M15].

3.4 Occurrence of Looping Motion

3.4.1 Two Dimensional Trajectory Analysis

The foundation for a numerical model of microbead motion has been laid. Now, a comparison of experimental and simulated data is desired, in order to learn more about the physics of MB motion. Fig. 3.3 shows the simulated and experimental MB trajectories at selected external field rotation frequencies at an absolute field value of $|\mathbf{H}_{\mathrm{ext}}| = 16\ \mathrm{kA/m}$. In Fig. 3.3a,d the trajectory at a rotational field frequency of $f = 0.6\ \mathrm{Hz}$ is shown. Here, the motion of the MB takes a circular path around the ferromagnetic disk. At $f = 0.7\ \mathrm{Hz}$, depicted in Fig. 3.3b,e, the trajectory qualitatively changes: First, the motion follows again a circular orbit, but then one looping occurs, where the MB is pulled away showing an increase followed by a decrease of radial distance to the center of the disk. After the looping, the MB continues its circular motion around the disk. Fig. 3.3c,f shows the trajectory at $f = 0.9\ \mathrm{Hz}$. A qualitatively similar behavior compared to $f = 0.7\ \mathrm{Hz}$ can be seen: Circular motion, interrupted by looping motion. However, the number of loopings at $f = 0.9\ \mathrm{Hz}$ increased from one to four compared to $f = 0.7\ \mathrm{Hz}$. In general, the simulated data is congruent with the experiment.

The data shown here suggests that there are at least two regimes of motion for the superparamagnetic MBs [Lim14]. In the first regime, the MB is simply moving with the external field and the magnetization, which can be seen at $f = 0.6\ \mathrm{Hz}$. By increasing the frequency a second regime of motion will be entered: In this regime looping motion interrupts the pure circular motion. It is evident that there will be more loopings per revolution with increasing the frequency of the rotational magnetic field, as can be seen from $f = 0.7\ \mathrm{Hz}$ and $f = 0.9\ \mathrm{Hz}$. In general the looping phenomenon is of great interest, since it promises a controllable process of moving microbeads from one parent structure to another. Therefore an in depth analysis of the looping phenomenon is required.

3.4.2 Polar Coordinate Parametrization and Force Analysis

Another parametric representation of this data is exhibited in Fig. 3.4. The radial distance from the center of the disk to the MB center of mass, the phase shift Δ describing

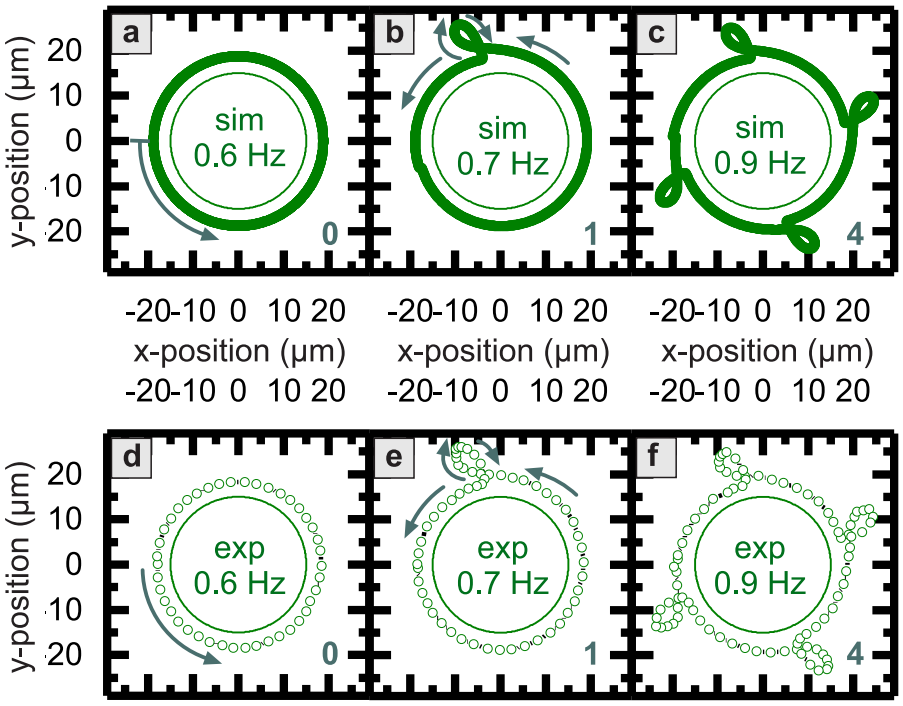

Figure 3.3: Simulated and experimental trajectories of one individual diameter $8\ \mu$m-MB. a-c) show the simulated MB-trajectory at $|\mathbf{H}_{\text{ext}}| = 16\ \text{kA/m}$ for one full rotation around the ferromagnetic disk, d-f) show the corresponding experimental data. a,d) exhibit the MB-trajectory at an external field frequency $f = 0.6$ Hz, b,e) show the MB-trajectory at $f = 0.7$ Hz and c,f) display the MB-trajectory at $f = 0.9$ Hz. The inner circle represents the edges of the magnetic disk. This figure was adapted from [Sajjad17].

the relative rotational phase between the moving energetic minimum and the MB, the field angle, the azimuthal and the radial magnetic force acting on the MB are shown as a function of the bead angle. At 0.6 Hz the radial position remains constant and the phase shift shows only small deviations possibly due to a small ellipticity of the effective field caused by the neglected anisotropy field. Also, the field angle is increasing linearly, the azimuthal force shows small oscillations around a constant level (exhibiting a different periodicity than the phase shift) and the radial magnetic force remains at zero. At $f = 0.7$ Hz the microbead motion shows five typical features for the looping motion: First, a steep increase of radial distance and a fast pullback to the equilibrium orbit around the disk. Second, the phase shift is not oscillating around a constant level anymore, but at the same bead angle as the looping occurs, the phase shift drastically increases. Third, the slope of the field angle plotted against the bead angle changes the sign twice at the looping event, because the bead is shortly moving in the opposite sense of rotation compared to the rotational field and turning around again after. Fourth, at the looping event, the azimuthal magnetic force drastically decreases from a constant level with small oscillations, also undergoes two sign changes, before its increasing again as quick as it decreased. And fifth, the radial magnetic force stays constant at first, briefly before it starts to rise into positive values, pushing the bead outwards, until it decreasing a lot to even lower negative values on a fixed MB-position and increases on the same position to zero again. At $f = 0.9$ Hz the loopings look qualitatively the same as at $f = 0.7$ Hz, but there is an increase of loopings per bead revolution. The congruence of experimental and simulated data suggests, that the simulated forces can be employed to gain a better understanding of the system.

In the case of simple circular motion, it is clear, that the MB is moving with the magnetic potential well (compare Fig. 3.2), but the non-zero phase shift suggests, that the MB is traveling behind the minimum, due to the additional drag force acting in the opposite direction of the MB velocity (see Eq. 3.13). This means, that the MB remains in a dynamical equilibrium position on the edge of the moving potential well. At higher frequencies, the phase-shift does not remain on a stable level, but there exists a point in the phase-shift when the MB becomes decoupled from the potential well. Then the radial magnetic force pushes the MB to the outside of the orbit, and the azimuthal force pushes the MB a bit backwards leading to the looping motion. Meanwhile, the potential energy landscape has rotated far enough, that the MB can be recaptured by a potential minimum

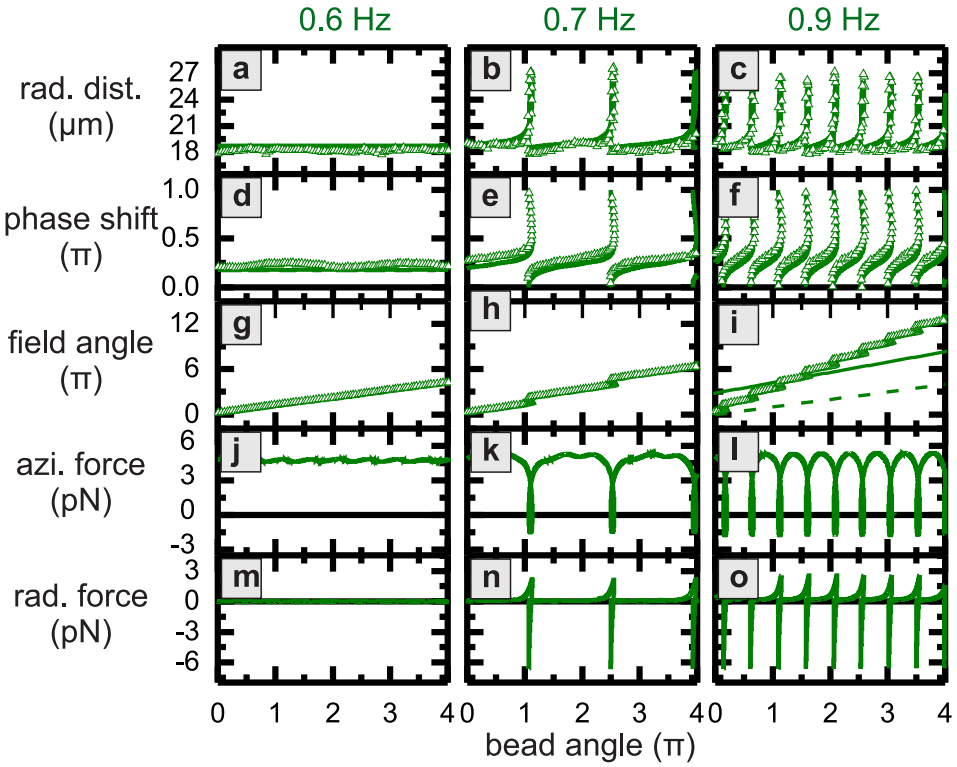

Figure 3.4: Motional response of a MB on a disk parent structure in a rotational magnetic field of amplitude $|\mathbf{H}_{\text{ext}}| = 16\ \text{kA/m}$ at selected frequencies. a-c) Radial center to center distance from disk to MB. d-f) phase shift Δ describing the relative phase between moving energetic minimum and the MB. g-i) angle of the external magnetic field. j-l) Simulated azimuthal magnetic force. m-o) Simulated radial magnetic force. The columns correspond to $f = 0.6$ Hz, to $f = 0.7$ Hz and to $f = 0.9$ Hz. This figure was adapted from [Sajjad17].

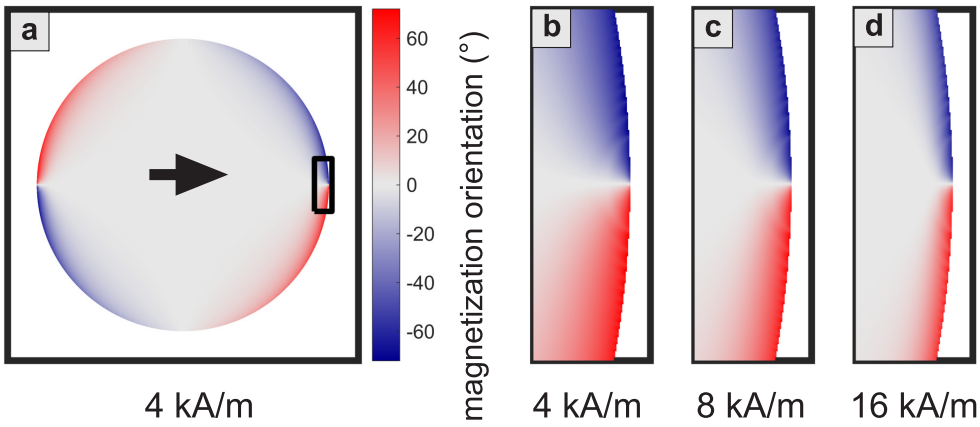

Figure 3.5: Magnetization state of a $30\ \mathrm{nm}$ thin magnetic Permalloy disk with a diameter of $30\ \mu\mathrm{m}$. a) At an external field of $4\ \mathrm{kA/m}$ in an azimuthal angle representation of the magnetization configuration. b) Magnification of a) in the region of the magnetic north pole. c) the same region at an external field of $8\ \mathrm{kA/m}$. d) the same region at an external field of $16\ \mathrm{kA/m}$. This figure was adapted from [Sajjad17].

into the orbit of circular motion. This corresponds to the strong pullback to the stable level in radial and azimuthal magnetic force. After this, the phase shift slowly increases, until there is another looping event.

3.4.3 Tuning of the Micromagnetic State via External Field

The motional response of the MB is tunable not only via the frequency, but also via the magnitude of the external magnetic field. Fig. 3.5 depicts the change of the magnetization state of a $30\ \mathrm{nm}$ thin magnetic Permalloy disk with a diameter of $30\ \mu\mathrm{m}$. In Fig. 3.5a the in-plane magnetization angle is shown for the full disk at an external field magnitude of $4\ \mathrm{kA/m}$. An area of particular interest around the magnetic north pole is marked with a black rectangle and magnified in Fig. 3.5b. The same area is depicted for external field magnitudes of $8\ \mathrm{kA/m}$ and $16\ \mathrm{kA/m}$ in Fig. 3.5c and d. As can be seen from these magnifications, the area of the magnetic onion state gets more narrow with increasing external magnetic field. This results also in a more deep minimum of the potential energy

landscape and consequently affects the motion of the MB around the disk structure.

3.4.4 Velocity Analysis

At last, the velocity and number of loopings per revolution is being exhibited in Fig. 3.6 as a function of external field frequency for three different absolute field values $|\mathbf{H}_{\mathrm{ext}}| = 4, 8, 16\ \mathrm{kA/m}$. It can be seen from Fig. 3.6a, that for each absolute external field value $|\mathbf{H}_{\mathrm{ext}}|$ there is a distinct critical frequency, at which the first looping event occurs. This critical frequency increases with increasing external field strength. This can be understood by a deeper potential well with increasing external field strength, due to higher demagnetizing fields. At higher frequencies than the critical frequency, the number of loopings increases rapidly almost linearly, where the slope decreases with increasing $|\mathbf{H}_{\mathrm{ext}}|$. The slope changes for different external fields, because the magnetic onion state gets more narrow with increasing field, as depicted in Fig. 3.5, and consequently the potential energy well gets deeper. This also leads to higher critical frequencies: a deeper potential well requires a larger damping force (which is proportional to the velocity) to overcome the energy barrier needed to transit into the looping motion regime. In Fig. 3.6b the MB frequency f_{MB} and angular velocity v_{MB} are plotted against the external field frequency. The MB frequency f_{MB} was defined here, as $1/\mathfrak{T}$, where $\mathfrak{T}$ is the time required for one revolution around the disk. The angular velocity is calculated as the equilibrium disk center to microbead distance d_{MB} times the MB frequency $v_{\mathrm{MB}} = d_{\mathrm{MB}} \cdot f_{\mathrm{MB}}$. As can be seen from Fig. 3.6b, the MB frequency increases linearly with a slope of one with the frequency of the external field. At each absolute field value there is a distinct frequency at which the MB frequency drops below the external field frequency. This frequency coincides with the critical frequency from Fig.3.6a, at which the first looping event occurs. The drop in microbead frequency compared to field frequency is quite steep directly at the critical frequency, but the negative slope gradually increases towards zero with increasing field frequencies.

It is clear from Fig. 3.6 and the figures presented before, that the angular velocity has to drop, when entering the regime of looping motion: For each looping event, the MB »waits« after being decoupled from one of the energetic minima, to be attracted by the next rotating minimum and therefore loses speed. The experimental and simulated data are in very good agreement. There is only a small discrepancy at lower fields

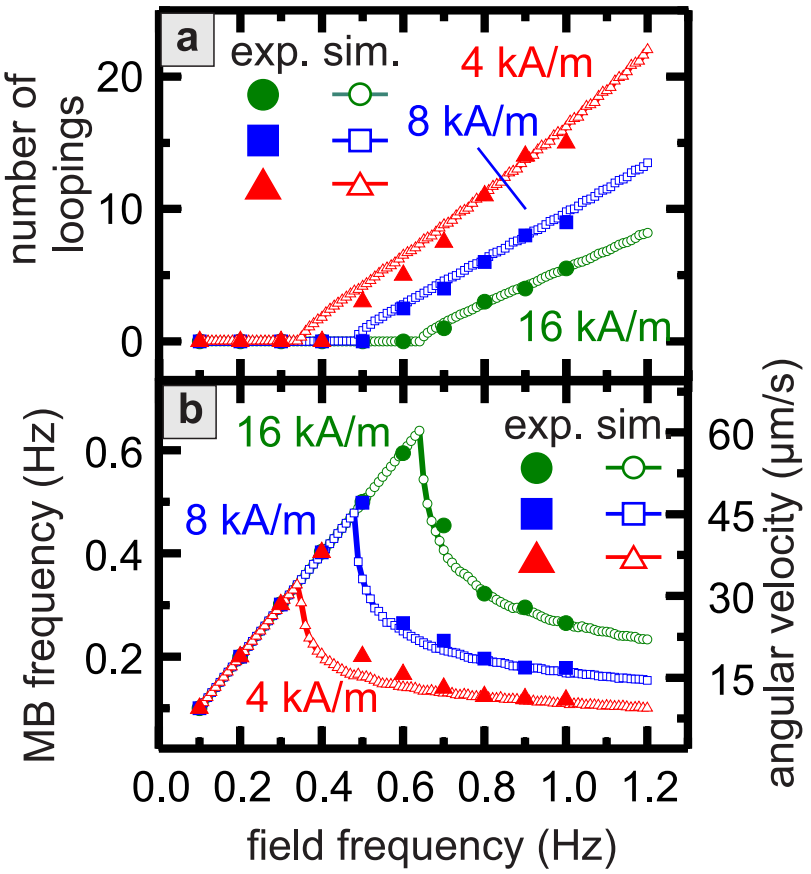

Figure 3.6: a) Number of loopings per revolution as a function of the external field frequency for the external field amplitudes $|\mathbf{H}_{\text{ext}}| = 4, 8, 16\ \text{kA/m}$ and b) responding MB frequency and angular velocity as a function of the external field frequency for the external field amplitudes $|\mathbf{H}_{\text{ext}}| = 4, 8, 16\ \text{kA/m}$. This figure was adapted from [Sajjad17].

around the critical frequency. This mismatch could be attributed to surface friction, mechanical and magnetic defects. It is expected that these effects are more pronounced at lower fields and around the critical frequency, since the energy barrier between pure rotational and looping motion is less big for these parameters. At high external fields (i.e. $|\mathbf{H}_{\mathrm{ext}}| = 16\ \mathrm{kA/m}$), the simulated data fully matches the experiment.

3.5 Summary

For the purpose of simulating the motion dynamics of superparamagnetic MBs on ferromagnetic surfaces, an algorithm was developed, which accounts for the micromagnetic state and the dynamic motion of magnetic microstructures. Here, the motion of a magnetic onion state leading to a minimum of the potential energy was calculated. Moreover, we used the micromagnetic reciprocity theorem enabling us to calculate the potential energy via the magnetic stray-field distribution of the ferromagnetic parent structure and the magnetization of the MB. For alternative purposes, it might be more suitable to use the reciprocity theorem in the other direction considering the micromagnetic magnetization configuration of the parent structure and the stray-field distribution of the MB. Therefore, tiny adjustments to the analytical calculations and the numeric algorithm will yield a general algorithm for the calculation of MB motion on arbitrary magnetic microstructures with arbitrary field signals simply by knowledge of the micromagnetic magnetization state. Also, magnetic MBs with different sizes and magnetic content could be investigated numerically. This could help design new lab on a chip devices utilizing functional superparamagnetic MBs, unlocking the possibility of two-dimensional motion, mixing and separation of differently sized magnetically labeled objects.

4 Magneto-Optical Microscopy: Imaging Magnetization at the Picosecond-Scale

There are few techniques, which are capable of measuring vectorial magnetization information with spatial resolution. Among them are differential phase contrast Lorentz transmission electron microscopy (LTEM) [Chapman83, Chapman90], scanning electron microscopy with polarization analysis (SEMPA) [Scheinfein90, Pierce11], or x-ray magnetic circular dichroism (XMCD) [Kim01]. Also, magneto-optical wide-field imaging is a powerful and efficient technique to image magnetization orientation with high spatial resolution [McCord15]. For quantitative measurements of the normalized magnetization vector, generally multiple magneto-optical images or sensitivities have to be combined in order to gain a vectorial in-plane magnetization data-set [Rave87, Rave90, Rave93]. Moreover, in-plane and out-of-plane magneto-optical contrast could be separated from each other in films with oblique plane of anisotropy [Urs16]. In [Soldatov17] the measurement of quantitative static pure in-plane magnetization is demonstrated by using two diametrically aligned sensitivities with oblique incidence. A recent review on magneto-optical imaging can be found in [McCord15].

In order gain a good time resolution in stroboscopic magneto-optical imaging, picosecond lasers are desired as an illumination source. In [Argyle00] a suitable illumination method for laser illumination in magneto-optical experiments is presented avoiding laser speckles. Based on this time-resolved experiments could be performed using pulsed magnetic fields as excitation for magnetization dynamics in Permalloy elements [Neudert05a]. This enabled research as the investigation of vortex core dynamics [Neudert05b] or the pulsed generation of Bloch-lines in cross-tie walls [Queitsch06]. Furthermore, by em-

ploying a high frequency sinusoidal magnetic field excitation more effects such as domain wall motion, local ferromagnetic resonance or spin-wave excitation could be monitored [Mozooni14, Mozooni15].

In this chapter the polar, longitudinal and transversal configuration are introduced. A brief introduction to magneto-optical microscopy based on the magneto-optical Kerr effect (MOKE) is given. Throughout my work, I have developed a timing algorithm, which allows for a fast phase detection and direct correction of large timescale drifts between field stimulus and laser pulse. This was a prerequisite for increasing the measurement time, while remaining with a stable phase. Due to the gained stability and the implementation of a two-axis motor, successful component-selective imaging with picosecond time-resolution could be performed. The separation of dynamic polar and longitudinal MOKE signals is performed by varying the plane and angle of incidence of illumination and allows for quantitative extraction of the time-dependent spatially resolved magnetization response. Combining vector and time-resolved imaging in one unique stable magneto-optical microscope paves the way for new insight on dynamic magnetization processes governed by local effective fields. The main aspects and recent achievements on the microscope have been published in [Holländer17]. The implementation of the dynamical vector method was subject to the master thesis of Mathis Lohmann. The dynamic vector measurements shown in this chapter were performed together with Cai Müller.

4.1 Magneto-Optical Microscopy

4.1.1 Magneto-Optical Kerr Effect

Throughout this work, magneto-optical microscopy based on the magneto-optical Kerr effect (MOKE), first investigated by John Kerr in 1877 [Kerr77] will be used. With the exception of the transverse MOKE configuration, the MOKE describes a rotation of the plane of linearly polarized light reflected by a reflective magnetic specimen due to the magnetization in the sample. By using two polarizers and a quarter-wave-plate, this rotation can be converted into a linear magnetization dependence of the intensity.

In Fig. 4.1 four different geometries are depicted for the MOKE. Fig. 4.1a displays the polar MOKE geometry. Here, the magnetization is oriented out-of-plane and the signal is linear in the intensity component normal to the surface. Therefore, for optimal polar contrast, the angle of incidence is $\theta = 0°$, perpendicular to the sample surface. Furthermore, there are two configurations to measure magnetic in-plane contrast using the longitudinal Kerr-effect. Fig. 4.1b shows the longitudinal parallel configuration, where the polarization of the incident light is parallel to the plane of incidence (p-polarized) and Fig. 4.1c exhibits the longitudinal perpendicular configuration, where the polarization of the incident light is perpendicular to the plane of incidence (s-polarized). For the longitudinal Kerr-effects an in-plane component of the incident light is required ($\theta \neq 0°$). Furthermore, when measuring in the longitudinal configuration, the sensitivity axis of magnetization is defined parallel to the plane of incidence. Since the out-of-plane component of the incident light can never be zero, when measuring with oblique incidence, there is always a non-zero sensitivity to out-of-plane magnetization.

In this work only thin films of soft-magnetic amorphous alloys with in-plane anisotropy are measured, where the magnetization can safely be assumed to be aligned in the film plane for static measurements. However, for the dynamic measurements performed here, the magnetization precesses out-of-plane and a strong polar contrast can be observed, also when measuring with oblique plane of incidence. Fig. 4.1d shows the transverse MOKE configuration. In this configuration the plane of incidence is perpendicular to the sensitivity axis of magnetization and the polarization is parallel to the plane of incidence. The transverse Kerr-effect does not describe a Kerr-rotation, but a change in amplitude of the polarized light. An advantage of the transverse configuration is that the signal can be measured without an analyzer and then contains pure in-plane magnetization information. However, it is not straightforward to implement this configuration in a wide-field magneto-optical microscope, since by leaving out the analyzer the overall light intensity increases and the utilized cameras cannot work accordingly within this intensity regime. When measuring with oblique incidence and p-polarized, the signal naturally contains a remaining transverse contrast (compare Fig. 4.1b,d, but it is significantly smaller. Also, there is a magneto-optical configuration, where the incident polarization is aligned $45°$ to the plane of incidence and the analyzer and the polarizer are crossed canceling out

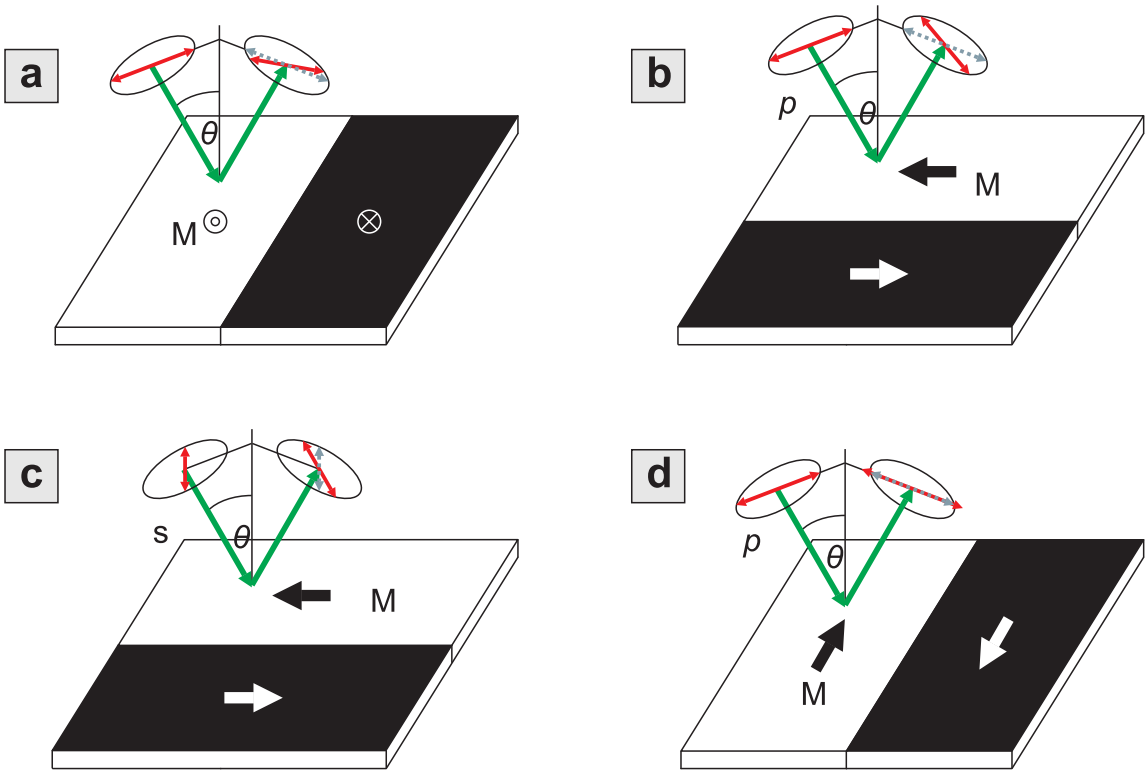

Figure 4.1: Magneto-optical configurations: Red arrows indicate plane of polarization before and after reflection, green arrows indicate incident and reflected beam of light, grey arrows indicate the plane of polarized light as it would be after reflection without Kerr-effect (reflected on a „non-magnetic “sample). a) the polar magneto-optical configuration: The polar Kerr effect occurs also for zero angle of incidence ($\theta = 0$). b) the longitudinal parallel configuration (p-polarized) c) the longitudinal perpendicular configuration (s-polarized): the longitudinal effects increase with $\sin\theta$. The longitudinal parallel effect and longitudinal perpendicular effect turn the plane of polarized light into opposite directions d) the transverse configuration: The transverse effect shows no rotation of the polarized light, it is an amplitude effect. Longitudinal and transverse effect require a non-zero angle of incidence θ. Figure created according to [Hubert08].

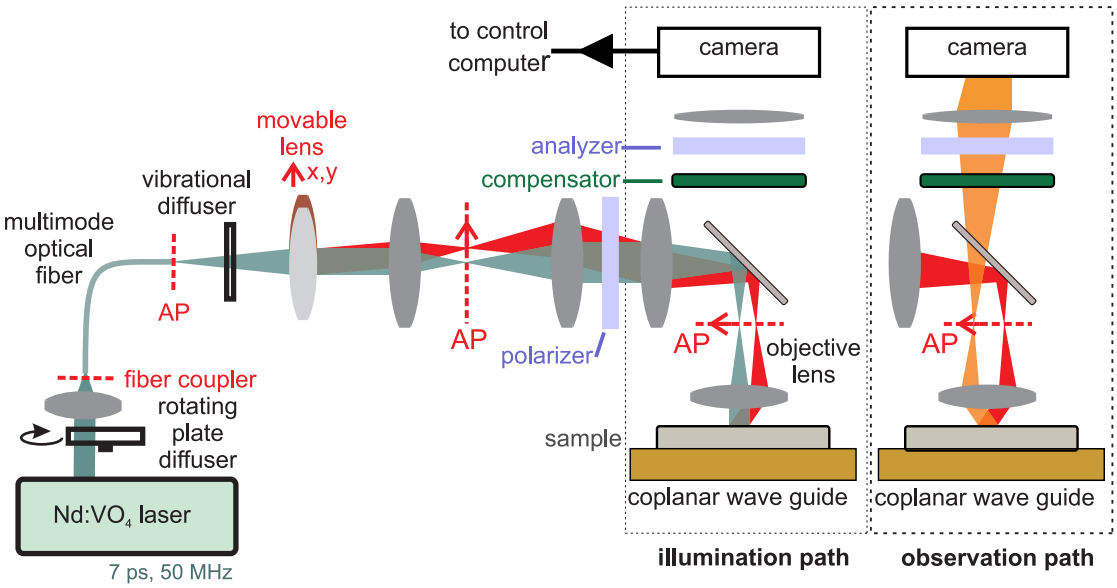

Figure 4.2: Illumination and observation path of a magneto-optical wide-field microscope using a pulsed laser illumination for stroboscopic time-resolved experiments: The movable lens enables automatic beam control for component-selective imaging. The right schematic exhibits only the observation path.

the longitudinal effects and leading to a superposition of polar and transverse contrast [Hubert08]. This configuration is not used in this work. In the following, we will mainly rely on the polar and longitudinal Kerr effect.

4.1.2 Time-Resolved Magneto-Optical Wide-Field Imaging

In order to gain a quantitative understanding of fast magneto-dynamic process, time-resolved magneto-optical wide-field imaging is applied. The current microscope setup was first described in [Mozooni14]. In [Holländer17] the recent achievements of quantitative imaging on the picosecond scale are demonstrated. Fig. 4.2 shows the illumination path of a magneto-optical wide-field microscope. Here, a pulsed laser illumination system is used: A Nd:YVO_4 laser is diode-pumped, passively mode-locked and frequency doubled to a wavelength of $532\ \mathrm{nm}$ and used as a light source. The laser emits short

pulses with a duration of $\Delta t_{\mathrm{pulse}} = 7\ \mathrm{ps}$ at a repetition rate of $50\ \mathrm{MHz}$. The repetition rate is fixed by the cavity-length of the laser. The pulsed laser illumination is used as a light source for stroboscopic imaging, therefore the frequency resolution of the time-resolved measurements is limited to multiples of $50\ \mathrm{MHz}$. The camera is running freely at a fixed frame rate and the time resolution is solely determined by the pulsed laser illumination. The output power of the laser is $P \approx 130\ \mathrm{mW}$. The optical output of the laser is aligned through a rotating plate diffuser with a diffusing angle of $3°$ to avoid optical contrast by laser-speckles. The diffused beam is then coupled into a multimode optical fiber with a numerical aperture of $\mathrm{NA} = 0.22$ and a core diameter of $0.5\ \mathrm{mm}$. The output of the optical fiber is then guided through a vibrational diffuser operating at $f_{\mathrm{vibr}} = 180\ \mathrm{Hz}$ with a diffusing angle of $12°$. The effective light source is then focused by a movable convex lens with a focal length of $+50\mathrm{mm}$ into the microscope. The relevant aperture planes (AP) are shown. Furthermore, a polarizer is used for s- or p-polarization of the laser ray in the microscope. After reflection on the sample, which is positioned on a coplanar waveguide (CPW), a turnable analyzer (another polarizer) and compensator ($\lambda/4$-wave-plate) are then used to project the long elliptical axis of polarization onto a reference axis. The two polarizers in the beam path are set close to extinction. In this work analyzer opening angles of about $\beta_{\mathrm{O}} \approx 4.5°$ were used. The Kerr rotation θ_{K} is linear in magnetization M and much smaller than the opening angle for a metallic thin film. By using Malus' law for almost crossed polarizers, the measured intensity is linear in $\sin^2(\beta_{\mathrm{O}} + \theta_{\mathrm{K}})$. The Kerr signal s_{K} is the difference between a dark domain D_2 and bright domain D_1

$$s_{\mathrm{K}} = D_1 - D_2 = \sin^2(\beta_{\mathrm{O}} + \theta_{\mathrm{K}}) - \sin^2(\beta_{\mathrm{O}} - \theta_{\mathrm{K}}). \tag{4.1}$$

Small angle approximation then yields

$$s_{\mathrm{K}} \approx (\beta_{\mathrm{O}} + \theta_{\mathrm{K}})^2 - (\beta_{\mathrm{O}} - \theta_{\mathrm{K}})^2 = 4\beta_{\mathrm{O}}\theta_{\mathrm{K}}. \tag{4.2}$$

The Kerr signal is then linear in magnetization. A similar derivation can be found in [Hubert08]. By adjusting the position of the movable lens, the beam path in the microscope can now be altered. By shifting the position of the lens, effectively the position of the light source is shifted in the back-focal plane of the objective lens. This shift in

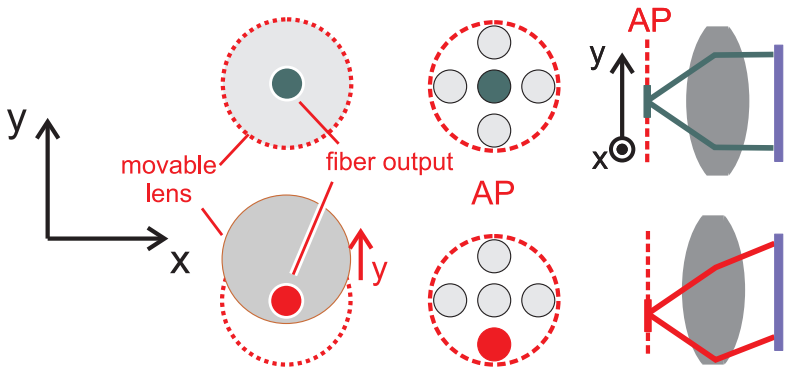

Figure 4.3: Schematic exhibiting the creation of an angle of incidence in a wide-field microscope. The green color marks normal incidence, red marks oblique incidence. This figure was adapted from [Holländer17].

position converts then into a non-zero angle of incidence towards the magnetic specimen. The reflected light is collected by the objective lens and transmitted to the camera via the observation path.

Fig. 4.3 schematically illustrates the creation of an angle of incidence in a wide-field microscope: The position of the fiber output stays constant, but the movable lens can be shifted along the x and y-direction. If it is for example shifted along the y-direction, this leads to a change of position of the effective light source in the AP along the y-axis and an angle of incidence in the y-z-plane. The maximum angle of incidence is then capped by the numerical aperture of the microscope objective. Here, an objective lens with a numerical aperture of $\mathrm{NA} = 0.6$ was used for all dynamical experiments.

Also, Fig. 4.4 exhibits the full electrical setup of the dynamical Kerr-microscope. The pulsed laser system is controlled in a loop by the timing stabilizer synchronizing the repetition to $50\ \mathrm{MHz}$ [Mozooni14]. Internally the timing stabilizer runs from a $10\ \mathrm{MHz}$-clock creating the fifth harmonic of this signal. The $10\ \mathrm{MHz}$-clock signal of the timing stabilizer can be read out and also be used as a reference signal (ref. in) for the high frequency signal generator. In this way a fixed phase relationship between the laser pulses and the signal of the signal generator can be reached. The jitter of this system is generally low $\Delta t_{\mathrm{jitter}} < 0.5\ \mathrm{ps}$. The signal generator creates sinusoidal microwave signals up to $20\ \mathrm{GHz}$ with a high voltage amplitude of up to $5\ V$ base to peak depending on the operat-

ing frequency. Optionally a high frequency amplifier can be used to boost the microwave signal. The microwave signal is then fed through a broadband impedance matched CPW creating a homogeneous Oersted-field distribution on top the CPW [Chumakov05]. The CPW consists of a $160\ \mu\mathrm{m}$ wide and $17.5\ \mu\mathrm{m}$ thick center conductor and a ground-plane. High amplitude microwave currents up to a base to peak amplitude of $I_\omega = 0.1\ \mathrm{A}$ can be used to generate the microwave field at the fixed input impedance of $50\ \Omega$. The alternating microwave magnetic fields can be as high as $300\ \mathrm{A/m}$ for a sample positioned magnetic face down on the waveguide (directly on top of the center conductor). The output signal of the CPW is measured utilizing a digital sampling oscilloscope with $20\ \mathrm{GHz}$ bandwidth. The oscilloscope is triggered by the $10\ \mathrm{MHz}$ signal of the timing stabilizer. Microwave attenuators are used between CPW and oscilloscope in order to maintain a voltage lower than the maximum input voltage of the sampling oscilloscope.

By performing measurements with multiple sensitivities or with increased number of averages to capture only small changes of magnetization, the total measurement time increases. On a long time scale (multiple hours) small drifts between the laser pulses and the excitation signal become noticeable. In order to prevent these drifts and gain long time phase stability, a closed cycle of measuring and setting the phase is used. The phase of the microwave signal is read out via the sampling oscilloscope. A fast and reliable way to read out the phase of the microwave signal is the creation of the fast Fourier Transformation (FFT) and measurement of the phase at the excitation frequency. In order to correct for small drifts, the zero-point of the phase can be read out first. Then, the desired phase is corrected by the new zero-point as a linear phase offset and actuated directly. Each zero-point is used only for one differential image. The phase accuracy for this zeroth-order correction scheme is approximately $\Delta\phi = \pm 0.02$ corresponding to a time resolution of $\Delta t_{\mathrm{phase}} = \pm 1.5\ \mathrm{ps}$ at an excitation frequency of $f = 1.9\ \mathrm{GHz}$. The temporal resolution of the combined system can be written as

$$\Delta t = \sqrt{\Delta t_{\mathrm{pulse}}^2 + \Delta t_{\mathrm{jitter}}^2 + \Delta t_{\mathrm{phase}}^2} = 7.2\ \mathrm{ps}. \tag{4.3}$$

This corresponds to a bandwidth well above $50\ \mathrm{GHz}$. The new timing algorithm is a prerequisite for vector measurements of magnetization, because even after averaging a certain amount of time for one specific phase, the phase remains stable and can be

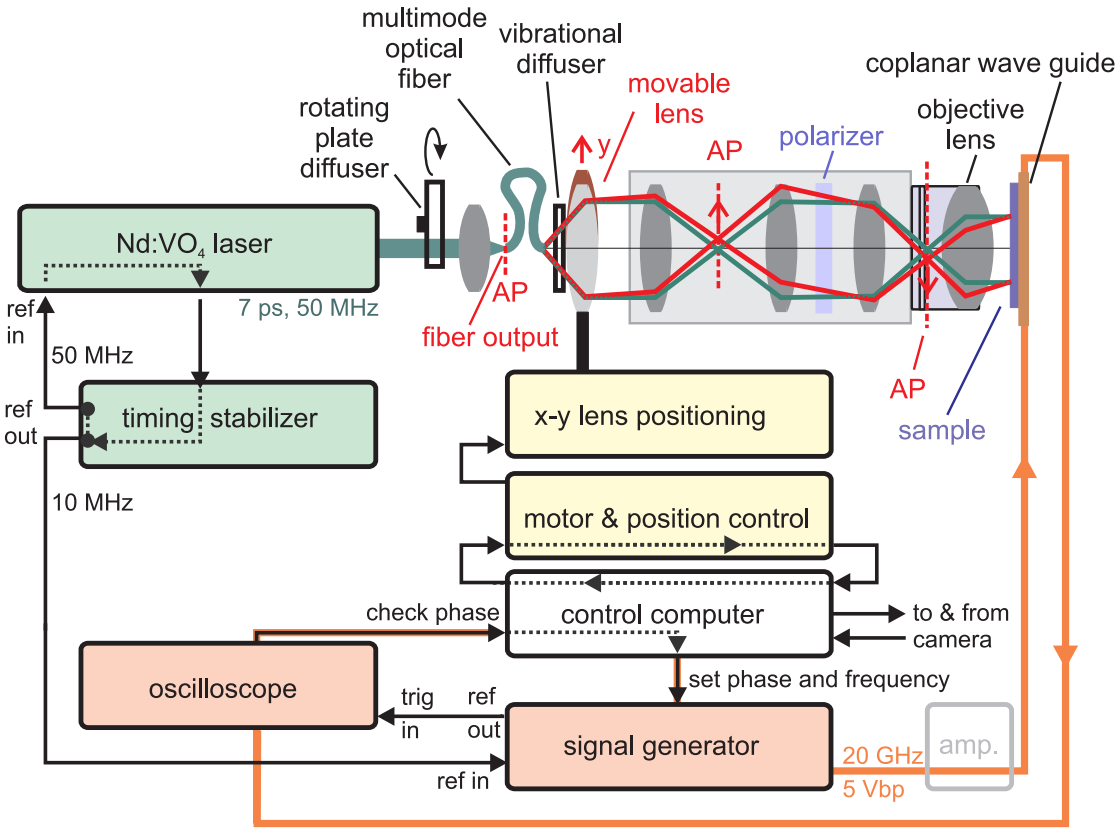

Figure 4.4: Detailed electrical setup of the utilized microscope: The laser system is controlled in a loop by the timing stabilizer. The signal generator runs from the timing stabilizers internal 10 MHz clock and creates an electrical signal with a fixed phase to the laser pulses. The microwave signal is then guided through a coplanar waveguide (CPW). The CPW generates a quasi-homogeneous Oersted-field on top of the waveguide exciting coherent magnetization dynamics in the sample, which can be imaged via the laser illumination system. The through the waveguide transmitted signal is read out via a digital sampling oscilloscope and controlled via the computer. The movable lens is positioned via a biaxial motor system. This figure was adapted from [Holländer17].

correlated with a measurement from a different sensitivity. Another prerequisite for acquiring the low-signal dynamic data as described is the mechanical stability: Therefore, the microscope stand is made of a high mass granite block, on which the sample stage and focusing unit are mounted. The optical microscope setup is mounted on an optical table and shielded by a box from air convection, thermal drift and acoustic noise. The granite block and the ambient noise shielding allow for measurement durations up to several hours under stable conditions.

4.2 Calibration by Static MOKE Imaging

In order to calibrate the dynamic response, static measurements of the magnetic specimen are required. In particular, each sensitivity measured with oblique incidence is characterized by its corresponding sensitivity curve containing the dependence of the intensity on the magnetization orientation [Rave93]. The sensitivity curve can for example be obtained by saturating the sample along multiple orientations and evaluating the corresponding intensity. Another approach towards obtaining the sensitivity curve is utilizing a magnetization distribution, where at least three different magnetization orientations are known. These three orientations can then be used to calibrate the dependence of magneto-optical intensity versus magnetization orientation. In this chapter, the latter approach will be used.

To demonstrate dynamic magneto-optical vector-imaging, a sample of amorphous $Co_{40}Fe_{40}B_{20}$ stripes with dimensions of $40\ \mu\mathrm{m} \times 1\ \mathrm{cm} \times 120\ \mathrm{nm}$, deposited on a $800\ \mu\mathrm{m}$ thick glass substrate is chosen. Furthermore, the complete stack contains a $5\ \mathrm{nm}$ thick Ta seed layer and a $3\ \mathrm{nm}$ thick Ru capping layer to avoid oxidation and corrosion. The induced uniaxial anisotropy of $K_\mathrm{u} = 1300\ \mathrm{J/m^3}$ is aligned in the film plane by applying a magnetic field of $H_\mathrm{dep} = 8\ \mathrm{kA/m}$ during deposition of the magnetic layer. The anisotropy axis is aligned perpendicular to the long stripe axis. The stripes were patterned by standard photo lithography and selective ion beam etching. Fig. 4.5 shows five static MOKE images in five different sensitivity directions and the extracted sensitivity curves. The magneto-optical images were obtained using a standard differential imaging technique [Hubert08, McCord15] requiring to break the current domain state.

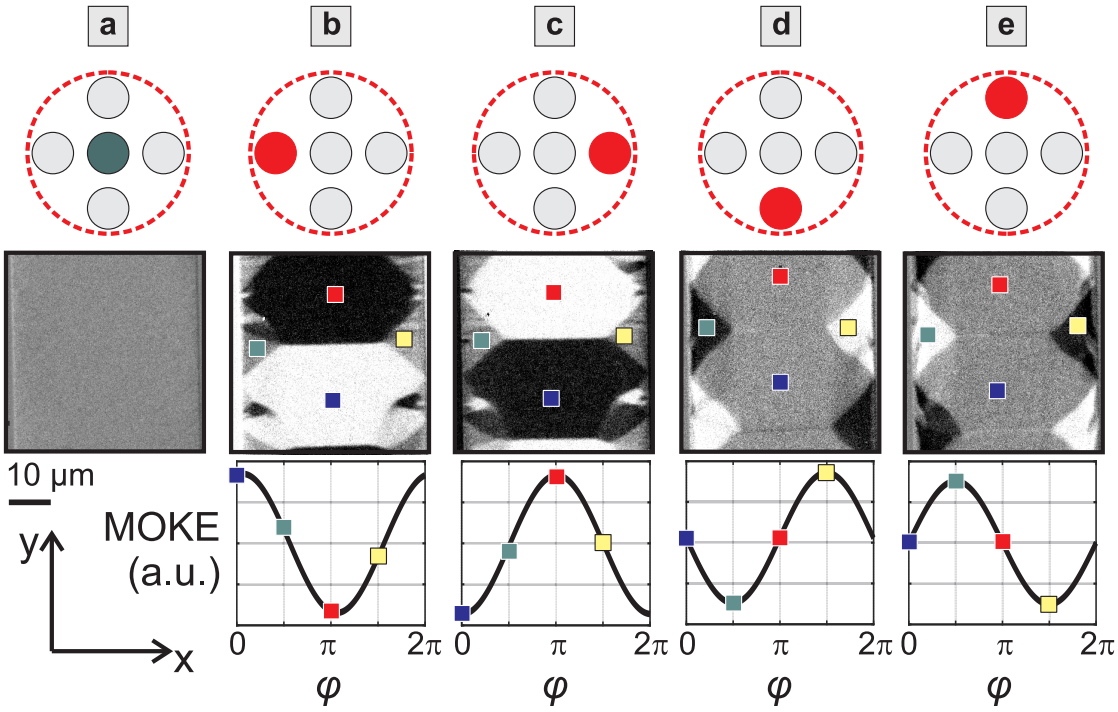

Figure 4.5: Calibration by static MOKE imaging: A known magnetization configuration similar to a Landau state is utilized to obtain the magneto-optical calibration curves. a) polar illumination. b,c) two horizontal illumination states with oblique incidence in diametric arrangement. d,e) two vertical illumination states with oblique incidence in diametric arrangement. e) depicts the domain configuration used for further dynamic experiments. This figure was adapted from [Holländer17].

Each sensitivity is indicated by a schematic representation of the effective light source in the backfocal plane. In Fig. 4.5a a MOKE image in polar configuration is shown. Here, the effective light source is given by the optical fiber, positioned in the middle of the backfocal plane leading to a normal incidence on the sample. In this configuration, there is vanishing low residual magneto-optical contrast of the longitudinal MOKE contrast and possibly second order magneto-optical Voigt-contrast [McCord15] contained. This is expected, because the magnetization of the soft magnetic stripe resides in the plane of the magnetic thin film. However, the in-plane magnetization in the domains is aligned parallel and perpendicular to the incident polarization leading to a minimization of the Voigt-contrast in this configuration. Fig. 4.5b,c show two horizontally aligned MOKE sensitivities with oblique incidence in a diametric arrangement. The position of the

effective light source is shifted to the left or right of the backfocal plane, respectively. As depicted in Fig. 4.3 this leads to an oblique plane of incidence and the magneto-optical sensitivity changes sign by moving from Fig. 4.5b to c. Fig. 4.5d,e show two vertically aligned MOKE sensitivities with oblique incidence in a diametric arrangement. The position of the effective light source is shifted to the bottom or top of the backfocal plane (see sketches of the backfocal plane on top in Fig. 4.5), respectively. Again, this leads to an oblique plane of incidence and the magneto-optical sensitivity changes sign by moving from Fig. 4.5d to e. The statically measured sensitivity curves show differential MOKE intensity depending on the known magnetization angle. All magnetic domain images shown in Fig. 4.5 were recorded on the same position without moving the sample. There is no polar MOKE contrast visible in Fig. 4.5a. Hence, the assumption, that there is no polar contrast in the static images of Fig. 4.5 is correct. In order to calibrate the polar MOKE contrast, a known out-of-plane magnetization is needed. Here, the polar MOKE contrast remains uncalibrated, since the experimental challenge is relatively high compared to the scientific gain. The calibration curves obtained with oblique incidence are fitted using a sine-function according to the expected sinusoidal longitudinal magneto-optical sensitivity. The obtained coefficients are then used for the calibration of the component-selective time-resolved measurements.

Fig. 4.5e depicts the domain configuration used for further dynamic experiments. The domain configuration shows large antiparallel domains in the middle, where the magnetization is oriented along the easy axis of uniaxial anisotropy. Closure domains at the edge of the stripe are visible, where the magnetization is oriented along the edges.

4.3 Superposition of Longitudinal and Polar MOKE in Time-Resolved Measurements

In Fig. 4.6 a data set of acquired dynamic MOKE images of the soft magnetic stripe element at an excitation frequency of $1.9\ \mathrm{GHz}$ is exhibited. Here, Fig. 4.6a shows the time evolution of the vertical longitudinal and polar MOKE contrasts, while Fig. 4.6b depicts the time evolution of the horizontal longitudinal and polar MOKE contrasts. The

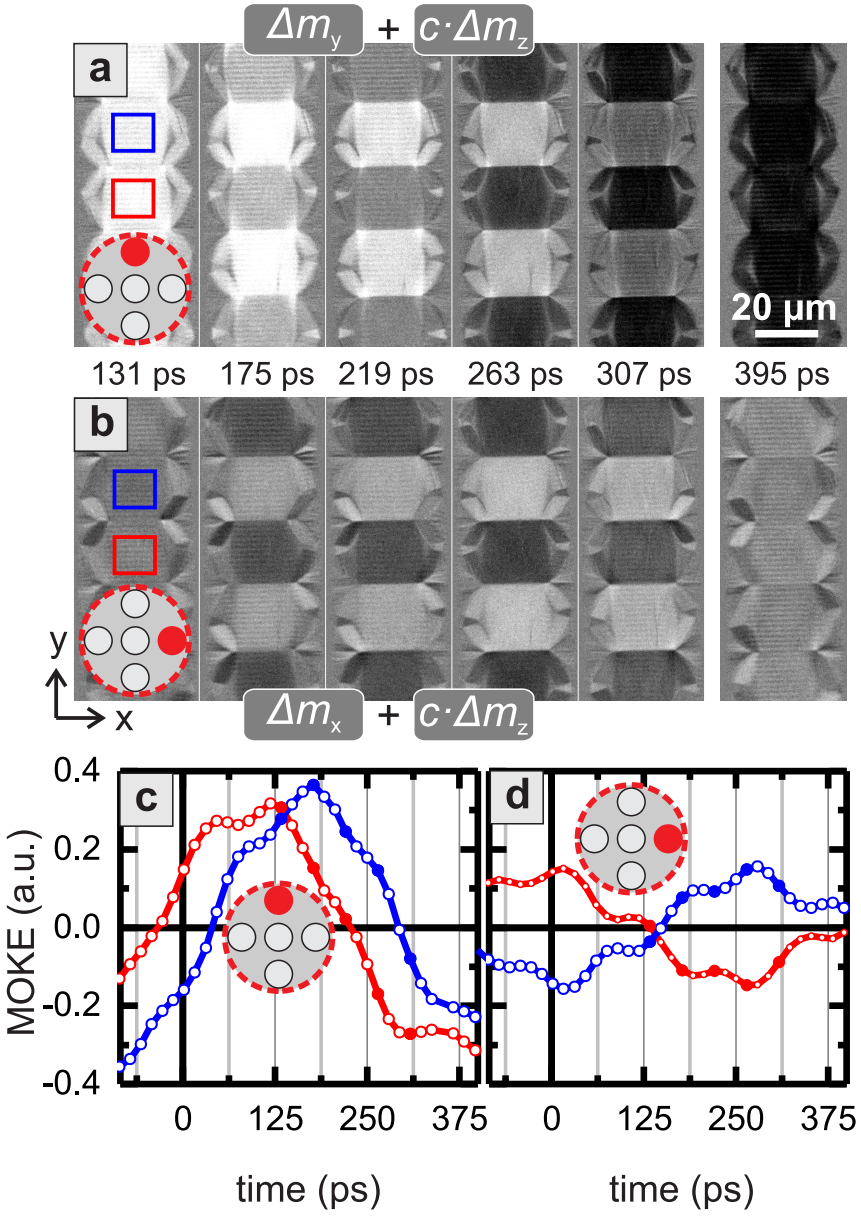

Figure 4.6: Acquired dynamic MOKE images at an excitation frequency of 1.9 GHz with different oblique planes of incidence: a) vertical incidence (s-polarized). b) horizontal incidence (p-polarized). c) average time evolution of two domains marked by red and blue frames in a) containing longitudinal and polar magneto-optical contrasts. d) average time evolution of two domains marked by red and blue frames in b) containing longitudinal and polar magneto-optical contrasts. This figure was adapted from [Holländer17].

red and blue boxes mark the domains, from which the average magnetization is plotted separately as a time evolution in the graphs Fig. 4.6c,d. Fig. 4.6c shows the time evolution of magneto-optical contrast as in Fig. 4.6a using vertical sensitivity, while Fig. 4.6d shows the time evolution of magneto-optical contrast as in Fig. 4.6b using horizontal sensitivity. The frequency was chosen as the resonance frequency of the domain precession, i.e. the magnetization in the center domains precesses uniformly around the easy axis of induced anisotropy. Before performing the dynamic measurements, the magnetic stripe element was statically initialized to the remanent state with previous saturation along the easy axis of magnetization (along the x-direction). This leads to a magnetization configuration with increased domain width compared to the equilibrium domain width. Furthermore, the axis of oscillation for the high frequency Oersted-field is aligned along the y-direction allowing for the direct excitation of the domain precession. A dynamic differential image is created by a 16 times averaged image acquired at a phase ϕ subtracted by a 16 times averaged background image of phase $\phi - \pi$ with the algorithm described in Section 4.1.2. This scheme is used for each dynamic differential image. Each differential image was then acquired 16 times and averaged again. Since the local effective field is aligned here along the easy axis of magnetization and the stripe is sufficiently thin, the magnetization of the central domains precesses elliptically around the easy axis of magnetization. In Fig. 4.6 the MOKE intensity of the vertical oblique incidence configuration shows a clear phase-shift between the domains with opposing magnetization, because of the mixed polar and longitudinal signals. The dynamic intensity of the horizontal oblique incidence measurements shows a clear phase shift of π between the two domains with opposing magnetization. Furthermore, the found signals are highly nonlinear due to the mixed MOKE signals and the influence of interacting domains despite the sinusoidal excitation field. The closure domains are aligned parallel to the oscillating excitation field and are therefore not excited directly by the oscillating field. The magnitude of the polar sensitivity is assumed to be significantly higher than the longitudinal sensitivity [McCord15]. Therefore, the dynamic images obtained with oblique incidence in Fig. 4.6 show a strong superposition of polar and longitudinal contrast. The magneto-optical intensity containing those two components can be written as

$$I_{\mathrm{MOKE,p}} = \pm I_{\mathrm{long}} + \pm I_{\mathrm{trans}} + I_{\mathrm{pol}} + I_{\mathrm{BG}}, \tag{4.4}$$

$$I_{\mathrm{MOKE,s}} = \pm I_{\mathrm{long}} + I_{\mathrm{pol}} + I_{\mathrm{BG}}, \tag{4.5}$$

where $I_{\mathrm{MOKE,p}}$ and $I_{\mathrm{MOKE,s}}$ are the magneto-optical intensities for p-polarized light or s-polarized light, respectively. Further quantities are the longitudinal intensity I_{long}, the transverse intensity I_{trans} and the polar intensity I_{pol}. The background intensity I_{BG} contains the non-magnetic information. In this work all dynamic images were recorded in a way that the horizontal incidence was p-polarized and vertical incidence s-polarized. The longitudinal and transverse intensities change sign under reversal of the angle of incidence, as already mentioned in Section 4.2 for the sign change of the calibration curves.

4.4 Component-Selective Imaging

As previously discussed, when performing dynamic measurements in the MOKE configuration with oblique incidence, there is a significant polar contribution. In order to untangle both sensitivity directions, it is suitable to perform a second measurement to calculate the pure out-of-plane and pure in-plane contrast. Untangling the two contributions with just one sensitivity is only feasible for special cases as for example in a mirrored domain state [Mozooni14] and requires preexisting knowledge about the sample and its dynamic behavior. When performing dynamic measurements for two magneto-optical sensitivities in a diametric arrangement, the sign of the longitudinal effect changes, while the polar contribution remains constant. Therefore, the two measurements can be added and subtracted leading for s-polarized light to

$$I_{\mathrm{MOKE,polar,+}} = 2I_{\mathrm{pol}} + 2I_{\mathrm{bg}} \text{ and} \tag{4.6}$$

$$I_{\mathrm{MOKE,long,-}} = 2I_{\mathrm{long}}. \tag{4.7}$$

$I_{\mathrm{MOKE,polar,+}}$ is the out-of-plane intensity obtained by adding diametric sensitivities, $I_{\mathrm{MOKE,long,-}}$ is the intensity containing only longitudinal contrast obtained by subtracting two diametric sensitivities. Fig. 4.7 exhibits a set of dynamic out-of-plane images recorded with three different methods. Fig. 4.7a shows an out-of-plane time-evolution of the magnetic stripe element measured in the polar MOKE configuration, while Fig. 4.7b shows the out-of-plane time-evolution by measurement of two diametric vertical sensitivities and addition of both with weighting coefficients extracted from the sensitivity curves.

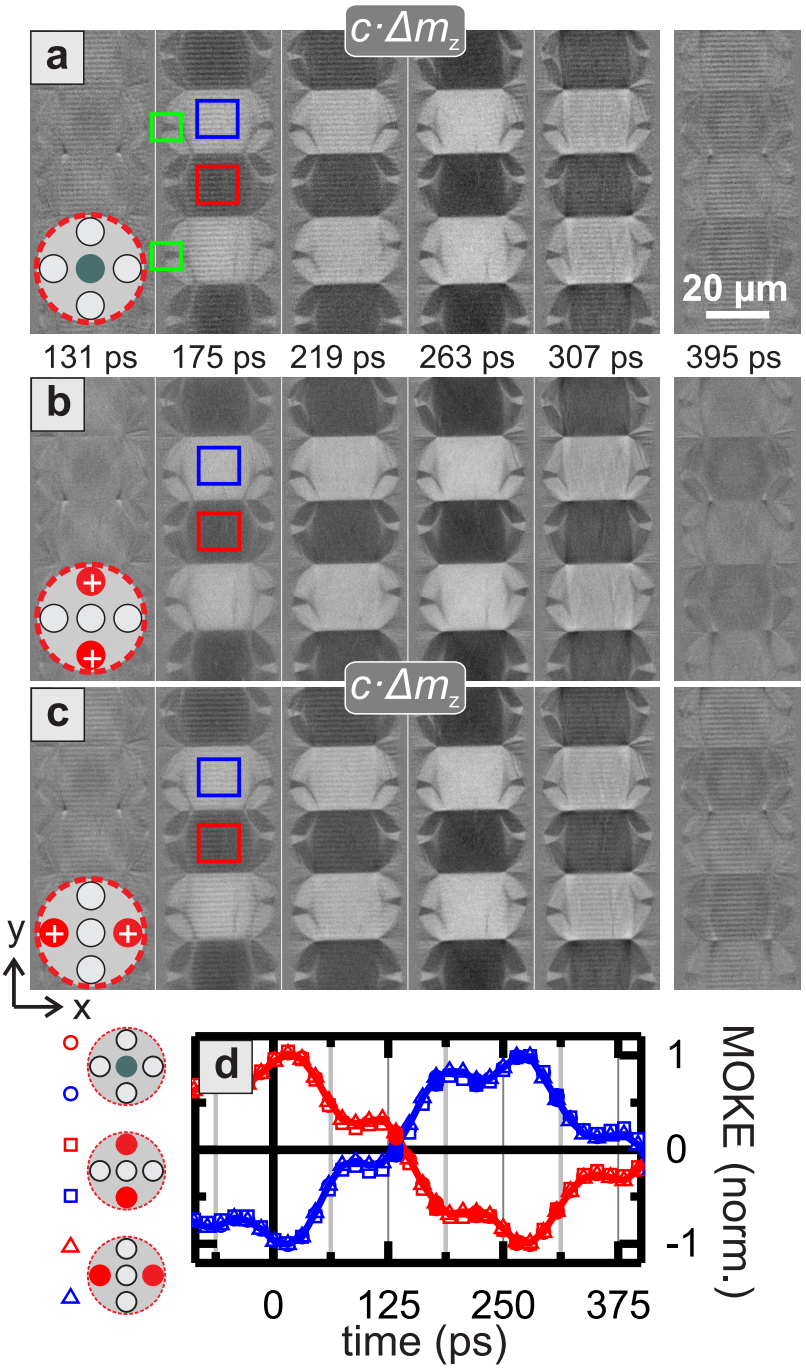

Figure 4.7: Out-of-plane contrast acquired by three different methods: a) measured in polar MOKE configuration b, c) measured in two configurations with oblique incidence and calculated by adding the two weighted separate measurements with oblique incidence for b) horizontal incidence and c) vertical incidence d) comparison of dynamic intensities achieved by each method in two domains with opposing magnetization (see red and blue box in a-c)). This figure was adapted from [Holländer17].

Furthermore, Fig. 4.7c shows the out-of-plane contribution calculated from measurements in two horizontal diametric sensitivities. All five sensitivities were recorded in one measurement cycle, therefore the timescale is comparable. In Fig. 4.7d the time-evolution of the intensity obtained by averaging in two domains with opposing magnetization (red and blue box in a-c). The gray scale and the domain response of the polar measurement were adjusted here, in order to gain direct comparability. As can be seen the three methods of obtaining pure dynamic out-of-plane contrast are in excellent agreement. The two evaluated domains with opposing magnetization show an alternating contrast with a phase shift of π indicating a precession around the easy axis of magnetization confined to the center domains. An oscillation of higher order is superposed with the sinusoidal signal, which might be related to the non-equilibrium arrangement of the magnetic domains. The static domain configuration is already magnetically charged at the «2-nodes», where two opposed closure domains meet. Small additional domains are formed in this region (see green rectangles in Fig. 4.7a, because the remanent state along the easy axis leads to a formation of wide domains, wider than the equilibrium domain width. Furthermore the presence of magnetostriction might favor the presence of these domains. These smaller domains precess with a recognizable phase shift compared to the wide domains in the center. Also, in Fig. 4.6a,c wavefronts in the out-of-plane response of the center domains can be observed. In Fig. 4.6b these waves are not recognizable. The generation of these waves in magnetization is subject of Chapter 6.

The two independent dynamic measurements enables not only the extraction of dynamic out-of-plane contrast, but also the calculation of dynamic differential pure in-plane magnetization response by subtraction of the diametric vertical and horizontal modes. By applying the calibration from Fig. 4.5, the magnetization response can be described quantitatively, normalized to saturation magnetization. In Fig. 4.8 the corresponding dynamic in-plane magnetization response is shown. Fig. 4.8a depicts the vertical dynamic in-plane magnetization response Δm_y. Fig. 4.8b shows the horizontal dynamic magnetization response Δm_x. In Fig. 4.8c the average in-plane time-evolution of magnetization response Δm_x, Δm_y is depicted for two center domains with opposing magnetization. It is evident from Fig. 4.8a that the majority of the magnetization response on the high frequency field is localized in the central stripe region. To a slightly smaller extent, also the edge regions next to the closure domains react on the external stimulus. These two regions

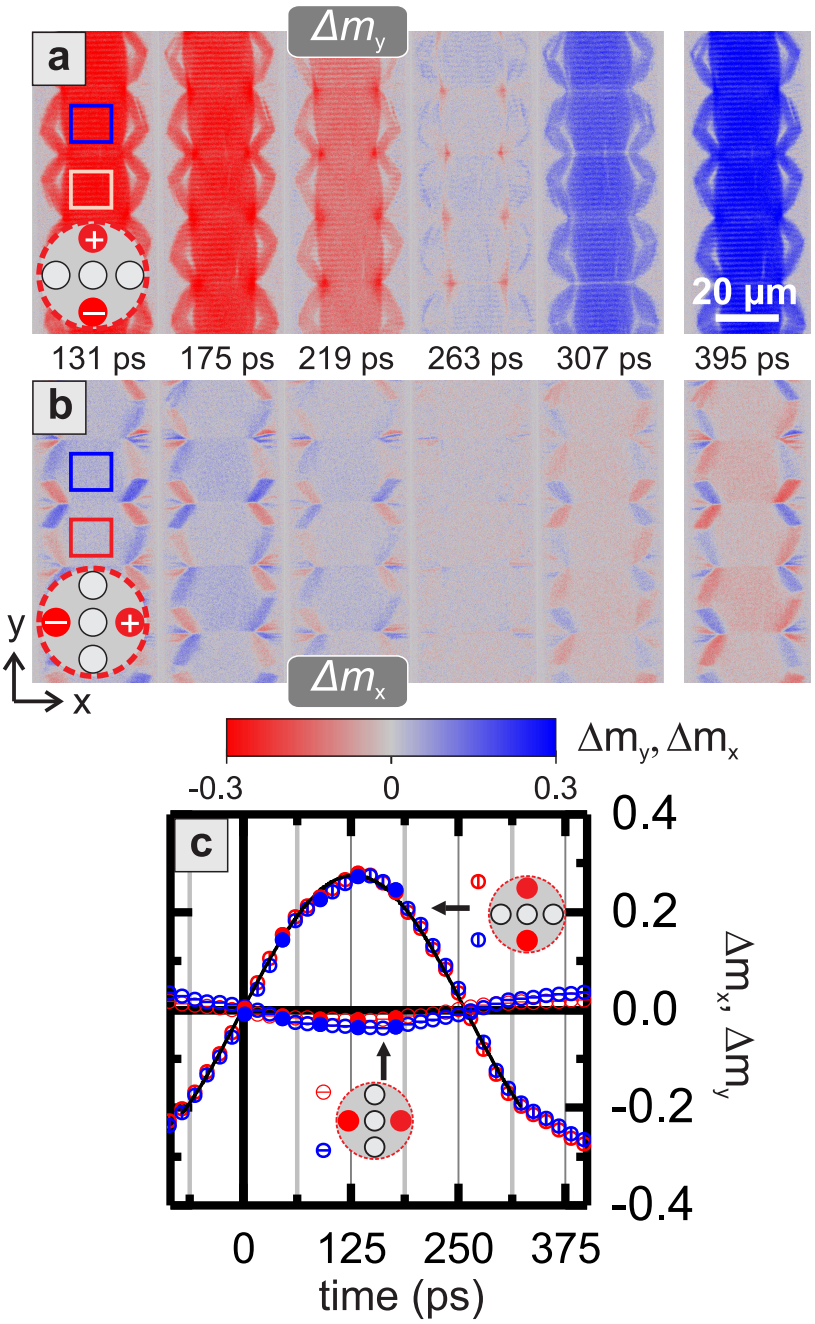

Figure 4.8: Dynamic pure in-plane measurements: a) Time-evolution of differential magnetization along the y-direction b) Time-evolution of differential magnetization along the x-direction c) evaluated intensity of two domains with opposing magnetization (compare red and blue box in a,b). This figure was adapted from [Holländer17].

are separated by a low permeability region pinned on both sides to the «3-nodes», where two closure domain walls and one 180°-wall meet. The 3-node itself and a small region around react with a significant phase lag. This is best visible at the zero crossing of the center domain precession at $t = 263$ ps and it could be an indicator for a local resonance of this region. Local phase shifts can lead to increased losses. Local resonances will be discussed in more detail in Chapter 5 on different samples. As discussed in Section 4.3, the closure domains do not react, since their magnetization is aligned parallel to the stimulus. In Fig. 4.8b the horizontal magnetization response exhibits a strong and alternating response in close proximity to the closure domains. In this region, the magnetization is slightly tilted and pinned by the closure domains leading to a different dynamic response compared to the central region of the stripe. Only little residual dynamic magnetization response can be seen in the central region of the stripe along the x-direction (Fig. 4.8c), which might be related to a slightly tilted anisotropy or simply might reflect the angular resolution of the method. Furthermore, the waves in magnetization (first recognized in Fig. 4.6a,c are present in the y-component of magnetization response, but not in the x-component. All in all, the magnetic high-frequency response is already complex even for this rather simple domain structure, therefore quantitative imaging techniques are needed.

4.5 Vector Dynamic In-Plane Response

Since both components of the in-plane magnetization response are known, the condition for depicting the lateral in-plane vector-response is given. Fig. 4.9 displays this data in a color coded vector map. The vector color coding highlights more details, which could not be observed easily before: Horizontal modes (blue, yellow) are excited in the closure domains in close proximity to the 3-node, vertical modes in the center domains (purple, green) and mixed vertical and horizontal modes at the boundary to the closure domains (purple, green) and (orange, blue). The previously discussed behavior of magnetization response is also evident here. These features are not distinguishable in the simple measurements with superposed longitudinal and polar contrast (compare Fig. 4.6). Using a combination of pure in-plane vector data and polar magnetic contrast, all the important parts of the magnetization response can be understood. For completion, the polar out-of-plane data could be calibrated in the future by measuring a known

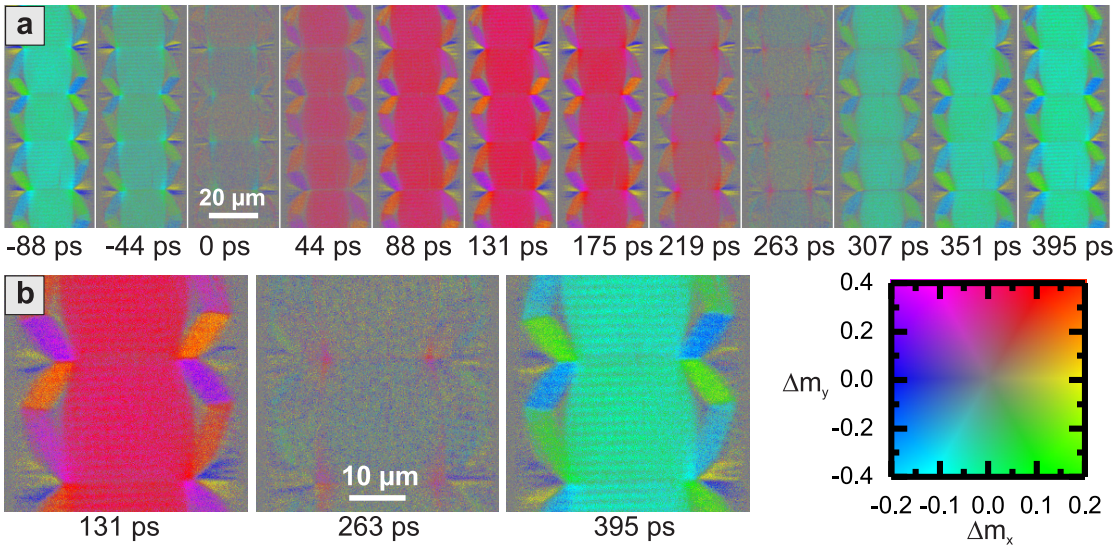

Figure 4.9: Vector dynamic in-plane magnetization response: a) Time evolution of Δm_y and Δm_x in vector response images b) exemplary details from a). This figure was adapted from [Holländer17].

out-of-plane magnetization, but nevertheless the pure in-plane magnetization response provides quantitative information to extract all relevant parameters to this work.

4.6 Summary

A highly sophisticated magneto-optical microscope was described in its key-features. The pulsed laser illumination system allows for stroboscopic measurement of magnetization dynamics at high excitation frequencies. The timing algorithm secures long-time stability of the electrical input signal and therefore enables long integration times for the acquired magneto-optical signal. It is a precondition for quantitative imaging, because it enables recording and correlating phase-stable dynamic images. The motorized altering of the beam path opened up a new chapter of magneto-optical in-plane vector measurements. As shown here, the system is capable of experimentally investigating spatial and temporal magnetization response and paves the way for understanding the interaction of magnetic micro-structures and spin waves. An in detail investigation of such dynamics is given in Chapter 6. Furthermore, the imaging scheme presented here might be applicable to other magnetic imaging techniques.

5 Local Asymmetry and Non-Homogeneous Ferromagnetic Resonance

The integral high-frequency response of a magnetic material can be measured using inductive ferromagnetic resonance techniques in the time and frequency domain. Here, pulsed inductive microwave magnetometry (PIMM) [Kos02] is introduced to obtain high frequency permeability spectra. The magnetic properties of a full magnetic thin film are analyzed. Also, continuous wave ferromagnetic resonance (CW-FMR) [Ding04] is described for the application towards symmetry broken thin films. Quantitative magnetic domain images and PIMM spectra are shown in order to discuss the effect of a locally broken symmetry on a thin ferromagnetic film. A diamond-shaped antidot thin film is investigated using component-selective magneto-optical wide-field imaging, exhibiting new functionality by bistable remanent magnetization states: By switching between remanent states, different local effective fields are present leading to a variation in local and integral resonance frequency.

Magnetic microwave materials are applied in components as magnetic-field-tunable band-stop filters [Yang15b, Song09, Salahun02, Cramer00, Harward14, Kuanr05, Kuanr03, Tsai05, Tsai99, Li15], circulators [Saib05, Adam02] or phase-shifters [Kuanr03, Saib05, Adam02]. Following the approach of switching domain configurations without the necessity to permanently apply an external magnetic field could lead to new energy-efficient switchable magnetic microwave components.

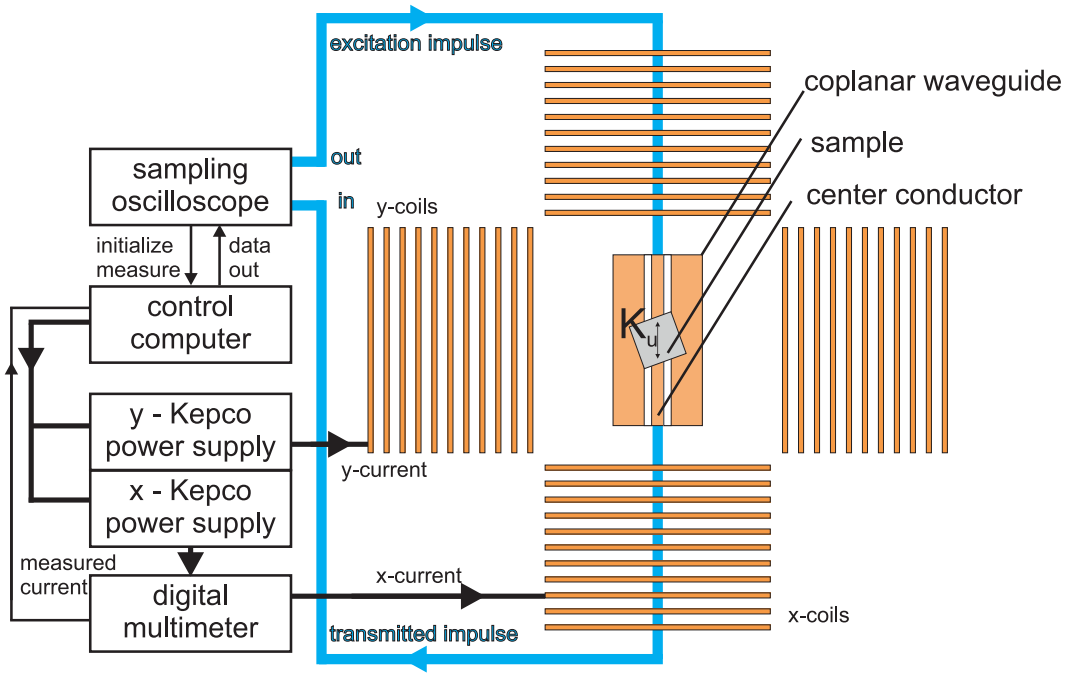

Figure 5.1: Experimental Setup for Pulsed Inductive Microwave Magnetometry (PIMM): A magnetic sample is placed magnetic face down on a coplanar waveguide aligned with the easy axis of magnetization along the center conductor. A magnetic field can be applied in the plane of the sample along two axes by the x-coils and y-coils. The coils are powered by two Kepco power supplies. The TDR-module of a digital sampling oscilloscope is used for sending an excitation impulse through the coplanar waveguide. The transmitted impulse is then detected on the second port of the oscilloscope. A digital multimeter is used to probe the current in the x-coils.

5.1 Ferromagnetic Resonance Experiments

5.1.1 Pulsed Inductive Microwave Magnetometry

In order to gain an understanding of the high frequency permeability of a magnetic material, various techniques exist such as the commonly used VNA-FMR (vector network analyzer - ferromagnetic resonance). Generally, these techniques rely on application of a microwave field and an inductive pick-up of the change in magnetization. Here, PIMM (pulsed inductive microwave magnetometry) [Silva99, Kos02] is applied to characterize the inductive high frequency field response. Instead of measuring the permeability di-

rectly in the frequency domain, PIMM is based on the measurement of the step response in the time domain. Fig 5.1 shows a schematic representation of the utilized PIMM setup. The key element of the setup is a $20\ \mathrm{GHz}$ bandwidth digital sampling oscilloscope ›Lecroy Wave Expert 100 H‹ including two TDR-modules (time-domain reflectometry). Each TDR-module is capable of applying a TDR step impulse with a rise time below $50\ \mathrm{ps}$ and an unipolar voltage amplitude of $260\ \mathrm{mV}$. The step impulse is generated in the first module, guided by microwave cables to a CPW (coplanar waveguide), transmitted through the CPW, and guided back to the second module, where the altered step impulse is detected. The coplanar waveguide is positioned in two pairs of coils allowing for the application of magnetic fields in the plane of the waveguide. The two pair of coils are aligned with the magnetic field direction parallel and perpendicular to the center conductor of the CPW. The magnetic sample is positioned magnetic face down on the coplanar waveguide. In this work all samples are aligned in a way that the axis of uniaxial anisotropy of the sample remains parallel to the center conductor of the CPW. Two Kepco power supplies are utilized as current sources for the static magnetic field generation in the coils: A ›Kepco BOP 100-10 MG‹ for the $y-$coils and a ›Kepco BOP 15-20 M‹ for the $x-$coils. A digital multimeter ›Agilent 34410A‹ is used to record the current through the x-axis coils for calibration of the x-axis magnetic field. A control computer is used to initialize the measurements, read out the data from the sampling oscilloscope and control the static magnetic field via an PCIe-Card ›National Instruments PCIe-6321‹ (mostly a 16 bit digital-to-analog converter), which applies a voltage to the Kepco power supplies. Then the power supplies generate a current proportional to the output voltage. The CPW utilized for PIMM in this work consists of a $750\ \mu\mathrm{m}$ wide and $17.5\ \mu\mathrm{m}$ thick center conductor and a ground plane.

Fig. 5.2 shows the inductive hysteresis loops of a $50\ \mathrm{nm}\ (\mathrm{Fe_{90}Co_{10}})_{78}\mathrm{Si_{12}B_{10}}$ full film, which will be investigated in the following. The saturation along the hard axis at $1.5\ \mathrm{kA/m}$ approximately marks the anisotropy field. Also, the hard axis loop exhibits almost zero remanent magnetization. Thus, at the remanent state with previous alignment of the hard axis field, the magnetization is aligned along the axis of uniaxial anisotropy. Therefore, in a ferromagnetic resonance experiment similar spectra for the two remanent states with previous field alignment along the easy axis and along the hard axis are expected.

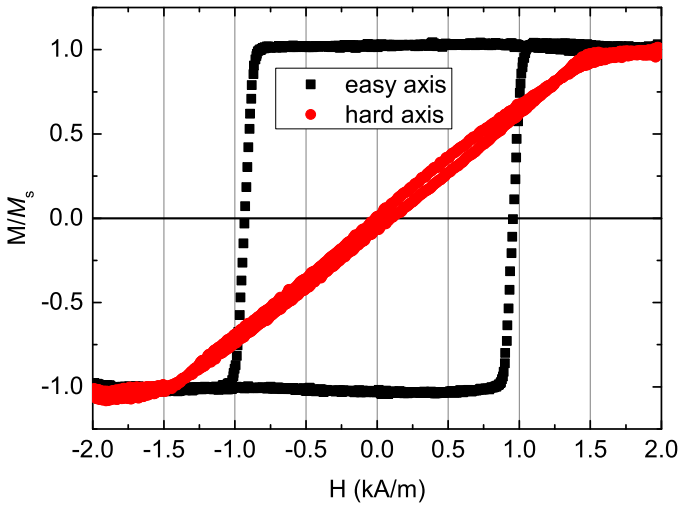

Figure 5.2: Inductive hysteresis loops along the easy and hard axis of uniaxial anisotropy for a $50\ \mathrm{nm}$ $(Fe_{90}Co_{10})_{78}Si_{12}B_{10}$ full film. The anisotropy field is approximately $1.5\ \mathrm{kA/m}$. The hard axis loop shows almost zero remanent magnetization.

An exemplary PIMM measurement of the full film is shown in Fig. 5.3. To unwrap the magnetic signal from the transmission through the waveguide, two measurements are required: one signal impulse containing magnetic and non-magnetic information and one background impulse containing only non-magnetic information. A transmitted impulse containing magnetic and non-magnetic information is depicted in Fig. 5.3a. For this impulse a magnetic bias field of $2\ \mathrm{kA/m}$ was applied along the x-axis. In this signal the non-magnetic information dominates. In order to obtain a transmission not containing magnetic information, a magnetic field strong enough to saturate the sample is applied along the y-axis. Then the high frequency Oersted-field of the CPW is oriented parallel to the saturated magnetization and it is assumed that no magnetization dynamics are induced in this configuration, since the saturating field is much stronger than the field impulse. The magnetic field step impulse has an amplitude of approximately $3\ \mathrm{A/m}$, calculated by an approach published in [Chumakov05]. The transmitted background impulse containing only non-magnetic information is then subtracted from the original

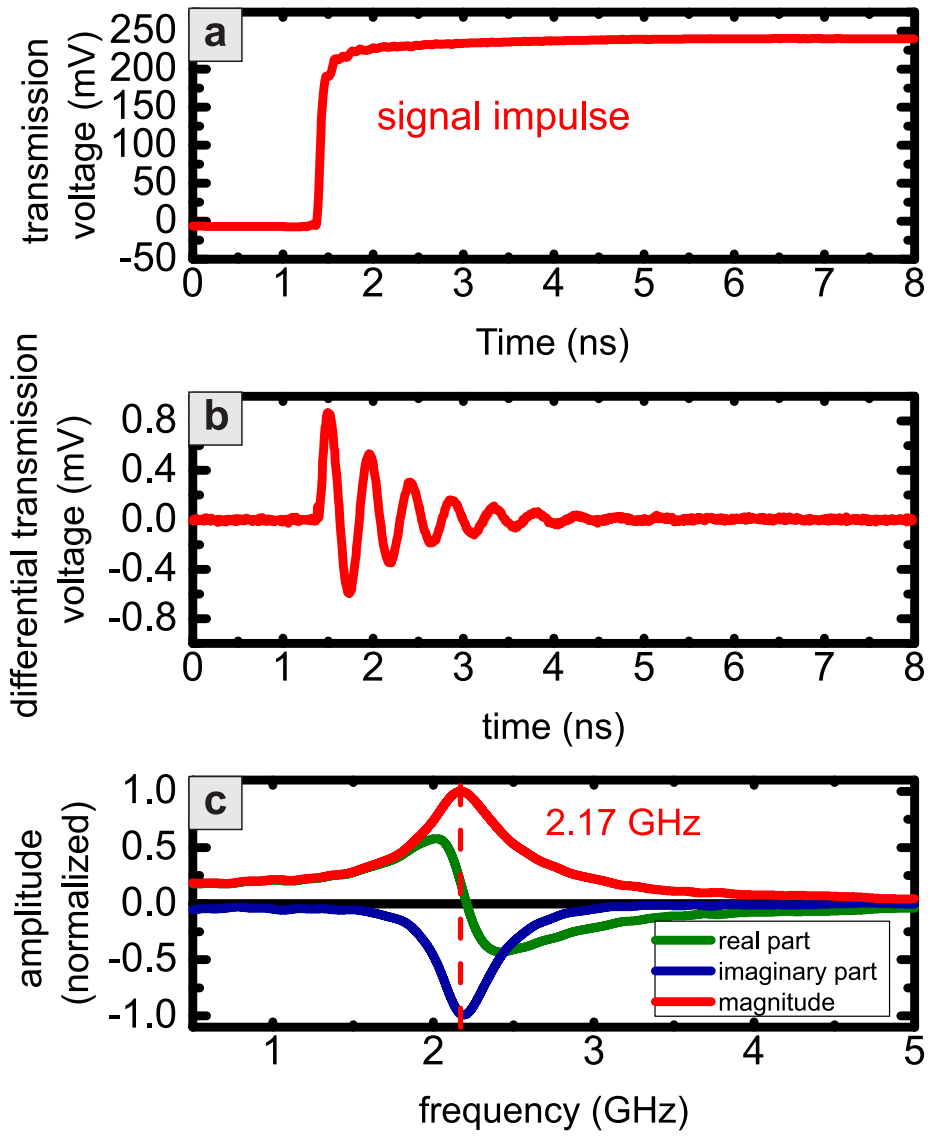

Figure 5.3: Exemplary PIMM results for the soft magnetic $50\ \mathrm{nm}\ (\mathrm{Fe_{90}Co_{10}})_{78}\mathrm{Si_{12}B_{10}}$ full film at an external field of $-2\ \mathrm{kA/m}$: a) the transmitted signal impulse, b) the differential transmission and c) the FFT of the zero-padded differential transmission are shown.

data. The obtained differential signal is then averaged over multiple measurement cycles. In Fig. 5.3b such a differential signal is plotted. The differential transmission voltage $V_t(t)$ is now proportional to the time derivative of the average magnetization [Silva99]

$$V_t(t) \propto \frac{d\bar{M}_y(t)}{dt}. \tag{5.1}$$

Due to the step response of the magnetic material on the external stimulus the differential transmission voltage exhibits a magnetic ringing on the resonance frequency. The ringing takes the form of a damped precession described by the LLG (see Eq. 2.18). Since PIMM is sensitive to the y-component of the differential magnetization response the damped precession results in a damped sinusoidal signal [Silva99]

$$\begin{aligned} \frac{dM_y}{dt} &\approx \omega_0 M_s(\cos(\phi_0)\beta_0 \exp(-t/\tau)\cos(\omega_0 t) \\ &+ \frac{1}{2}\sin(\phi_0)\beta_0^2 \exp(-2t/\tau)\sin(2\omega_0 t)). \end{aligned} \tag{5.2}$$

Here, ω_0 is the angular resonance frequency, β_0 an amplitude factor, ϕ_0 is the effective equilibrium direction of the magnetization, M_s is the saturation magnetization, τ the relaxation time and t the time. When the magnetization is predominantly aligned along the easy axis of magnetization (parallel to the center conductor of the CPW, along the x-axis), the generation of second harmonics as described by the second term in Eq. 5.2 is suppressed. Now, the differential transmission can be used to obtain spectral information of the magnetization dynamic processes by using FFT: It is clear from the signal in Fig. 5.3b that after the experimentally relevant time of $8\ \mathrm{ns}$ the differential transmission remains on a constant level of zero, because the magnetization has found a new equilibrium orientation and the ringing has totally decayed. Using this information, the signal can be zero-padded meaning, that more zeros can be added after the experimental data is finished leading to an artificially longer signal. This process is used to decrease the spacing between frequency points Δf in the FFT of the signal. In Fig. 5.3c the FFT of the zero padded differential transmission (compare Fig. 5.3b) is shown. The zero padding leads to an artificially lower amplitude of the signal. Therefore, the FFT signal is normalized to the maximum magnitude frequency per spectrum. The calculated FFT of the transmitted signal is now proportional to the frequency dependent

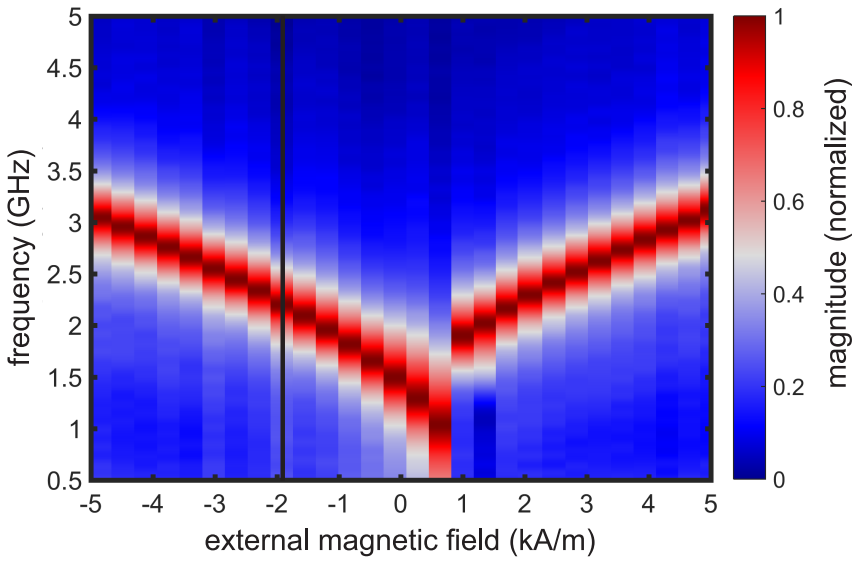

Figure 5.4: Exemplary PIMM results for the soft magnetic $50\ \mathrm{nm}\ (\mathrm{Fe_{90}Co_{10}})_{78}\mathrm{Si_{12}B_{10}}$ full film as a function of the external field and frequency. The normalized magnitude of the FFT is shown on the colorscale. Initially, the field was applied along the negative x-axis.

susceptibility [Alexander00]

$$\tilde{V}(\omega) \propto \chi_{yy}(\omega) \tag{5.3}$$

and can be compared to calculated ferromagnetic resonance spectra (see Section 2.4.1). Therefore, the aim is now to extract important parameters such as resonance frequency and magnetic damping from the experimental PIMM data. As depicted in Fig. 5.3c the maximum magnitude frequency ($2.17\ \mathrm{GHz}$) approximately marks the resonance frequency (compare Section 2.4.1). The magnetic damping can be found via [Sandler99]

$$\alpha = \frac{2}{\tau\gamma\mu_0 M_\mathrm{s}} \tag{5.4}$$

requiring knowledge of the relaxation time and the saturation magnetization by assuming a fixed gyromagnetic ratio $\gamma \approx 1.76 \cdot 10^{11}\ \mathrm{rad}/(\mathrm{MHz} \cdot \mathrm{T})$.

By measuring PIMM for different bias-fields the field evolution of the ferromagnetic resonance can be observed. This is depicted in Fig. 5.4. The colorscale corresponds to the

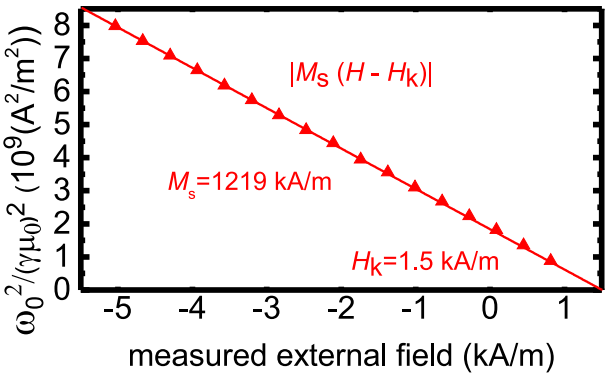

Figure 5.5: Squared left arm of the ferromagnetic resonance mode of the soft magnetic 50 nm $(Fe_{90}Co_{10})_{78}Si_{12}B_{10}$ full film. By using the Kittel-formula and fitting the resonance frequency as a function of magnetic field, the saturation magnetization can be found.

normalized magnitude of the susceptibility spectrum. Predominant is that the maximum magnitude response follows a square-root behavior as described by the Kittel formula (see Eq. 2.22). Assuming that the maximum magnitude response is approximately the resonance frequency, the extracted angular resonance frequencies can be squared and divided by $(\mu_0\gamma)^2$ following the Kittel formula resulting in

$$\frac{\omega_0^2}{(\mu_0\gamma)^2} \approx |M_s\,[H \pm H_k]\,|, \tag{5.5}$$

where the sign in front of the H_k depends on the sign of the field (positive for positive external fields, negative for negative fields). Therefore, by using a known gyromagnetic ratio and measuring field and resonance frequecy the saturation magnetization can be obtained by a linear fit as the slope connecting external field and squared resonance frequency. This was performed in Fig. 5.5. Here, the left arm of the resonance frequency was used resulting in a negative slope. The saturation magnetization was found to be $M_s = 1219\ \mathrm{kA/m}$, which is 12% higher than the value a previous study found for $(Fe_{90}Co_{10})_{78}Si_{12}B_{10}$ using the same method [Frommberger04].

This behavior can be investigated using PIMM. In Fig. 5.6 the time domain differential signal of the remanent magnetization states and the corresponding spectra are shown.

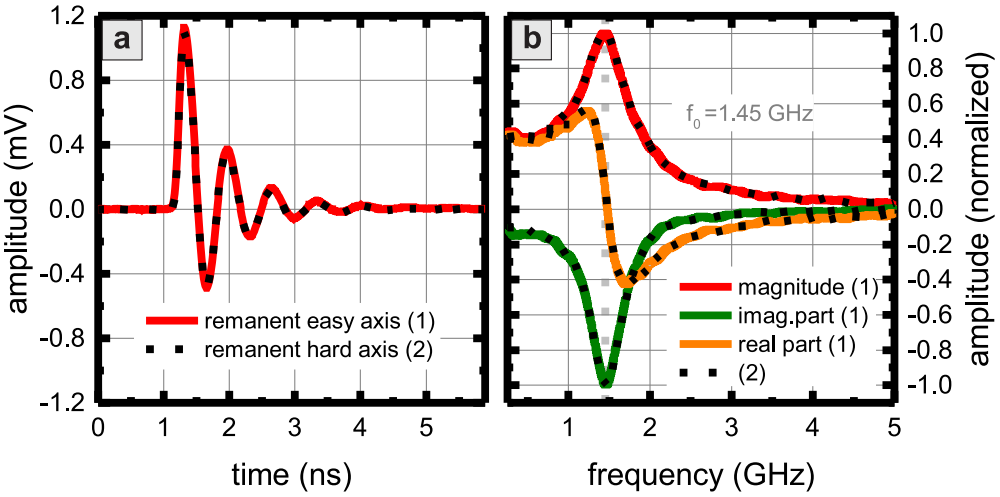

Figure 5.6: a) Time domain differential PIMM transmission of a $(Fe_{90}Co_{10})_{78}Si_{12}B_{10}$ unpatterned thin film of thickness 50 nm in the remanent magnetization configuration b) frequency domain differential PIMM transmission of a $(Fe_{90}Co_{10})_{78}Si_{12}B_{10}$ unpatterned thin film of thickness 50 nm in the remanent magnetization configurations. The resonance frequency is marked at 1.45 GHz.

The time domain signal depicted in Fig. 5.6a immediately shows the same step response of the remanent magnetization initialized with a field along the easy axis or along the hard axis. Fig. 5.6b shows the spectrum of the two remanent states. Colored lines indicate the spectrum of the remanent state with field history along the easy axis in magnitude, real and imaginary part. The black dashed lines indicate the spectrum of the remanent state with previous application of a saturating field along the hard axis. The spectra of the two magnetization configurations are in excellent agreement. The resonance frequency of the fullfilm at zero field is found to be $f_0 = 1.45$ GHz. In the following section experiments will be shown, in which the symmetry between the remanent state with previous field history along the easy or hard axis is broken by asymmetric patterning.

5.1.2 Continuous Wave - Ferromagnetic Resonance

Another technique utilized in this chapter is CW-FMR (continuous wave - ferromagnetic resonance). The experimental setup is similar to the PIMM setup in Fig. 5.1 with the exception, that the excitation is given by a microwave signal generator exciting with a sinusoidal signal instead of an impulse. Also, another CPW with a $160\ \mu\mathrm{m}$ wide center conductor was used (same CPW as used in the dynamic magneto-optical wide-field imaging). The amplitude of the excitation signal was $5\ \mathrm{V}$ converting to an excitation field of approximately $300\ \mathrm{A/m}$. Similar to the PIMM experiment, a sinusoidal transmission curve was recorded containing magnetic and non-magnetic information and a background sinusoidal transmission curve containing only non-magnetic information. Here, the background curve is recorded in a saturating field along the y-axis again. The signal and background curve are each fitted using a sinusoidal fit:

$$V_t = A \sin(\omega t + \phi), \tag{5.6}$$

where A is the amplitude parameter of the signal, ω the angular excitation frequency and ϕ a phase parameter. Using the obtained coefficients, the background curve is subtracted from the sinusoidal curve containing magnetic information resulting in a purely magnetic sinusoidal signal consisting of an amplitude and a phase parameter. The differential amplitude and phase parameter are than averaged over multiple measurement cycles. The results of this CW-FMR experiment on a thin film with broken symmetry are discussed in Section 5.3.

5.2 Local Asymmetry in a Symmetry Broken Thin Film

The objective of this study was to achieve multiple possible domain states in a patterned magnetic thin film at zero external field, which show different dynamic properties by external magnetic field history. It is interesting to switch the zero-field response, since it is more energy efficient than maintaining a magnetic bias-field during the full operation of the magnetic microwave device. For the desired zero-field soft-tuning of the dynamic properties, there are three relevant figures of merit: the resonance frequency or maxi-

mum amplitude frequency, the maximum observed shift in resonance frequency and the amplitude ratio at operating frequency. A resonance frequency, which switches between two or more relevant frequency bands, such as the L- and the S-band (long wave and short wave), would be of interest. Therefore, a high shift in resonance frequency would be required. Also, a high effect would be beneficial such as a very high, or very low amplitude ratio. To maximize the total effect a high ferromagnetic resonance absorption is desired.

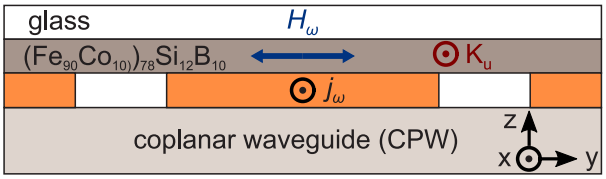

Figure 5.7: Excitation scheme: Schematic showing the cross section through the coplanar waveguide and the sample.

In order to investigate such dynamic properties, the sample of interest is placed magnetic face down on a CPW as depicted in Fig. 5.7. The axis of uniaxial anisotropy was always parallel to the center conductor of the CPW. The $(Fe_{90}Co_{10})_{78}Si_{12}B_{10}$ thin film sample (deposited on a glass substrate) is then investigated by PIMM, CW-FMR and static as well as time resolved magneto-optical wide field vector imaging. Beforehand, the static properties of such a symmetry broken thin film are discussed. Fig. 5.8 shows a SEM (scanning electron microscope) image of a $50\ \mathrm{nm}$ magnetic thin film periodically patterned by optical lithography. The structure consists of a diamond-shaped antidot lattice [Bhat13]. The lattice has a rectangular shape. Each antidot has a $3.4\ \mu\mathrm{m}$ long and a $2.2\ \mu\mathrm{m}$ short axis. The lattice constants are $16\ \mu\mathrm{m}$ along the long axis and $12\ \mu\mathrm{m}$ along the short axis. Standard domain configurations in antidot-lattices are Néel spikes [Néel88]. By choosing a rectangular lattice with two asymmetric axes instead of a square lattice, the Néel spikes along the two lattice axes have two different distances to the next Néel spike in the lattice. For closer distances of the antidots along the short axis, Néel spikes may overlap, which leads to a coupling between the antidots along this axis and the formation of a connecting domain. To form such domains, a special alignment of the uniaxial anisotropy is required. An illustration on the formation of connecting domains is shown in Fig. 5.9. By applying a moderate external field along the uniaxial

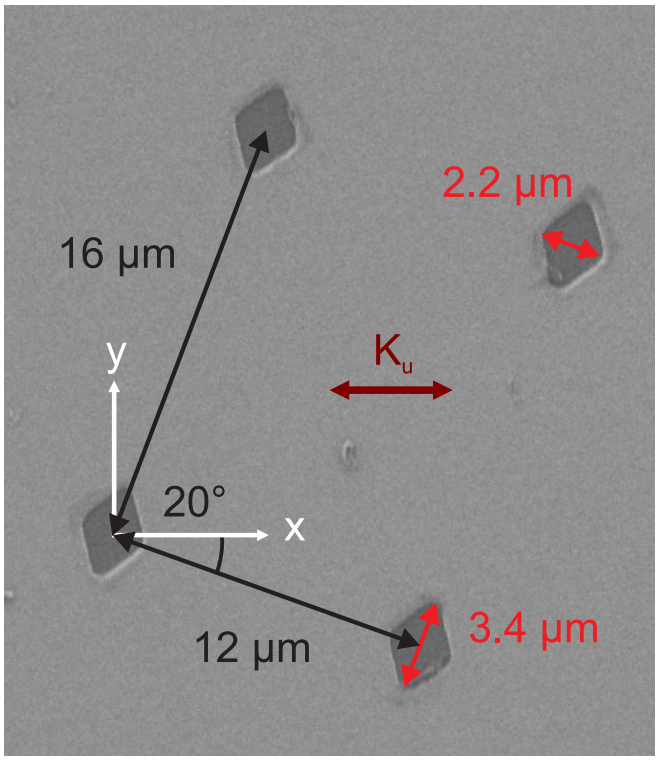

Figure 5.8: Sample design: Scanning electron microscope (SEM) image showing a patterned 50 nm $(Fe_{90}Co_{10})_{78}Si_{12}B_{10}$ film with diamond-shaped antidots.

anisotropy, the magnetization in the matrix aligns along field and anisotropy. Along the edges the magnetization is parallel to the edge. This is depicted in Fig. 5.9a. By reducing the field along the easy axis, the magnetization alignment will stay almost the same as shown in Fig. 5.9b. By applying a moderate field along the hard axis of uniaxial anisotropy, the magnetization in the matrix aligns along the external field and in vicinity of the antidots orients along the edges of the diamond-shaped antidot. In this case Néel spikes can overlap along the anisotropy direction for two faces with same magnetization in spatial proximity. By reducing the field along the hard axis, the magnetization rotates towards the easy axis. Due to the alignment of the two faces with same magnetization orientation compared to the axis of anisotropy, the magnetization in the overlapping Néel spikes rotates clockwise, while the magnetization in the matrix rotates counterclockwise due to the orientation of the free surfaces without counterpart. Along the hard axis a multi-domain state is formed.

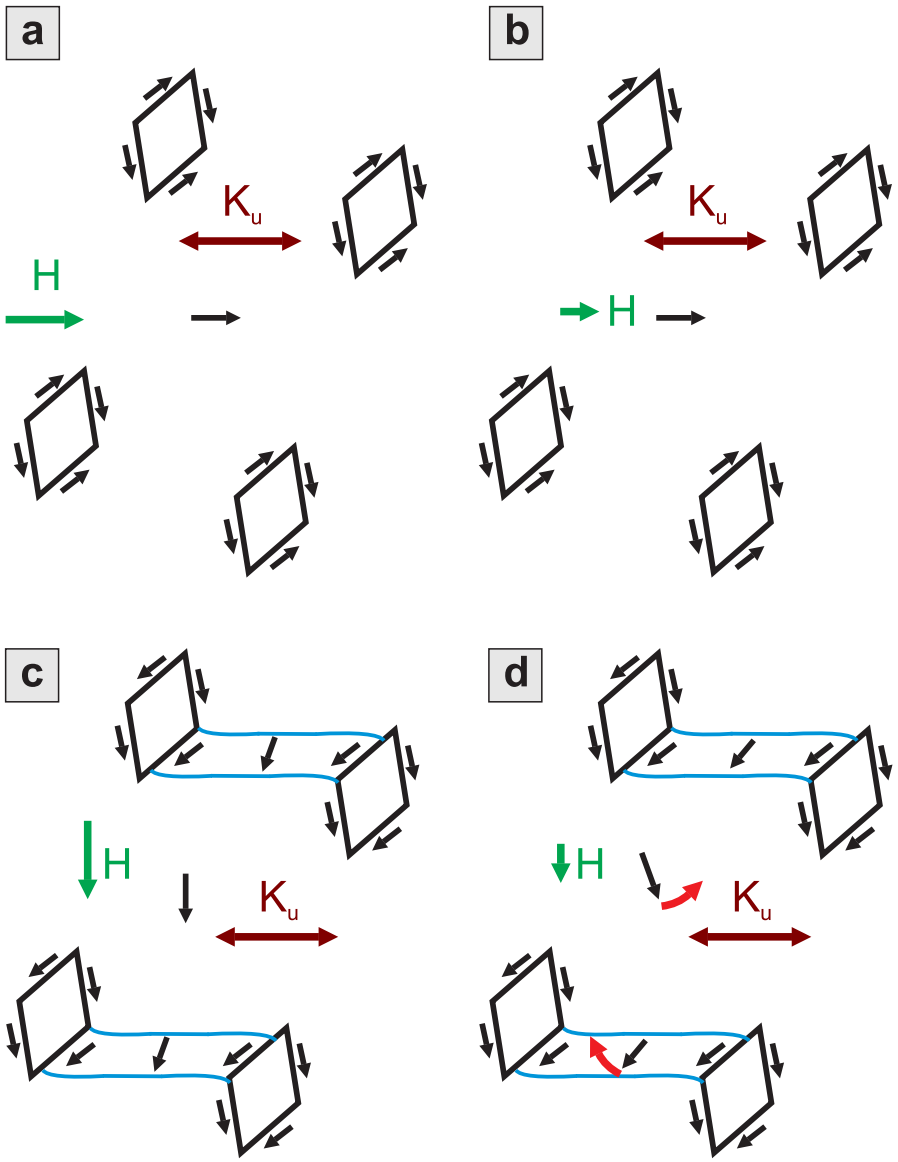

Figure 5.9: Schematic illustration (not to scale) of connecting domain formation along the patterned diamond-shaped antidot axes. a) in a moderate bias field along the uniaxial anisotropy the magnetization aligns along the edges in proximity to the antidots and along the easy axis in the matrix. b) by reducing the field along the easy axis, the magnetization in the matrix remains along this axis. c) applying a moderate field along the hard axis leads to an overlap of local effective fields for close faces with same magnetization orientation. d) by reducing the field along the hard axis, magnetization rotates into different directions leading to domain formation.

In Fig. 5.10 two different remanent states of the symmetry broken thin film are depicted in quantitative magneto-optical images containing color-coded information about the local magnetization orientation. The axis of uniaxial anisotropy is intendedly aligned with an angle of approximately $20°$ to the short axis of the antidot lattice, therefore the orientation of the lattice is turned accordingly. Furthermore, the magneto-optical imaging was performed with an objective lens with an numerical aperture of $\mathrm{NA} = 0.9$ on the magnetic top surface (not the glass top). The arrows drawn in Fig. 5.10 correspond to the approximate magnetization orientation found by analyzing quantitatively the domain wall angles. In Fig. 5.10a a remanent state is exhibited for previous application of a saturating magnetic field along the axis of uniaxial anisotropy (along $180°$) before reduction of the external field to zero. From now on this state will be called remanent easy axis state. In this state, it can be observed, that the magnetization in the matrix between the antidots is aligned approximately along the axis of uniaxial anisotropy. A small deviation between magnetization orientation in the matrix and uniaxial anisotropy can be seen and is in the order of $5°$. The locally changing demagnetizing field in the vicinity of the antidots leads to a spatially inhomogeneous magnetization distribution. At the edges of the diamond-shaped antidots the magnetization is aligned parallel to the surface allowing for the creation of slightly tilted Néel spikes. It can be seen that the Néel spikes along the long axis of magnetization overlap, but due to the anisotropy, which is almost crossed to this axis, the formation of a domain along this axis is suppressed down to small deviation from the matrix magnetization angle in the overlap region.

Another remanent magnetization configuration is depicted in Fig. 5.10b. Here, the film was saturated perpendicular to the axis of uniaxial anisotropy before reducing the external field to zero. This is the remanent hard axis state. Here, a more complex magnetization state is observed. The uniaxial anisotropy direction and the smaller distance between the antidots along the short axis allow for the creation of a domain between neighboring antidots. In the middle of these generated domains the magnetization is aligned antiparallel to the magnetization of the surrounding matrix. Modulations in these domains and in the surrounding matrix are visible due to the formation of cross-tie domain walls. In proximity to the antidot the magnetization is aligned along the short axis of the lattice resulting in a slightly curved domain wall orientation. Around the diamond-shaped antidot a complex magnetization configuration is visible including magnetic charges

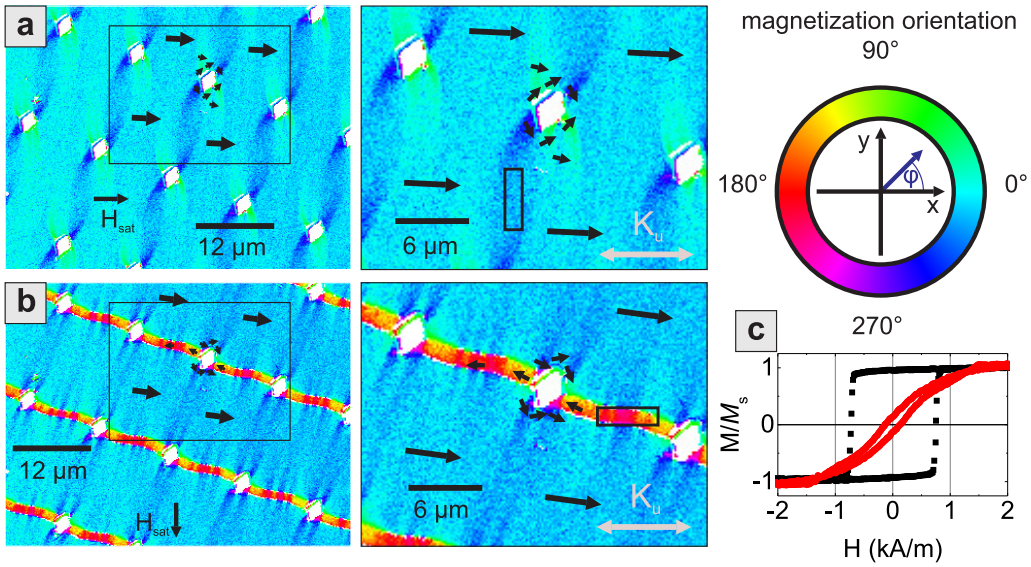

Figure 5.10: Magneto-optical vector image of the bistable remanent states in the diamond-shaped antidot patterned 50 nm $(Fe_{90}Co_{10})_{78}Si_{12}B_{10}$ film. a) remanent state after saturating along $-x$-direction and slow reduction of the field to zero (remanent easy axis state). b) remanent state after saturating along y-direction and slow reduction of the field to zero (remanent hard axis state). c) inductive hysteresis loops along easy (black) and hard (red) axis of uniaxial anisotropy of the diamond-shaped antidot sample.

at the boundary between the interconnecting domains and the edge states as well as two Néel spikes along the long lattice axis. These double spikes decay on a smaller length scale compared to the Néel spikes of the remanent easy axis state and look like a bifurcation of the magnetization pattern. The magnetization of the surrounding magnetic matrix itself is slightly tilted compared to Fig. 5.10a.

Fig. 5.10c depicts the inductive hysteresis loops of the diamond-shaped antidot patterned 50 nm $(Fe_{90}Co_{10})_{78}Si_{12}B_{10}$ film. By comparing it to the hysteresis loops of the full film (compare Fig. 5.2), it can be seen that the coercive field along the easy axis has decreased in the patterned sample. From the hard axis loop it can be seen, that the anisotropy field has stayed the same, but the remanent magnetization along the hard axis has increased. The latter is related to the patterning formation of the connecting domains along the hard axis loop. Furthermore, it can can be seen in Fig. 5.10b that the matrix magnetization is slightly tilted compared to the axis of uniaxial anisotropy due to the

locally induced demagnetization fields. All in all, breaking the symmetry of the domain pattern as anticipated in Fig. 5.9 has succeeded. The formation of connecting domains between diamond shaped antidots occurred for a previously applied field along the hard axis of uniaxial anisotropy, but not for a previously applied field along the easy axis of uniaxial anisotropy.

5.3 Inductive High Frequency Response of a Symmetry Broken Thin Film

By using field history, different domain configurations at zero field were found. In the following, the high frequency characteristics of this patterned thin film are investigated. First, PIMM is applied for the two remanent magnetization states. In order to make sure, that the right domain configurations are reproduced in the PIMM setup, after a first successful measurement, the sample was mounted in a magneto-optical wide-field microscope and a domain image was measured exhibiting the expected domain configuration. In the subsequent PIMM measurements, the resulting spectra were compared instead of the domain images. In Fig. 5.11 exemplary PIMM measurements are shown for 11 switching cycles. In each cycle a remanent easy axis configuration was measured followed by a remanent hard axis configuration. Here, the time domain signals were zero padded, but the amplitudes of the PIMM spectra were not normalized. Therefore, the amplitude of the spectrum is not to scale with the shown time domain signal, but can be directly compared with each other (all PIMM spectra in Fig. 5.11). Fig. 5.11a shows the differential transmission signal through the waveguide in the time domain for the 11 seperate measurements of the newly initialized remanent easy axis magnetization configuration. Fig. 5.11b shows the resulting magnitude spectra of Fig. 5.11a. A resonant peak at $1.3\ \mathrm{GHz}$ can be observed. Furthermore, a small plateau can be observed at $2.5\ \mathrm{GHz}$. The maximum magnitude frequency of a $50\ \mathrm{nm}$ thin film of $(\mathrm{Fe_{90}Co_{10}})_{78}\mathrm{Si_{12}B_{10}}$ without antidots from the same wafer in the remanent configuration (easy or hard) was $1.45\ \mathrm{GHz}$ (see Fig. 5.6). Therefore, the remanent easy axis state of the diamond shaped antidot sample even shows a lower maximum magnitude frequency than the corresponding full film. Fig. 5.11c shows the differential transmission signal through the waveguide in the

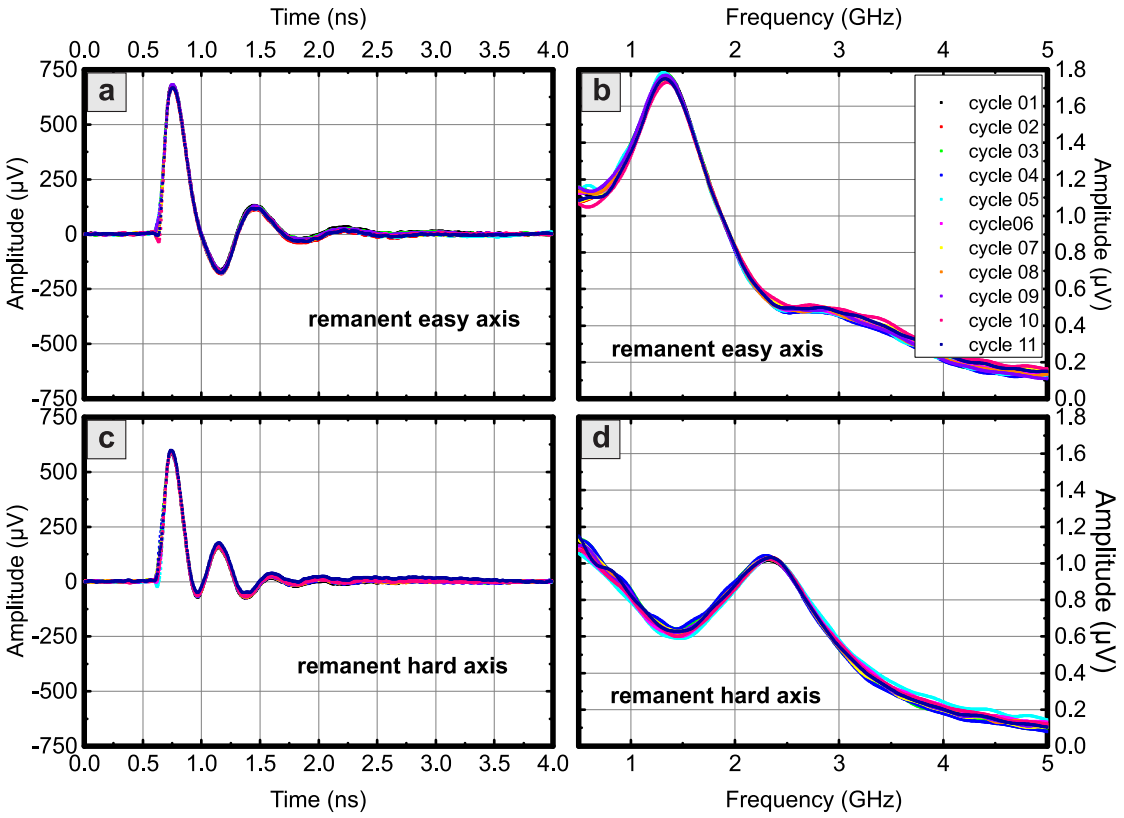

Figure 5.11: PIMM results on the diamond-shaped antidot patterned 50 nm $(Fe_{90}Co_{10})_{78}Si_{12}B_{10}$ film. Each signal was recorded for 11 cycles switching from remanent easy axis state to remanent hard axis state and back. a) Time domain signal of the remanent easy axis magnetization state ($\propto \frac{dM}{dt}$). b) Magnitude spectrum of the remanent easy axis magnetization state. c) Time domain signal of the remanent hard axis magnetization state($\propto \frac{dM}{dt}$). d) Magnitude spectrum of the remanent hard axis magnetization state.

time domain for the 11 seperate measurements of the remanent hard axis magnetization configuration. Fig. 5.11d shows the resulting magnitude spectra of Fig. 5.11c. A roll-off can be observed up to $1.5\ \mathrm{GHz}$. A resonant peak at $2.3\ \mathrm{GHz}$ can be observed. The amplitude of the peak in Fig. 5.11b at $1.3\ \mathrm{GHz}$ is significantly higher than the amplitude of the peak in Fig. 5.11d at $2.3\ \mathrm{GHz}$. An excellent reproducibility can be observed for both domain states. The magneto-dynamic response of the patterned sample deviates nicely from the full film response. The symmetry of the magneto-dynamic response was broken successfully between remanent hard and remanent easy axis states by local demagnetization effects. This was achieved by periodic patterning. To find the details of the local permeability response dynamic magneto-optical imaging is applied and the results are shown in Section 5.4.

By evaluating the maximum magnitude frequencies, the switching behavior of the diamond shaped antidot sample can be further demonstrated: Fig. 5.12 shows the maximum magnitude response as a function of the switching events (data of Fig. 5.11). Here, two switching events correspond to one cycle. Again, an excellent reproducibility of the resonant magnetic behavior can be found. The mean peak frequency is $f_{\mathrm{easy}} = 1.34\ \mathrm{GHz}$ for the remanent easy axis state and $f_{\mathrm{hard}} = 2.33\ \mathrm{GHz}$ for the remanent hard axis state. Switching fields of $4\ \mathrm{kA/m}$ were used in this experiment. Fields as low as $2\ \mathrm{kA/m}$ could be used to switch the domain structure in static magneto-optical experiments.

In order to compare these results of the pulsed excitation to continuous excitation a CW-FMR experiment was performed (see Section 5.1.2 for details on the experiment) for both magnetization configurations at $1.3\ \mathrm{GHz}$ and $2.3\ \mathrm{GHz}$. For the remanent easy axis state, the change in amplitude was $-17\ \mathrm{V/m}$ at $1.3\ \mathrm{GHz}$ and $-22\ \mathrm{V/m}$ at $2.3\ \mathrm{GHz}$ (compared to the $5\ \mathrm{V}$ base to peak excitation amplitude). For the remanent hard axis state, the change in amplitude was $-10\mathrm{V/m}$ at $1.3\ \mathrm{GHz}$ and $-24\ \mathrm{V/m}$ at $2.3\ \mathrm{GHz}$. For the inductive experiments, the center conductor of the waveguide was covered over a length of $4.2\ \mathrm{mm}$ with the ferromagnetic sample. These values indicate the possibility of tuning the absorption.

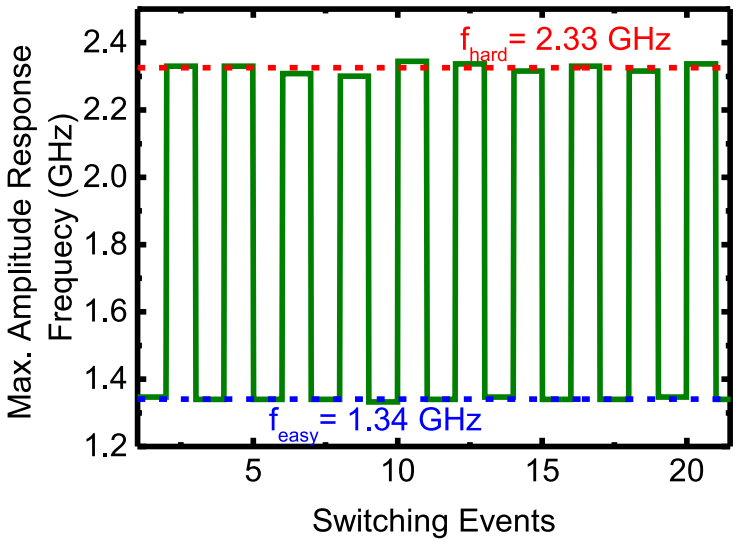

Figure 5.12: Switching of the maximum magnitude response frequency as a function of switching events (switching from remanent easy axis state to remanent hard axis state or back).

5.4 Dynamic Magneto-Optical Investigation of Local Resonances in a Symmetry Broken Thin Film

To reveal the nature of the integral resonance switching, time-resolved magneto-optical wide-field vector imaging is applied (see Chapter 4) to the sample. Here, the magneto-optical calibration curves are found by saturating the sample and rotating the field. For a more deep understanding of the local resonance frequencies it is of key interest to characterize the local phase compared to the excitation, since it can qualitatively reveal the position of the local resonance in the local spectrum. In order to find the time or phase offset between the local dynamics and the excitation phase, a calibration experiment was performed: the $(Fe_{90}Co_{10})_{78}Si_{12}B_{10}$ full film was measured with a bias field of $10\ \mathrm{kA/m}$ shifting its resonance frequency far above the maximum excitation frequency at $1.3\ \mathrm{GHz}$ and $2.3\ \mathrm{GHz}$. After finding the local phase for the particular position on the waveguide, the diamond-shaped antidot sample was measured integral

on this position resulting in a corresponding phase shift between excitation and full sample response. The resulting phase offset (obtained by fitting a cosine function) was considered in graphs Fig. 5.13 and 5.14. Fig. 5.13 shows the time-resolved magneto-optical investigation of the remanent easy axis state. First, the local phase and amplitude will be discussed qualitatively, followed by a quantitative analysis of the phase shifts. In Fig. 5.13a the static configuration used in the dynamic experiment is depicted. This static domain image was recorded with a vertical sensitivity. Three domains are marked in the static configuration. Domain 1 corresponds to the matrix aligned along the uniaxial anisotropy, domain 2 to the interconnection between the antidots along the short lattice axis and domain 3 is the interconnection between the antidots along the long lattice axis, where the Néel spikes overlap for the remanent easy axis state. The two maximum amplitude frequencies from PIMM are chosen for a more deep investigation: $1.3\ \mathrm{GHz}$ and $2.3\ \mathrm{GHz}$. In Fig. 5.13b the dynamic in-plane vector response of the remanent easy axis configuration is shown for an excitation frequency of $1.3\ \mathrm{GHz}$ and a utilized field amplitude of approximately $H_\omega = 300\ \mathrm{A/m}$ along the y-axis. It can be seen, that domain 1 and and domain 2 show a similar dynamic vector response - a precession around the easy axis of magnetization. In contrast, domain 3 shows only a small magnetic in-plane response for all phases. Fig. 5.13c displays the dynamic in-plane vector response of the remanent easy axis configuration for an excitation frequency of $2.3\ \mathrm{GHz}$ and a utilized field amplitude of approximately $H_\omega = 300\ \mathrm{A/m}$ along the y-axis. While domain 1 and domain 2 still show a precession with a similar phase, domain 3 shows a stronger oscillation than at $1.3\ \mathrm{GHz}$ with a clear phase shift compared to domain 1 and domain 2. This can be explained with a locally higher resonance frequency in domain 3: The overlapping Néel spikes lead to higher local effective fields resulting in a higher resonance frequency. By closely looking at the PIMM spectrum in Fig. 5.11b, a second peak can be observed at approximately $2.7\ \mathrm{GHz}$ with a small amplitude. In Fig. 5.13d the average Δm_y component is plotted as a function of the phase of the excitation field for the three individual domains and for the response of the full frame at $1.3\ \mathrm{GHz}$. Here, the response of domain 1 and domain 2 is high, almost in-phase and similar in amplitude. Domain 3 shows a significantly lower response and has a small phase shift to domain 1, domain 2 and the full frame response, which is dominated by the response of domain 1 and domain 2. Fig. 5.13e shows the average Δm_y component as a function of the phase of the excitation field for the three individual domains and for the response of

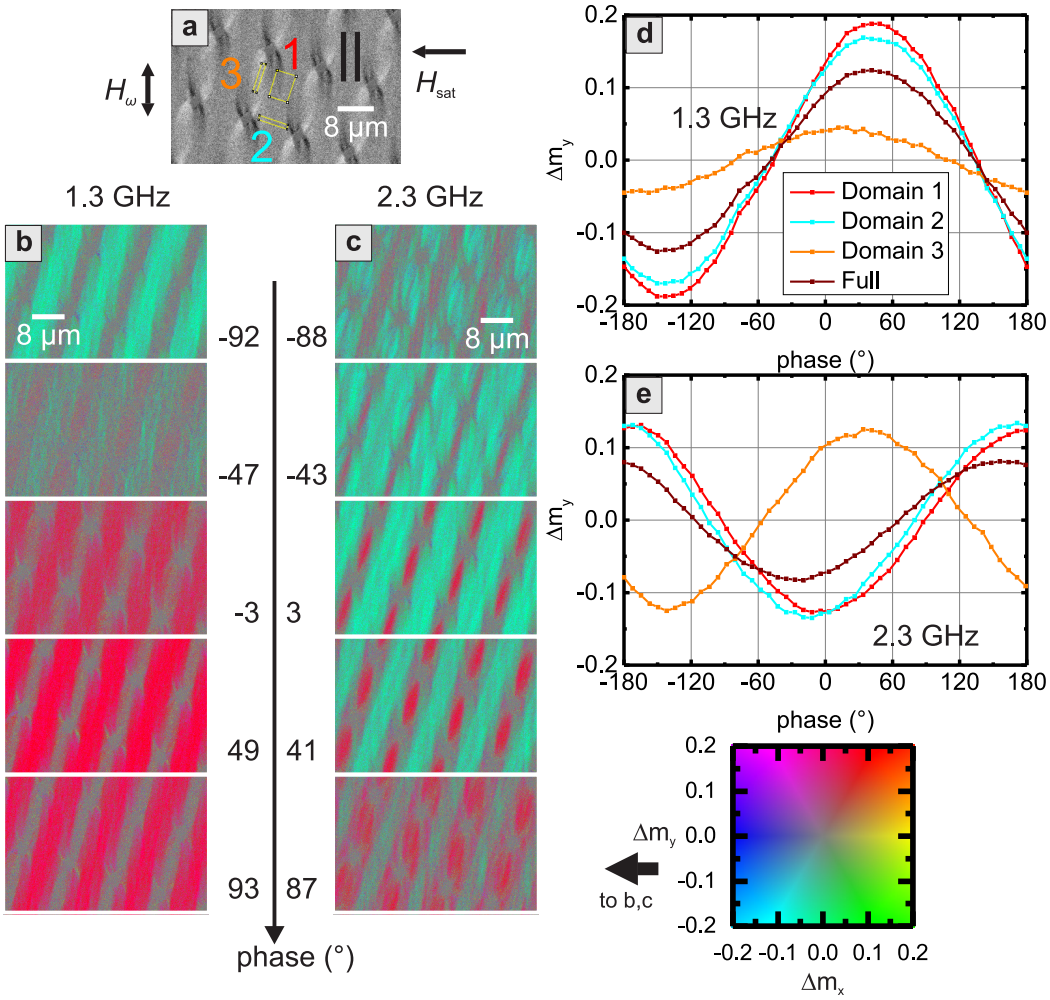

Figure 5.13: Time-resolved magneto-optical investigation of the remanent easy axis magnetization state for the diamond-shaped antidot patterned 50 nm $(Fe_{90}Co_{10})_{78}Si_{12}B_{10}$ film. a) static magnetization configuration of the remanent easy axis state. b) dynamic vector response of the magnetization at 1.3 GHz excitation frequency. c) dynamic vector response of the magnetization at 2.3 GHz excitation frequency. d) locally averaged domain response Δm_y at 1.3 GHz. e) locally averaged domain response Δm_y at 2.3 GHz.

the full frame at 2.3 GHz. Again, domain 1 and domain 2 exhibit a similar response of both, amplitude and phase. However, domain 3 shows a similar amplitude as domain 1 and 2, but also a drastic phase shift of almost half a period. Due to the phase shift of domain 3, the full sample response is lower than the individual domain response, since they partially cancel each other out. It is conclusive from this data, that domain 3 has a higher local resonance frequency than domain 1 and domain 2. Generally, at resonance the phase shifts from zero (following the forced oscillation in-phase) over $-90°$ (directly at resonance) to $-180°$ (lagging behind the excitation). At 1.3 GHz the amplitude of the oscillation in domain 3 is low and the phase is close to zero, therefore it is far below the resonance frequency. At 2.3 GHz domain 3 oscillates stronger with a strong phase shift compared to domain 1 and domain 2, thus domain 1 and domain 2 are oscillating above the resonance frequency and domain 3 oscillates still below the resonance frequency (compare amplitude and phase in Fig. 2.8). Considering the phase of domain 1 and domain 2 compared to domain 3 at 2.3 GHz, it is clear that domain 1 and domain 2 are already oscillating above the local resonance frequency. The resonance frequency of domain 3 is higher than 2.3 GHz, the local resonance frequency of domain 1 and domain 2 is between 1.3 GHz and 2.3 GHz. Because of the phase shifts due to the local resonances a part of the high frequency response above 1.3 GHz cancels out leading to PIMM spectra with an artificially lower maximum magnitude frequency (compare Fig. 5.11) than the local resonance frequencies. This is consistent with the resonance frequency of the full film, which is higher than the remanent easy axis state and lower than the remanent hard axis state (see Fig. 5.6).

Fig. 5.14 shows the time-resolved magneto-optical investigation of the remanent hard axis state. In Fig. 5.14a the static ground state is depicted, which is dynamically excited. This static domain image was recorded with a horizontal sensitivity. Again the sample is placed magnetic face down on the waveguide. Three domains are marked in the static configuration. The same areas as for Fig. 5.13 are analyzed: Domain 1 corresponds to the matrix aligned approximately along the uniaxial anisotropy, domain 2 to the interconnection between the antidots along the short lattice axis, where additional domains are formed for the remanent hard axis state. Domain 3 is the interconnection between the antidots along the long lattice axis, where no Néel spikes are overlapping for this magnetization configuration. In Fig. 5.14b the dynamic in-plane vector response of the remanent hard axis configuration is shown for an excitation frequency of 1.3 GHz

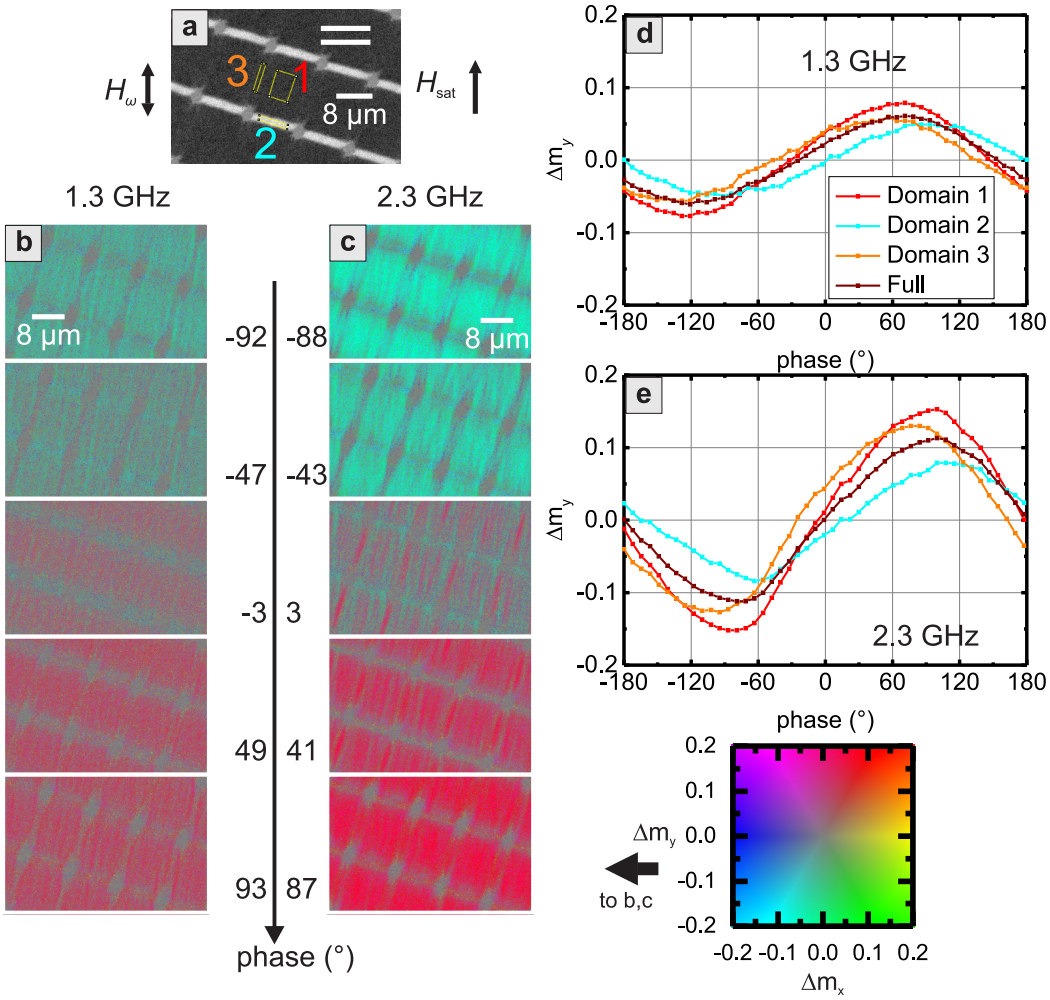

Figure 5.14: Time-resolved magneto-optical investigation of the remanent hard axis magnetization state for the diamond-shaped antidot patterned 50 nm $(Fe_{90}Co_{10})_{78}Si_{12}B_{10}$ film. a) static magnetization configuration of the remanent hard axis state. b) dynamic vector response of the magnetization at 1.3 GHz excitation frequency. c) dynamic vector response of the magnetization at 2.3 GHz excitation frequency. d) locally averaged domain response Δm_y at 1.3 GHz. e) locally averaged domain response Δm_y at 2.3 GHz.

and a utilized field amplitude of approximately $H_\omega = 300\ \mathrm{A/m}$ along the y-axis. It can be seen, that domain 1, domain 2 and domain 3 show a similar dynamic vector response - a precession around the easy axis of magnetization. A slight phase shift of domain 2 is visible. Domain 3 shows qualitatively the same dynamic behavior as domain 1. Small periodic modulations are visible in domain 1 and 2, possibly corresponding to the dynamic response of the cross-tie domain walls and the short fork-like Néel spikes seen in Fig. 5.10b. Another possibility would be the generation of spin waves or elastic waves by the inhomogeneous magnetization configuration. Such a behavior is discussed more deeply in Chapter 6 for a different structure. Fig. 5.14c displays the dynamic in-plane vector response of the remanent hard axis configuration for an excitation frequency of $2.3\ \mathrm{GHz}$ and a utilized field amplitude of approximately $H_\omega = 300\ \mathrm{A/m}$ along the y-axis. Domain 1 and domain 3 again show a similar dynamic response, an in-phase oscillation around the axis of uniaxial anisotropy with small spatial modulations. Domain 2 shows a slightly phase shifted response, most likely again due to a small deviation in resonance frequency compare to domain 1 and domain 3. However, due to the formation of the anti-parallel domain (compared to the matrix) and the orientation of the uniaxial anisotropy, the local effective fields seem not to be drastically different resulting in a similar local resonance frequency. In Fig. 5.14d the average Δm_y component is plotted as a function of the phase of the excitation field for the three individual domains and for the response of the full frame at $1.3\ \mathrm{GHz}$. Here, the response of domain 1, domain 2 and domain 3 is low, similar in phase and similar in amplitude. Domain 2 shows a slightly lower response and has a small phase shift to domain 1, domain 3 and the full sample response, which is dominated by the response of domain 1 and domain 3. Fig. 5.14e displays the average Δm_y component as a function of the phase of the excitation field for the three individual domains and for the response of the full frame at $2.3\ \mathrm{GHz}$. Here, domain 1, domain 2 and domain 3 exhibit a similar response of both, amplitude and phase. The qualitative magnetic response is similar at $1.3\ \mathrm{GHz}$ and $2.3\ \mathrm{GHz}$ for the remanent hard axis state, but the amplitude of the magnetic response is higher at $2.3\ \mathrm{GHz}$. Still the response of domain 2 is a bit out of phase and shows a slightly lower amplitude. Since the qualitative behavior between $1.3\ \mathrm{GHz}$ and $2.3\ \mathrm{GHz}$ did not change much, it is not as clear, which local resonance frequency is higher without looking quantitatively at the phase to the excitation. However, they seem to be close to each other. The maximum amplitude high frequency response of the remanent hard axis state is higher than the

maximum amplitude response for the remanent easy axis state. This could possibly be related to the occurence of dynamic magnetic inhomogeneities and modulations visible in Fig. 5.14b and c. Also, for higher effective fields and consequently for higher resonance frequencies, the angle of the cone of precession (see θ in Fig. 2.7) gets more narrow. The resulting phase of each domain and the full sample response is summarized in Tab. 5.1 for a quantitative understanding.

Phase shift(°)	Remanent easy axis (1.3 GHz)	Remanent easy axis (2.3 GHz)	Remanent hard axis (1.3 GHz)	Remanent hard axis (2.3 GHz)
ϕ_1	-43	-179	-58	-87
ϕ_2	-41	-168	-90	-109
ϕ_3	-16	-37	-46	-71
ϕ_f	-41	-155	-64	-92

Table 5.1: Phase between excitation and response of different domains and phase shift to full response for both remanent states at 1.3 GHz and 2.3 GHz.

Here, the phase differences to the excitation show, what was already discussed qualitatively. For remanent easy axis state at 1.3 GHz domain 1 and domain 2 and the phase of the full frame response have a similar phase and are below the resonance frequency. The phase of domain 3 is closer to the excitation phase with $-16°$ and thus more far away from resonance compared to domain 1 or domain 2. At 2.3 GHz the remanent easy axis configuration show the anticipated behavior: Domain 1 and domain 2 oscillate with a similar phase of $-179°$ and $-168°$, but most significantly is the very different phase of domain 3 with $-37°$. This proofs the anticipated local resonance mechanism. As a result the phase of the full frame is shifted to $-155°$. For the remanent hard axis state at 1.3 GHz similar phases compared to the excitation are observed for the three domains: domain 2 exhibits a phase of $-90°$, which could correspond to being at the local resonace frequency. In this case, it might correspond as well to being composed of different smaller magnetic microstructures showing only an integral response of $-90°$. The latter is supported by the relatively low amplitude compared to domain 1 and domain 3 (see Fig. 5.14). Domain 1 and domain 3 show a phase of $-58°$ and $-46°$ and are therefore still below the local resonance frequency. The phase of the full frame response is not so different from the phase of domain 1 with $-64°$. The remanent hard axis state

at 2.3 GHz shows again a local resonance: domain 2 exhibits a phase of $-109°$, thus it is driven close above its local resonance. Domain 1 and domain 3 are close below their local resonance with phase shifts of $-87°$ and $-71°$. The full frame response of remanent hard axis state is dominated by the local resonance of domain 1 and shows a phase of $-92°$.

The calibrated time-resolved wide-field MOKE imaging enables the detection of local resonances via a calibrated phase. By applying this technique it was possible to understand these local dynamics in more detail and explain features of the magneto-dynamic spectrum, such as the decreased maximum magnitude frequency of the remanent easy axis state compared to the full film.

5.5 Comparison of Inductive and Optical Measurements

To further understand the implications of the optical experiments and their meaning for the inductive behavior a comparison of the methods is desired. Therefore, an amplitude ratio r is defined as:

$$r = \frac{A_{\text{rem hard axis}}}{A_{\text{rem easy axis}}}, \tag{5.7}$$

where the amplitude values are given by the amplitude of the differential sine wave for CW-FMR and the amplitude of the magneto-optical response along the y-axis of the full frame shown in the dynamic magneto-optical measurements. In Tab. 5.2 the

Amplitude ratios	r (CW-FMR)	r (MOKE)
1.3 GHz	0.59	0.47
2.3 GHz	1.09	1.29
Stripline width	160 μm	160 μm
Excitation field	300 A/m	300 A/m

Table 5.2: Amplitude ratios for switching from hard axis remanent to easy axis remanent at 1.3 GHz and 2.3 GHz. Comparison of CW-FMR and MOKE.

amplitude ratios obtained by CW-FMR and MOKE are assembled. The ratios obtained

by both techniques are in agreement with each other. For the inductive technique the non-homogeneous excitation could be a source of deviation from the local behavior. A complete review of the differences between MOKE, CW-FMR and PIMM is beyond the scope of this work and has been covered for example in [Neudecker06].

5.6 Summary

The basics of the ferromagnetic resonance techniques PIMM and CW-FMR were introduced. Dynamic properties resulting from PIMM measurements of a full film have been discussed. A thin film patterned with diamond-shape antidots was investigated with static vector MOKE, PIMM, CW-FMR and time-resolved magneto-optical vector imaging. Bistable remanent domain states were found in static MOKE. The resulting inductive spectra were fundamentally different for the two remanent states, in particular a shift of the maximum magnitude frequency of the high frequency susceptibility was found. Highly reproducible switching between remanent states was achieved requiring only low magnetic switching fields. The dynamic optical investigation showed, that fundamentally different dynamics could be achieved by switching the domain structure. Localized resonances were found in the remanent easy axis domain state, while a spatially modulated magnetization response was found in the remanent hard axis state. A new type of functionalizing magnetic microwave materials was found relying on local effective fields and resonances. The observed shift in resonance frequency of $1\ \mathrm{GHz}$ was large and the maximum amplitude frequency of the remanent hard axis state was close to a application relevant frequency band around $2.4\ \mathrm{GHz}$.

6 Broadband Emission of Spin Waves and Elastic Waves by Domain Walls

Spin waves are a fundamental collective excitation of the spin system in a ferromagnetic material and a candidate to substitute today's electronics by low power consumption wave-computing [Chumak15, Kruglyak10, Lenk11]. Natural boundaries as edges and domain walls in a ferromagnetic material introduce local effective fields in the magnetic medium. By homogeneous excitation with a high frequency Oersted-field, these boundaries can be manipulated into regimes of spin-wave emission [Mushenok17, Lohman17, Whitehead17]. Symmetric Bloch domain walls and their spin wave eigenmodes have been studied since the early 1960's [Winter61]. Numerical and analytical models are among the predictions for uniaxial [Shimokhin91] and cubic materials [Alekseev99]. The use of Néel for guidance of spin waves modes and mode localization has been discussed in [Trützschler16, Wagner16]. Also, magnetic domain walls could be used as delimiter for spin waves [Pirro15]. In [Wintz16] it was shown that magnetic vortices could be used as tunable spin wave emitters. Furthermore it has been suggested by numerical studies to use magnetic domain walls as directional spin wave sources [Roy10, Wiele16]. Here, the excitation of various spin wave modes by homogeneously driven domain walls is investigated by direct observation and numerical simulation.

An excitation scheme of magnetostatic surface spin waves using magnetic domain walls is investigated by picosecond magneto-optical imaging and micromagnetic simulations. Homogeneously excited asymmetric Bloch walls are studied in a two dimensional periodic structure using micromagnetic simulations. Emission of magnetostatic surface spin waves and secondary low-wavelength, possibly dipolar-exchange spinwave, modes can be found. In the experiment similar magnetostatic surface spin waves can be found

at excitation frequencies exceeding 6 GHz. The short-wavelength spin waves are not accessible in the experiment, due to the limited optical resolution. Furthermore, the experiment shows an elastic wave emission in the excitation frequency range of 0.55 GHz to 2.5 GHz. These coincide with the phase velocity of an elastic shear wave. Also, the magnetization obtained by micromagnetic simulations is calculated to a magnetostrictive force density, which can be utilized as an input parameter for mechanical finite element method (FEM) simulations. Hereby, the mechanical simulation shows Rayleigh-waves excited at the domain walls. Therefore, the homogeneous excitation of ferromagnetic domain walls offers a magnetic scheme to excite elastic waves as an alternative to magneto-electric excitation of coherent elastic waves as surface acoustic waves (SAW), for which it was shown that they can induce ferromagnetic resonance [Weiler11] and interact with magnetic microstructures [Foerster17]. The measurements shown in this chapter were elaborated together with Cai Müller. The mechanical simulations were performed by Julius Schmalz under the supervision of Martina Gerken. The results of this chapter have been published in [Holländer18].

6.1 Excitation of Magnetic Waves

In Fig. 6.1 the excitation geometry and an exemplary domain configuration of the sample are shown. The CPW is utilized for generation of a microwave Oersted field and allows for a homogeneous field distribution directly on top of the center conductor. The magnetic specimen is an amorphous $Co_{40}Fe_{40}B_{20}$ stripe element with dimensions of $40\ \mu\text{m} \times 1\ \text{cm} \times 120\ \text{nm}$ and the same sample as shown in Chapter 4. Fig. 6.1 depicts a schematic of the CPW, on which the ferromagnetic stripe element is positioned with the long stripe axis perpendicular to the center conductor of the CPW. The axis of uniaxial anisotropy is parallel to the stripline. Therefore, the microwave excitation is perpendicular to the long stripe axis enabling excitation of the dominant domain precession. Using external field history, different domain states can be created and excited. An exemplary wide domain state (WDS) of the ferromagnetic stripe element is depicted in Fig. 6.1. Also, the frequency of the microwave excitation can be tuned between 50 MHz and 20 GHz. By varying the frequency different modes of oscillation can be observed using the stroboscopic imaging scheme described in Chapter 4.

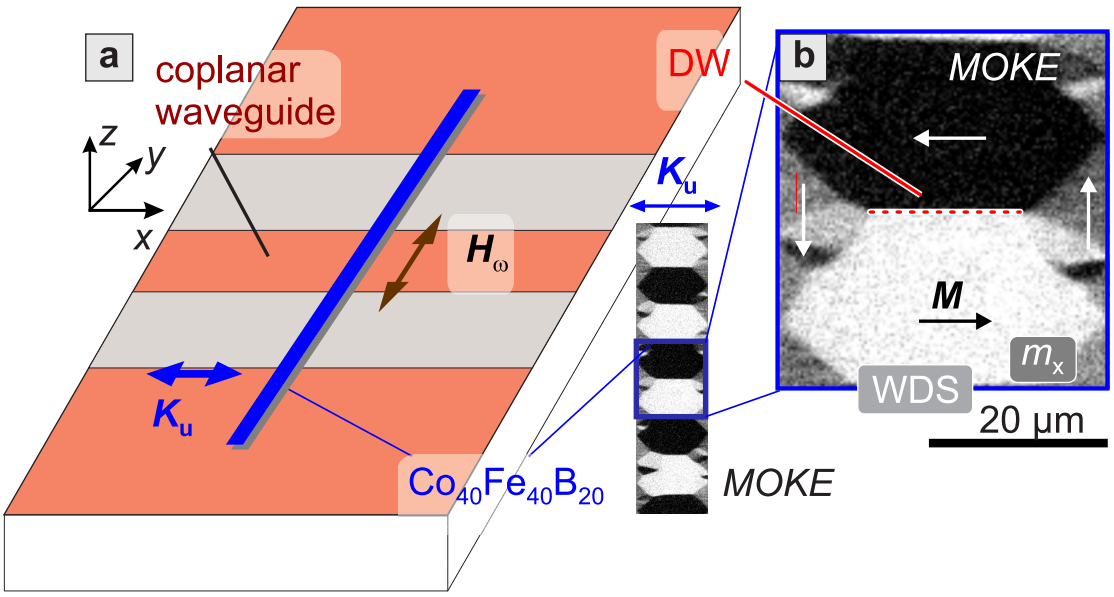

Figure 6.1: Excitation scheme for magnetic oscillation in a ferromagnetic stripe element: a) Geometry of excitation. b) exemplary domain configuration. This figure is a derivative of the figure published in [Holländer18] under the creative commons license.

6.2 Direct Observation of Magnetostatic Spin Waves Emitted by Domain Walls

Fig. 6.2 shows the direct experimental observation of the emission of magnetostatic surface spin waves (MSSW) by domain walls. A short introduction to the magnetostatic spin wave modes can be found in Section 2.4.2. In Fig. 6.2a a wide domain state (WDS) was created by external field history. Here, the sample was first saturated along the axis of uniaxial anisotropy. Then, the field was reduced to zero resulting in a remanent state with increased domain width compared to the equilibrium state. The WDS was then excited by a microwave field with a frequency of $9\ \mathrm{GHz}$ and a field amplitude of $H_\omega \approx 100\ \mathrm{A/m}$ (calculated on the surface of the waveguide). The time evolution was recorded with simple oblique incidence resulting in a superposition of longitudinal and polar magneto-optical contrast. Standing wavefronts can be observed parallel to the $180°$ asymmetric Bloch domain walls in the central domains. A line for eye guidance was drawn on the node of the wavefronts. Also, the out-of-plane precession is visible by the

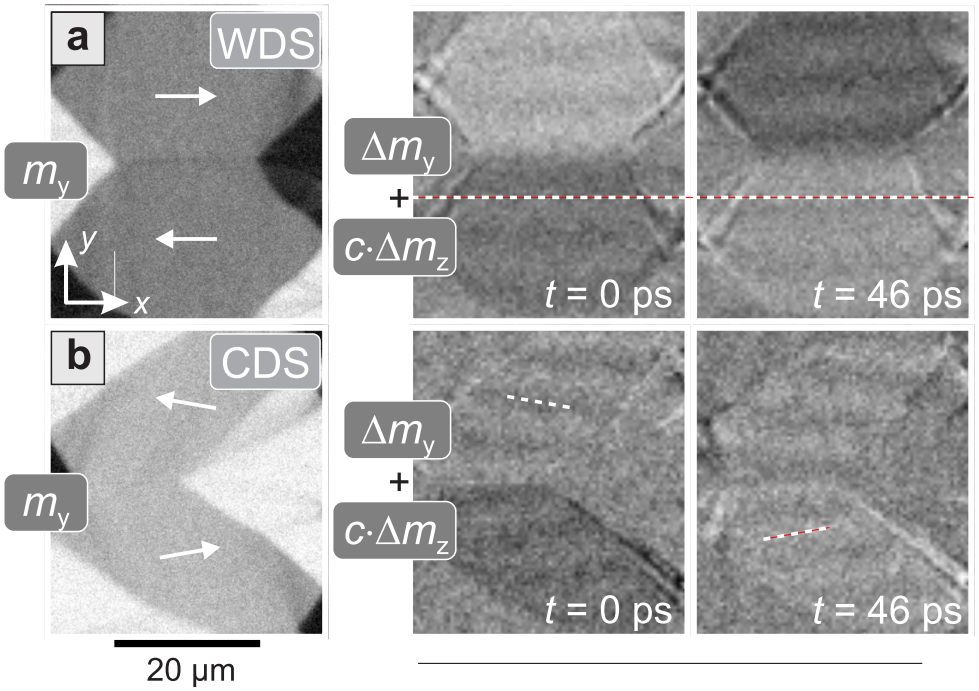

Figure 6.2: Direct observation of magnetostatic surface spin waves (MSSW) in domain structures: a) a static wide domain state (WDS) is excited by a homogeneous Oersted-field along the y-axis at a frequency of 9 GHz. The dynamic images contain a superposition of out-of-plane and longitudinal in-plane contrast. Standing wavefronts are visible in the center domains parallel to the magnetization and 180° domain wall. b) a static canted domain state (CDS) is excited by a homogeneous Oersted-field along the y-axis at a frequency of 9 GHz. The dynamic images contain a superposition of out-of-plane and longitudinal in-plane contrast. Standing wavefronts are visible in the center domains parallel to the magnetization, but not parallel to the 160° domain wall. This figure is a derivative of the figure published in [Holländer18] under the creative commons license.

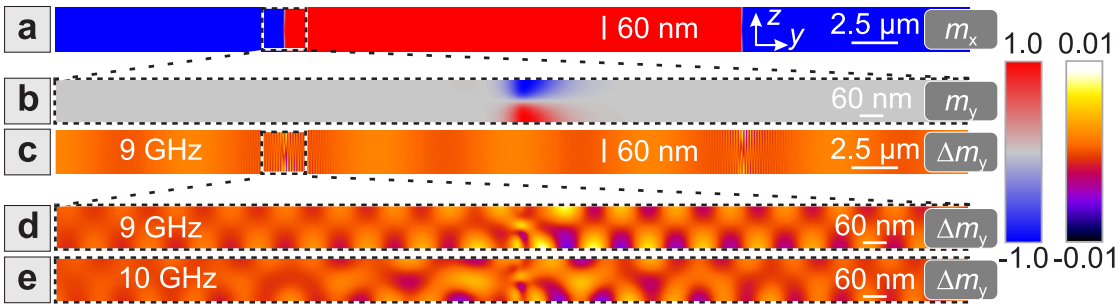

Figure 6.3: Micromagnetic simulation of MSSW and additional low-wavelength spin waves emitted by an asymmetric Bloch wall: a) cross-section of static domain state utilized for the dynamic simulations. Magnetization along x-direction is depicted. Two 180° domain walls separated by 25 μm wide domains are calculated for a 120 nm thin film with periodic boundary conditions along x- and y-axis. b) static vicinity of the left domain wall. Magnetization along y-direction is depicted. c) dynamic cross-section of domain state excited by a high frequency Oersted-field at an excitation frequency of 9 GHz. Differential magnetization response along y-direction is depicted. d-e) dynamic cross-section of domain state in the vicinity of the left domain wall excited by a high frequency Oersted-field at an excitation frequency of d) 9 GHz and e) 10 GHz. Differential magnetization response along y-direction is depicted. This figure is a derivative of the figure published in [Holländer18] under the creative commons license.

phase shift of the two shown domains. In comparison Fig. 6.2b shows a canted domain state (CDS), which was created by remanent domain state and an additional bias field along the long axis of the stripe $H_y = 600$ A/m. The bias field results in a reorientation of the central domains by approximately 10°. Therefore, the former 180° asymmetric Bloch domain wall transforms into a 160° asymmetric Néel wall. Corresponding simulations can be found in Chapter 2. More details on domain wall transformations containing phase diagrams can be found in [Hubert08]. Then, the CDS is excited using the same excitation as in Fig. 6.2a and the corresponding time evolution is recorded with simple oblique incidence containing polar and longitudinal contrast. The time evolution exhibits standing wavefronts, which are parallel to the orientation of the magnetization, not to the orientation of the domain wall.

In order to simulate the emission of MSSW by domain walls, a two dimensional pattern of two repeating $25\ \mu m$ wide antiparallel domains is chosen for micromagnetic simulations. The static parameters are identical with the parameter set used for the calculation of the asymmetric Bloch wall in Fig. 2.4a,b. Fig. 6.3a shows the m_x-component of the static domain configuration. The cross-section through the domain walls is depicted utilizing periodic boundary conditions along x- and y-direction. In Fig. 6.3b the close vicinity of the domain wall is shown represented as static m_y-component. The domain walls have an asymmetric Bloch wall configuration. Fig. 6.3c shows the dynamic magnetization response at $9\ \mathrm{GHz}$ excitation frequency in dynamic equilibrium. The utilized field amplitude was $H_\omega = 150\ \mathrm{A/m}$. The Gilbert damping was $\alpha = 0.008$ in accordance with PIMM measurements performed on the amorphous $Co_{40}Fe_{40}B_{20}$-stripe sample. In order to gain only the dynamic magnetization response Δm_y, each dynamically simulated phase ϕ was subtracted by a background configuration at phase $\phi - \pi$. It is evident from Fig. 6.3c that magnetostatic surface spin waves are excited in the domain with the same periodicity as in Fig. 6.2a. Fig. 6.3d,e show the close vicinity of the left dynamically simulated domain wall. A short wavelength spin wave emission by the domain wall can be seen. In Fig. 6.3d the excitation of these spin waves is shown at $9\ \mathrm{GHz}$ exhibiting one mode of emission, while at $10\ \mathrm{GHz}$ (Fig. 6.3e) at least two different wavelengths are present. These low-wavelength spin waves possibly correspond to dipolar-exchange spin waves. However, they did not have an experimental counterpart, since the wavelengths were too small for an optical investigation. Fig. 6.4 shows the full time evolution of the simulated MSSW at an excitation frequency of $9\ \mathrm{GHz}$. Differential magnetization response along the y-direction Δm_y is depicted. $t = 0\ \mathrm{ps}$ is chosen after 45 periods of oscillation. It can be seen, that the wavefronts are standing in dynamic equilibrium.

To show that the spin waves are actually emitted at the domain walls, the origin of the waves can be observed in the transient effect. Therefore, the transient effect of the differential magnetization response Δm_y is shown in Fig. 6.5. Plotted is the top layer of magnetization along the z-direction in the central domain of Fig. 6.3a (red) as a function of time and y-position. The two domain walls (DW1 and DW2) are located at $y = -12.5\ \mu\mathrm{m}$ and $y = 12.5\ \mu\mathrm{m}$. The sinusoidal microwave excitation was started at $t = 0\ \mathrm{ns}$ ($t = 0\ \mathrm{ns}$ is not to compare for Fig. 6.4 and Fig. 6.5). It is directly evident that at $t = 0\ \mathrm{ns}$ no waves are present in the domain, but in the time evolution the waves

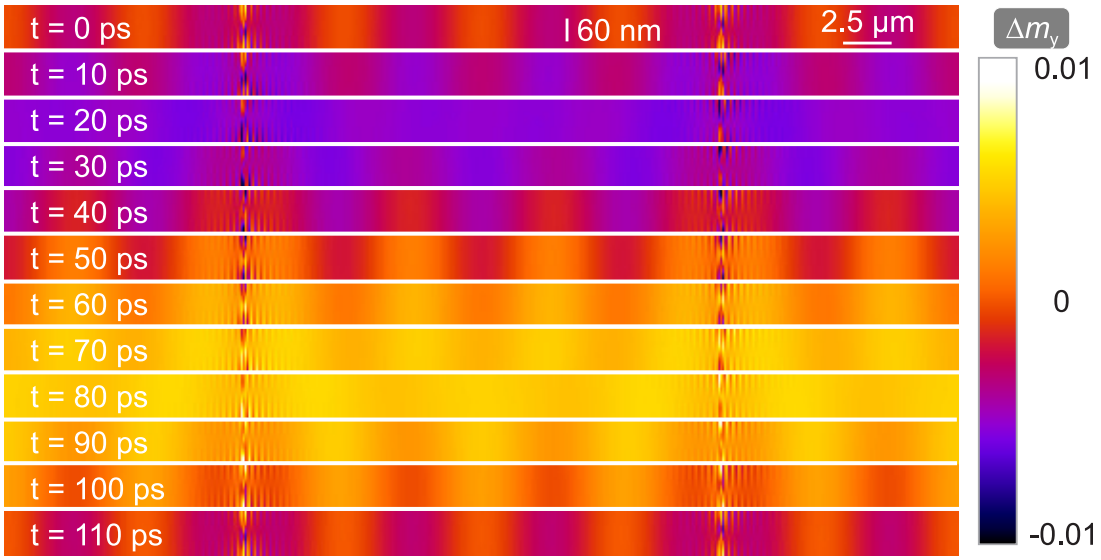

Figure 6.4: Time evolution of dynamic micromagnetic simulation of MSSW at an excitation frequency of 9 GHz. Differential magnetization response along y-direction is depicted. $t = 0$ marks the beginning of a period in the dynamic equilibrium. This figure is a derivative of the figure published in [Holländer18] under the creative commons license.

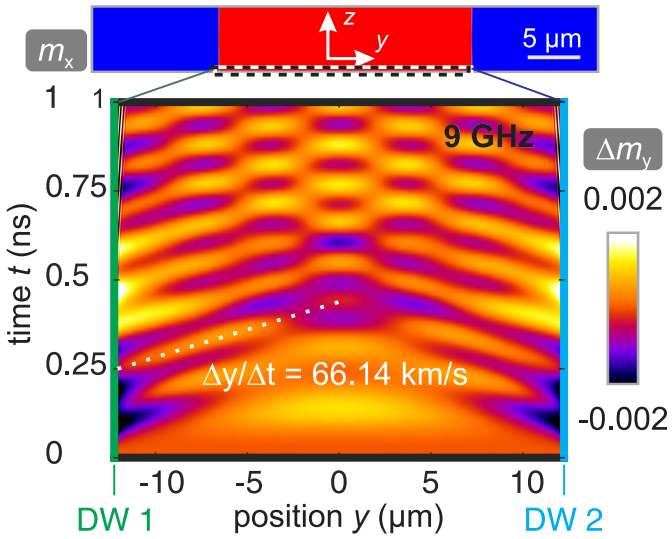

Figure 6.5: Transient effect of Fig. 6.3 c). Depicted is the dynamic differential magnetization Δm_y in the top layer along the z-axis and in the center domain enclosed by the two domain walls at $y = -12.5\ \mu\mathrm{m}$ and $y = 12.5\ \mu\mathrm{m}$ as a function of y-coordinate and time. This figure is a derivative of the figure published in [Holländer18] under the creative commons license.

start to emerge from the domain walls. As soon as the wavefronts meet in the center of the domain a superposition pattern is formed. By following one phase front, the phase velocity of the wave can be obtained $\Delta y/\Delta t = 66.14\ \mathrm{km/s}$. As for the underlying mechanism of spin wave generation at the domain walls: The local effective fields in the domain wall (compare Fig. 2.4b) lead to a gradient in resonance frequency at the domain wall, enabling spin wave emission [Schlömann64].

6.3 Direct Observation of Elastic Waves

By measuring the dynamic magnetization response not only coherent spin waves can be imaged, also coherent elastic waves can be seen in the magnetization contrast, as long as the magnetization locally follows the magnetostrictive stimulus. Fig. 6.6 shows exemplary data on the emission of elastic waves by $180°$ asymmetric Bloch domain walls. Here, a WDS was excited by a microwave field with frequency $1.9\ \mathrm{GHz}$ and amplitude $H_\omega = 300\ \mathrm{A/m}$ directly on top of the waveguide. The corresponding data set was already shown in Fig. 4.8 and the microscopic details of the magnetization response were discussed in Chapter 4. Here, the focus is on the emission of waves from the domain walls. In the Δm_x-component no wavefronts are visible. In Δm_y and Δm_z clear wavefronts parallel to the $180°$ are evident. Since the subjects of interest are elastic waves, we check whether the generated signal stems from direct magnetization response, or if it is an optical artifact due to the photo-elastic effect. The photo-elastic effect is a birefringence effect and the corresponding reflection coefficients are symmetric for positive and negative angles of incidence [Silverman90]. Therefore, by subtracting two diametric aligned sensitivities from each other, the photo-elastic contrast cancels out. Due to this symmetry the pure in-plane dynamic images do not contain photo-elastic contrast. Knowing this, it is evident, that the elastic waves contribute to the magnetization dynamics in Δm_y. Since the excitation frequency is close to the frequency of domain resonance (describing a precession around the easy axis of magnetization), it is very likely that the elastic waves also excite the out-of-plane magnetization component, but the same characteristics would be found by a mechanical wave exciting two magnetization components in linear response.

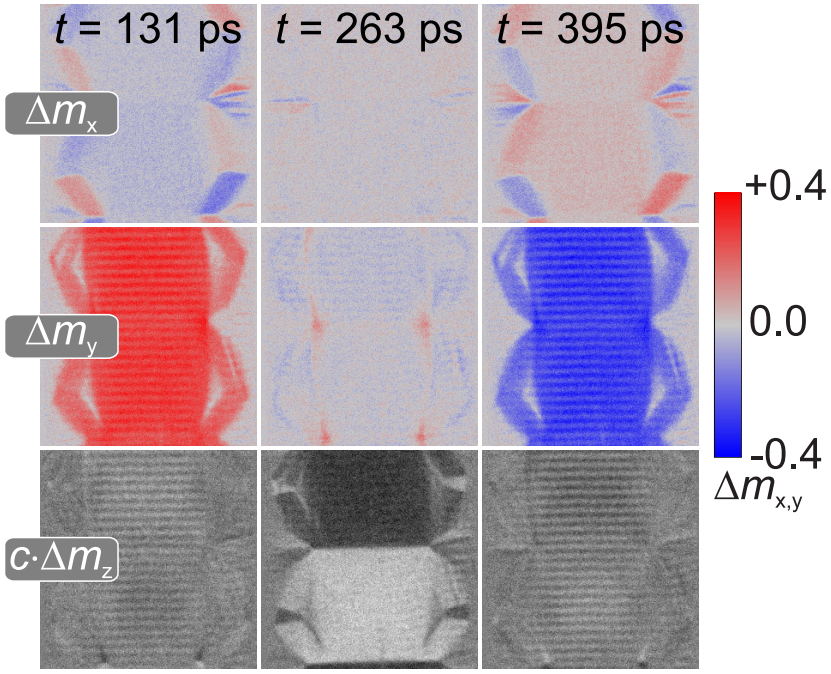

Figure 6.6: Component-selective differential magnetization response of stripe element in a WDS at and excitation frequency of 1.9 GHz corresponding to the frequency of the center domain resonance. All three components of differential magnetization response are depicted for three different points in time. This figure is a derivative of the figure published in [Holländer18] under the creative commons license.

To experimentally proof the generation of elastic waves by magnetic domain walls, the emission is measured with different magnetization configurations. Fig. 6.7 illustrates different static magnetization states and their corresponding time evolution. In Fig. 6.7a the static m_x-component of a CDS is shown. The field history is analogue to the static magnetization configuration shown in Fig. 6.2b. Therefore, the magnetization is tilted by approximately $10°$ and the wall corresponds to a $160°$ asymmetric Néel wall, again. Here, a microwave field with a frequency of 1.9 GHz and an amplitude of $H_\omega = 150$ A/m directly on top of the waveguide was used to excite the CDS. In the time evolution dynamic polar contrast is shown. The domain precession of the central domains is visible by the phase shift of the upper and lower domain. Also, magneto-dynamic features appear on the nodes, where domain walls meet originating in the magnetically charged domain state. Furthermore, wavefronts are visible in the central domains. These wavefronts are

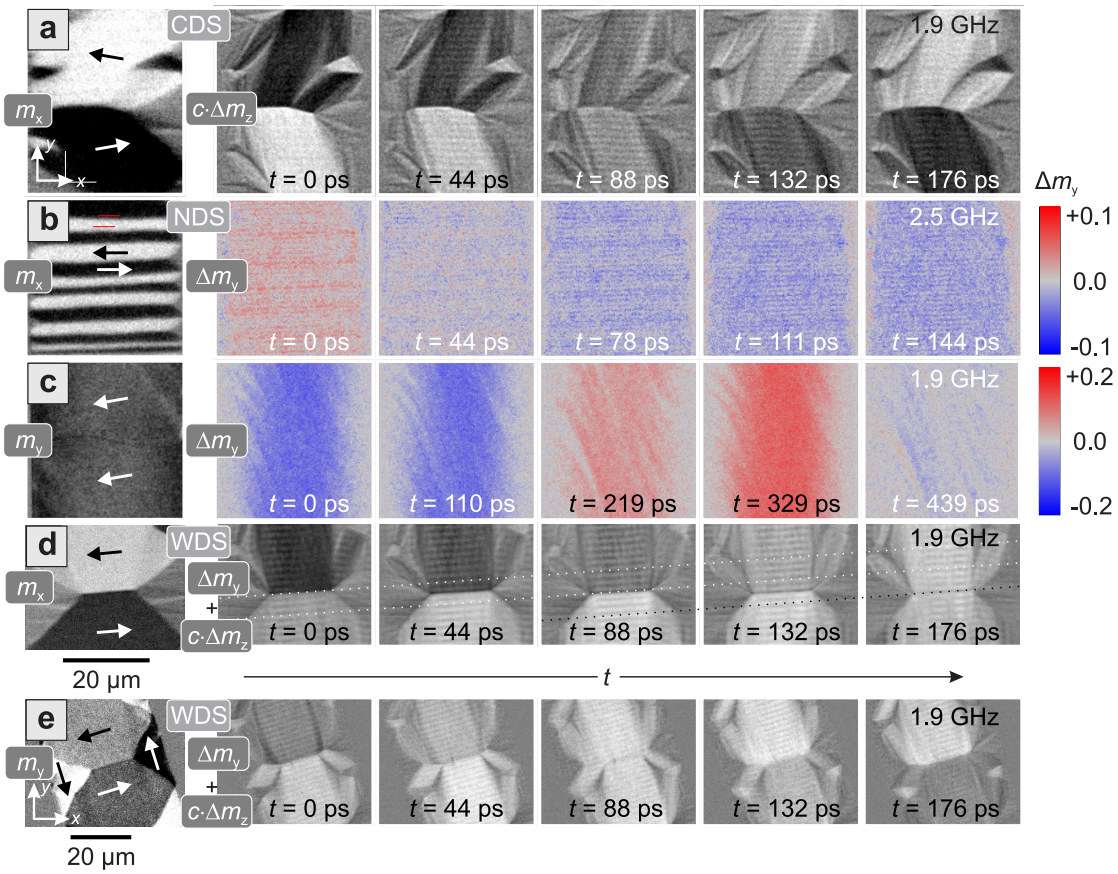

Figure 6.7: Static image and time-evolution of dynamic magnetization response at different domain configurations: a) static image and polar time evolution of a canted domain state (CDS) at an excitation frequency of 1.9 GHz. b) static image and pure in-plane time evolution of a narrow domain state (NDS) at an excitation frequency of 2.5 GHz corresponding to the center domain resonance. c) static image and pure in-plane time evolution of a domain state without high-angle domain walls at an excitation frequency of 1.9 GHz. d) control experiment with a tilted domain wall at 1.9 GHz: Anisotropy and 180° domain wall are tilted by 4.5°, but the wavefronts remain parallel to the domain wall. The dynamic images show longitudinal magneto-optic contrast superposed with polar magneto-optic contrast. Lines for eye guidance are drawn. e) control experiment with a tilted magnetic stripe element at 1.9 GHz: Anisotropy and 180° domain wall are tilted by 4.5°, but the wavefronts remain parallel to the domain wall. The dynamic image shows polar magneto-optic contrast. Lines for eye guidance are drawn. This figure is a derivative of the figure published in [Holländer18] under the creative commons license.

parallel to the orientation of the high angle magnetic domain wall and not parallel to the magnetization (compare Fig. 6.2b). Also, the wavefronts do not show a significant change by the wall transition from asymmetric Bloch wall to asymmetric Néel wall leading to the conclusion, that both domain wall types can emit elastic waves.

Fig. 6.7b exhibits a static narrow domain state (NDS) and the corresponding time evolution at its domain resonance at an excitation frequency of $2.5\ \mathrm{GHz}$ and excitation field of $H_\omega = 150\ \mathrm{A/m}$ directly on top of the waveguide. The NDS was created by applying an external field sufficiently high for saturation perpendicular to the axis of uniaxial anisotropy. This field history leads to a decreased domain width of the central domains. Multiple central domains are present with different widths. The time evolution is shown as pure dynamic in-plane contrast Δm_y. The in-phase domain precession of the in-plane magnetization is observable. Wavefronts in the central domains are apparent from the time evolution. It can be seen, that the periodicity of the waves changed towards lower wavelengths. Furthermore, the wavefronts keep the same periodicity in domains of different widths. Therefore, generation of these waves is not bound to the domain magnetization.

In Fig. 6.7c a magnetization state close to saturation is shown as m_y-component. Here, a bias field of $3\ \mathrm{kA/m}$ was applied along the axis of uniaxial anisotropy. No high angle domain walls are present in this magnetic state. The time evolution shows differential dynamic in-plane contrast Δm_y. No elastic waves are present in the time evolution. Therefore, the generation of elastic waves is bound to the existence of high angle domain walls.

In order to verify the hypothesis, that elastic waves are generated by excitation of the magnetic domain walls, additional experiments were performed. Fig. 6.7d shows the resulting magnetization configuration, where a WDS with tilted anisotropy was investigated. Due to the tilted anisotropy, magnetization and $180°$ domain walls are also tilted by $4.5°$. The time evolution shows a superposition of longitudinal and polar contrast measured with oblique incidence. The magnetic state was excited at $1.9\ \mathrm{GHz}$ with an amplitude of $300\ \mathrm{A/m}$ directly on top o the waveguide. Again, a phase shift between the two central domains is visible due to the superposed polar magnetic contrast. Furthermore, wavefronts are visible in the central domains. The wavefronts are parallel

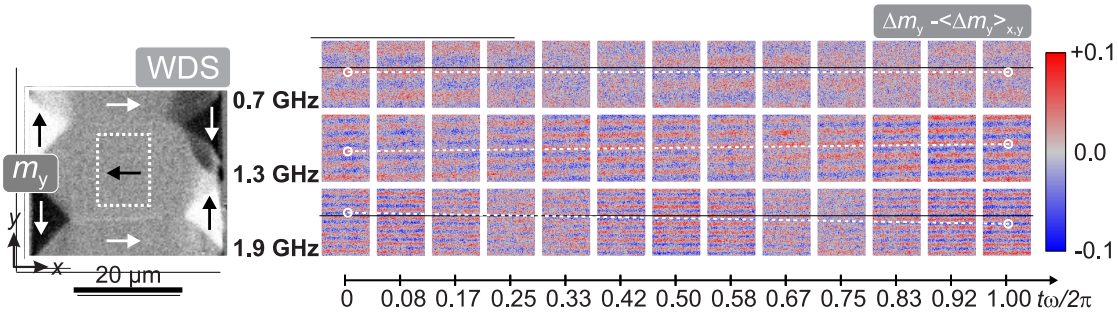

Figure 6.8: Static Image of a WDS and pure in-plane time-evolution at three selected frequencies: 0.7 GHz, 1.3 GHz and 1.9 GHz. This figure is a derivative of the figure published in [Holländer18] under the creative commons license.

to the orientation of domain wall and magnetization. Lines for eye guidance are drawn on the domain walls and the wavefronts. By combining Fig. 6.7a and d, it is evident, that the wavefronts follow the orientation of the magnetic domain wall and not the orientation of the magnetic track.

Also, the direct excitation of the microwave field should be excluded as source for the elastic wave excitation. Therefore, the magnetic stripe element was tilted with reference to the magnetic microwave excitation. This control experiment is depicted in Fig. 6.7 e). Here, the long stripe axis is tilted by approximately 17° with reference to the axis of microwave excitation. A static WDS is utilized in order to monitor the wave response with tilted excitation. The time evolution shows superposed longitudinal and polar dynamic contrast. The precession of the domains is eminent in the time evolution. The emerging wavefronts are still parallel to the 180° domain walls. This exhibits, that the generated elastic waves are bound to the existence and orientation of the high angle magnetic domain walls.

To find the dispersion of the elastic mode of oscillation, an experiment with an unbroken magnetization configuration was performed. Fig. 6.8 shows the static WDS as the m_y-component and the time evolution at three selected excitation frequencies in one identical domain as indicated by the rectangle in the static configuration. The time evolution shows pure magnetic in-plane contrast $\Delta m_y - \langle \Delta m_y \rangle_{x,y}$, where the uniform precession of the domain was removed by subtracting the spatial average $\langle \Delta m_y \rangle_{x,y}$ over each time frame. The excitation field was $H_\omega = 300\ \mathrm{A/m}$ directly on top of the waveguide. Lines for eye guidance were drawn following a maximum of the wave pattern. At 0.7 GHz the

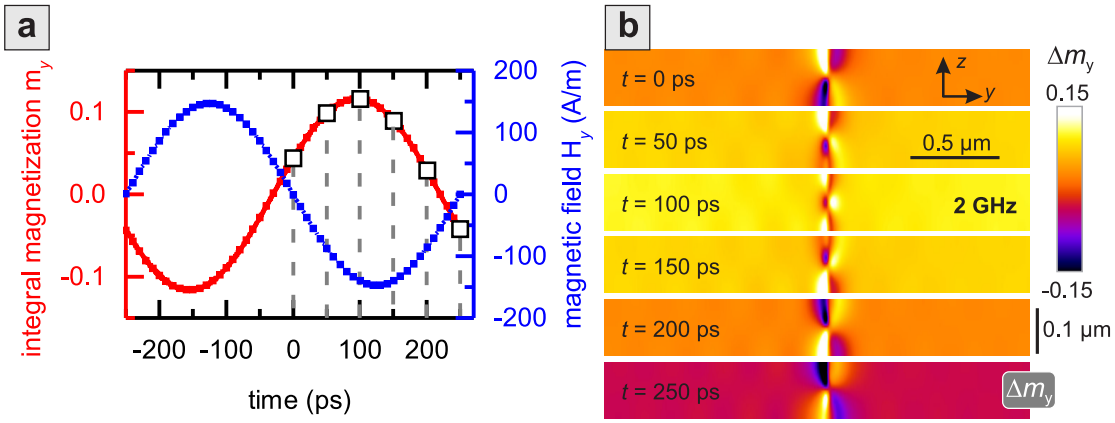

Figure 6.9: Time evolution of dynamic micromagnetic simulation of domain wall excitation in the vicinity of the domain wall at an excitation frequency of 2 GHz. a) integral magnetization component along the y-axis in dynamic equilibrium as a function of time. b) differential magnetization response in dynamic equilib along y-direction for selected points in time. This figure is a derivative of the figure published in [Holländer18] under the creative commons license.

line remains horizontal on the maximum corresponding to a standing wave. At 1.3 GHz the line has a positive slope, indicating propagation upwards. At 1.9 GHz excitation frequency the line has a negative slope indicating propagation downwards. Therefore, standing as well as propagating characteristics can be observed for the elastic waves. This behavior can be related to the following reason: The elastic waves travel farther than one domain width forming a superposition from more than two emitters. The propagating and standing characteristics then might be related to defect states far away from the measured domain.

In order to support that the origin of the elastic magnetization waves is of magneto-elastic nature, a micromagnetic simulation of the magnetization dynamics at 2 GHz was performed in the same geometry as Fig. 6.3, differing only by the excitation frequency ($H_\omega = 150$ A/m). The resulting time evolution is depicted in Fig. 6.9. The integral magnetization after relaxing the oscillating magnetization into dynamic equilibrium is shown in Fig. 6.9a. Also, the excitation field is plotted as a function of time. Magnetization and excitation field depict a significant phase shift of almost $-\pi$. This can be understood since the resonance frequency of the simulated periodic two dimensional pattern was at

1.5 GHz and therefore the here utilized excitation frequency is higher than the resonance frequency. The close vicinity of the magnetization response along the y-direction Δm_y is displayed for selected points in time in Fig. 6.9b and exhibits the excited domain wall. The dynamic equilibrium oscillation is exhibited. An in-phase precession of the two antiparallel domains left and right of the domain wall can be observed. A high differential response of the domain wall on the external stimulus can be seen. Compared with Fig. 6.3d,e the domain response and the domain wall response are much higher. No matching wavefronts can be seen in this calculation, since the micromagnetic model does not include magneto-elastic effects. As for the underlying mechanism, it is anticipated that the high magnetization response in the excited magnetic domain wall leads to an alternating elastic tensioning in the domain wall exciting the elastic waves. A parallel alignment of multiple domain walls then leads to a superposition of the propagating elastic waves.

In as simplified picture, the measured wavelengths coincide with the elastic shear wave dispersion, given by the sound velocity

$$c = \sqrt{\frac{G_{\mathrm{CoFeB}}}{\rho_{\mathrm{CoFeB}}}}, \tag{6.1}$$

where $G_{\mathrm{CoFeB}} = 70\ \mathrm{GPa}$ [Graczyk17] is the shear modulus and $\rho_{\mathrm{CoFeB}} = 7050\ \mathrm{kg/m^3}$ [Graczyk17] is the density of $\mathrm{Co_{40}Fe_{40}B_{20}}$. Using these literature values a velocity of $c = 3151\ \mathrm{m/s}$ can be obtained for the elastic shear wave, coinciding with the measured wave profiles without fitting of the dispersion. However, this reflects only the free shear wave velocity without boundary conditions and any distinct physical origin.

By multiplying the experimentally obtained wavelength and frequency, phase velocities in the expected regime of elastic shear waves are found. Thus, either an elastic shear wave or a combination of longitudinal and shear wave are expected. Therefore, a numerical approach considering also the substrate will be followed, now. To gain an understanding of the mechanics of the observed elastic waves, the micromagnetically calculated magnetization can be transformed into a locally acting strain (see Eq. 2.15)

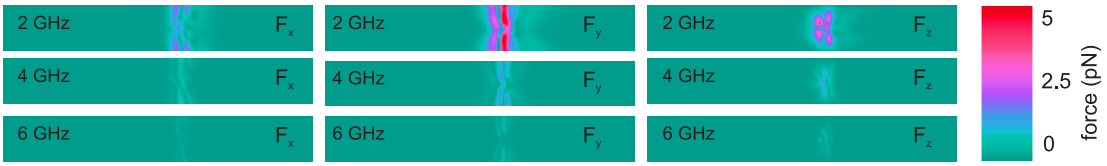

Figure 6.10: Magnitude of the local magnetostrictive force at an excitation frequency of 2 GHz. The force is shown directly on excitation frequency and on second and third harmonic.

and consequently into a local force density $\mathbf{f}$ via

$$\mathbf{f} = \nabla \cdot \underline{c} \cdot \underline{\epsilon^0}, \tag{6.2}$$

where $\underline{c}$ is the elastic stiffness tensor and $\underline{\epsilon^0}$ the magnetostriction tensor. After calculating the local force density in the vicinity of one domain wall from the data shown in Fig. 6.9, the FFT of the local force can be applied in order to transfer the force density from time to frequency domain. The magnitude of the force is shown in Fig. 6.10. The local force $\mathbf{F} = V_\mathrm{e}\mathbf{f}$ is depicted, where V_e is the volume of each cell element. It is shown on the excitation frequency (2 GHz) and second and third harmonic. The magnetostrictive force in the domains is vanishing compared to the domains. Also, the force is significantly higher on the excitation frequency than on the higher harmonics. Therefore, the force only directly on the excitation frequency can be selected neglecting higher harmonics. This complex force on the excitation frequency can then be used as an input parameter to a mechanical FEM simulation. COMSOL Multiphysics® is employed for this purpose. In the mechanical model, a 116 nm thick layer of amorphous $\mathrm{Co_{40}Fe_{40}B_{20}}$ with a length of 50 μm is considered on an infinitely thick glass substrate. Also, the boundaries along positive and negative y-axis are considered infinite in order to prohibit a reflection on the surface. The local force due to the excited domain wall was applied as boundary load in the middle of the magnetostrictive material in a small window of size $808 \times 116\ \mathrm{nm}^2$ around the domain wall. The thickness of the magnetostrictive layer was slightly reduced from 120 nm to 116 nm due to the evaluation of the numerical gradient. Also, the force along the x-axis is neglected due to the symmetry of the problem.

The results of the mechanical FEM simulations are depicted in Fig. 6.11. The two dimensional simulation allows for the extraction of the two longitudinal stress components

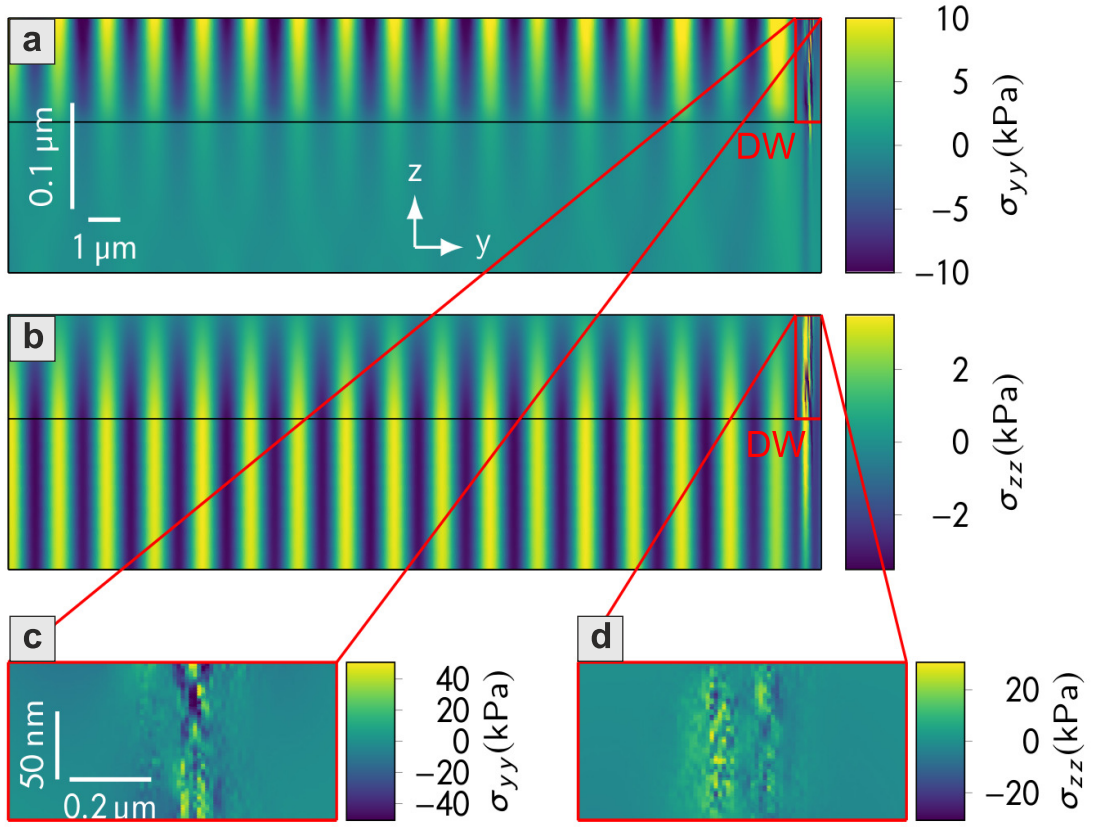

Figure 6.11: Elastic response on a oscillating domain wall (DW) at 2 GHz excitation frequency. a) longitudinal stress component along the y-axis. The domain wall is located in the top right box. b) longitudinal stress component along the z-axis. The domain wall is located in the top right box. c) longitudinal stress component along the y-axis. The close vicinity of the domain wall is magnified from a). d) longitudinal stress component along the z-axis. The close vicinity of the domain wall is magnified from b). The black line in a) and b) indicate the boundary between the magnetic material (top) and the substrate (bottom). The Young's modulus of $Co_{40}Fe_{40}B_{20}$ was $E_{\mathrm{CoFeB}} = 182$ GPa, the Poisson ratio $\nu_{\mathrm{CoFeB}} = 0.3$, the density $\rho_{\mathrm{CoFeB}} = 7050\ \mathrm{kg/m^3}$. The mechanical parameters of the substrate were: Young's modulus $E_{\mathrm{glass}} = 82$ GPa, the Poisson ratio $\nu_{\mathrm{glass}} = 0.206$, the density $\rho_{\mathrm{glass}} = 2510\ \mathrm{kg/m^3}$. This figure is a derivative of the figure published in [Holländer18] under the creative commons license.

σ_{yy} and σ_{zz}. Fig. 6.11a exhibits the longitudinal stress component σ_{yy} as a function of y- and z-coordinate. The domain wall is located in the top right corner. Clear wavefronts traveling away from the domain wall are visible. The black line indicates the boundary between the magnetic material and the glass. Fig. 6.11b exhibits the longitudinal stress component σ_{zz} as a function of y- and z-coordinate. In this case the waves are more pronounced in the substrate and decay towards the surface of the magnetic material, because the material can deform freely at the surface. The simulated waveform is a Rayleigh wave. In Fig. 6.11c a magnification of the stress along the y-axis σ_{yy} in close vicinity of the domain wall is shown. Fig. 6.11d shows a magnification of the stress along the z-axis σ_{zz} in close vicinity of the domain wall. It is evident that the simulated elastic waves are excited in the domain wall region. It is consistent, that the experimental measurement exhibit the wave in the Δm_y and Δm_z component and the simulated mechanical waves show stress along y- and z-axis. This exemplary data proofs the emission of elastic waves by the domain wall. Further proof is given by the analysis of multiple frequencies, which is subject to the following section.

6.4 Dispersion Analysis

Fig. 6.12 shows the dispersion map of different excited modes in the $\mathrm{Co_{40}Fe_{40}B_{20}}$ stripes. FFT and sine fit along the spatial dimensions yields the corresponding wavelengths $k/2\pi = 1/\lambda$. The FFT along the time axis obtained an oscillation on the excitation frequency, as expected for a forced oscillation in linear response. The experimental investigation of the MSSW shows the possibility to tune the emission wavelength by means of the excitation frequency. The simulated MSSW wavelengths are in excellent agreement with the measured MSSW. The first simulated low-wavelength mode was coherently emitted by the domain walls for excitation frequencies higher or equal 5 GHz. The second low wavelength mode was excited at frequencies higher or equal 10 GHz. At excitation frequencies lower than 5 GHz the low wavelength modes were excited in the simulation at higher harmonics of the excitation frequency. The measured elastic waves could be excited in a lower frequency regime between 0.55 GHz and 2.5 GHz. The measured wavelengths for WDS, NDS and CDS coincide within the limits of measurement inaccuracy. These elastic waves coincide almost perfectly with the simple elastic shear wave velocity. The simulated Rayleigh waves show a matching dispersion

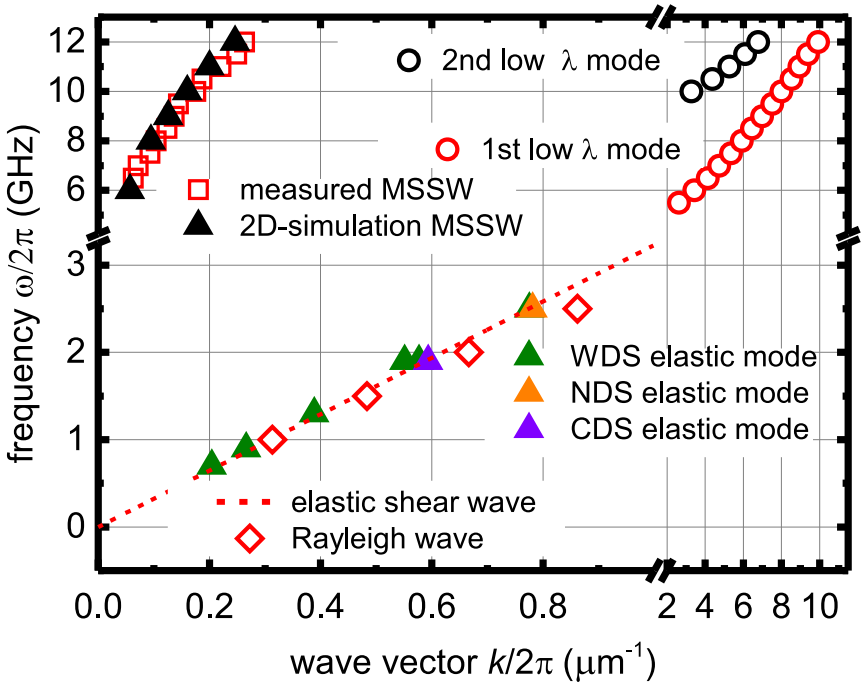

Figure 6.12: Dispersion map of spin wave and elastic wave modes of emission: The measured and simulated MSSW, two low λ-modes and domain-wall tied waves (elastic waves) for different domain states with the corresponding Rayleigh wave and elastic shear wave dispersion calculated for amorphous $Co_{40}Fe_{40}B_{20}$. This figure is a derivative of the figure published in [Holländer18] under the creative commons license.

as well, but they are calculated with a more realistic model considering the non-magnetic substrate and the geometry of the excitation.

6.5 Summary

In summary, multiple modes of emission by magnetic domain walls were investigated. The emission of MSSW can be understood via the Schlömann mechanism [Schlömann64] of spin wave excitation in non-homogeneous magnetic field. Also, low wavelength spin waves emitted by the domain walls were found in the simulation without an experimental counterpart due to optical limitations. An emission of elastic waves was found in a

lower frequency band. To fully understand the emission of elastic waves the elastodynamic equations were solved with FEM using the magnetic domain wall force as a local boundary load. The emission of spin waves and elastic waves is tunable via the excitation frequency and promises new excitation schemes for spin waves and elastic waves overcoming the need of small antennas or piezoelectric substrates.

7 Dynamics of Functional Magnetic Microstructures

7.1 Summary

Naturally, the occurrence of magnetic microstructures is correlated to local effective fields. By changing or modulating the inhomogeneous magnetization configuration with a time-dependent external magnetic field, the effective field is modulated or switched as well. A magnetic onion state (see Fig. 2.1) can be continuously moved by a rotating magnetic field. Since, the rotation of the magnetic field is sufficiently slow and the anisotropy low, the magnetization state follows the direction of the external field (discussed for an external field amplitude $H_{\mathrm{ext}} = 16\ \mathrm{kA/m}$ and a rotation frequency of $f \approx 0.5\ \mathrm{Hz}$). By embedding the magnetic disk structure in a fluid medium with superparamagnetic MBs, the motional response of the MBs on the external stimulus, rotating field and consequently rotating magnetization configuration of the disk parent structure, can be investigated. In this work an algorithm for an *all-numerical* analysis of the dynamic motional response of superparamagnetic MBs was developed. The algorithm starts with the calculation of the potential energy landscape of the MBs from the stray-field-distribution generated by the ferromagnetic disk and the magnetization distribution of the MB. Locally fitting the temporal and spatial dependence of the potential energy landscape then allows for the numerical solution of the equation of motion in adequate simulation time. The obtained numerical solutions were in excellent agreement with the experiment.

For the investigation of high frequency dynamics of magnetic microstructures, a specialized magneto-optical microscope was described. The pulsed laser illumination system of the setup enables stroboscopic measurements up to the GHz-regime. A new timing algorithm was implemented allowing for the correction of phase drifts occurring for long

measurement times. Furthermore, a two-axis motorized stage was integrated into the microscope setup unlocking the possibility of measuring dynamic in-plane magnetization vector response.

In order to engineer the magneto-dynamic response of a thin film and show bistable remanent states at zero-field, a thin film was patterned with diamond-shaped antidots in a rectangular lattice with a tilted anisotropy. The resulting functional microwave material has been investigated with static vector MOKE, SEM, PIMM, CW-FMR and time-resolved magneto-optical vector imaging. The bistable remanent states lead to different dynamic properties for different external magnetic field histories. The resulting PIMM spectra showed different maximum amplitude frequencies at a highly reproducible level and resonant frequencies close to the relevant frequency band at $2.4\ \mathrm{GHz}$. In order to disentangle the relevant dynamic processes, time-resolved magneto-optical vector imaging was applied to the sample exhibiting local dynamics governed by local resonance frequencies due to local effective fields of this functional magnetic microwave material.

Spin wave and elastic magnetization wave emission by domain walls were observed in magnetic stripe elements exhibiting multiple asymmetric Bloch domain walls. The emission of magnetostatic surface spin waves can be qualitatively understood by the Schlömann mechanism [Schlömann64]. The local effective fields induced by the inhomogeneous magnetization configuration lead to locally varying resonance frequencies resulting in a directional and coherent spin wave emission. Furthermore, an emission of elastic waves was found in a lower frequency band and was compared to the dispersion relation of the elastic shear wave using literature values for density and shear modulus. Also, in a more sophisticated approach the elastic wave emission could be modeled directly by using the micromagnetically obtained magnetization to calculate a local force and by using these forces as a boundary load in mechanical FEM simulations. All evidence points into the direction of an emission of elastic waves by the magnetic domain walls due to an elastic tensioning in the domain wall region.

7.2 Outlook

Dynamics of magnetic microstructures offer great flexibility and promise new applications. The motion of superparamagnetic MBs on ferromagnetic substrates provide a new reconfigurable platform for lab-on-a-chip applications such as magnetic flow-cytometry. Harvesting the energy of the looping motion occurring at higher frequencies by using magnetic field pulses or elliptical magnetic fields instead of rotating magnetic fields could lead to new fast transport mechanisms, ideally on a two-dimensional magnetic track. Programmable two-dimensional motion could lead to new functionalities, such as sorting of microbeads or magnetically labeled cells. The developed model is beneficial, since different structures and field sequences can be investigated as well. The implementation of an enhanced algorithm capable of solving the three dimensional equations of motion is work in progress.

Thin films with locally broken symmetry form a new area of application-oriented research towards the application in reconfigurable magnetic microwave devices. By using temperature annealing on patterned thin films, different domain states could be „imprinted“ into the material. Also, a combination with magnetic multilayer stacks exhibiting a tunable effective damping could provide more ability for functional reconfiguration. Furthermore, the proof of principle for symmetry broken thin films has been given, now an implementation in a device can be anticipated. A possible device architecture could involve a geometry, where the magnetic film is deposited between ground-plane and conducting stripline similar to the bandstop filter geometry used in [Kuanr03] leading to high attenuation.

Using magnetic domain walls as emitters of spin waves and elastic waves might have positive implications for future magnonic devices: First of all, magnetic domain walls occur naturally at zero external magnetic field. Since magnonic technology is a candidate as an example for low power consumption computing, it is only natural to use technology not relying on huge magnetic bias fields. Furthermore, the magnetic domain walls induce reasonable high local effective fields, which might be used not only to generate spin waves, but also as waveguides, delimiters or magnonic beam-splitters.
In contrast, the generation of elastic shear waves by magnetic domain walls might

simplify the excitation of phonon modes, which up to now require large interdigital transducers and piezoelectric substrates, in magnetic nano-strucutures. Elastic waves offer a simple possibility of inducing local magnetization dynamics. Also, elastic waves offer long propagation paths, when compared to spin waves. Furthermore, by injecting elastic waves into a material with a spin wave mode at lower frequencies, it should be possible to create propagating coupled magneto-elastic waves.

Due to the newly gained flexibility of the elastic wave excitation via domain walls, it is also possible to study the interaction of other magnetic microstructures with elastic waves with a high resolution in k-space.

7.3 Conclusion

The study of magnetic microstructures is a study of the local effective field. By engineering the local effective fields, as shown here with patterning, it will be possible to create new devices and research interesting physics, not accessible by magnetic fields solely created by electromagnets. The basic numerical algorithm for the calculation of the motional microbead response, is applicable to arbitrary problems consisting of microbeads on ferromagnetic surfaces. The time-resolved magneto-optical wide-field microscope provides a unique platform for interesting dynamic experiments. Symmetry broken magnetic thin films are ready for further investigations and device implementations. The emission of spin waves and elastic waves by domain walls is a new topic promising novel devices and physics. All in all, studying the dynamics of functional magnetic microstructures has been a successful and inspiring journey on the road of magnetism through different time scales.

Bibliography

[Abert13] C. Abert, L. Exl, F. Bruckner, A. Drews and D. Suess. *magnum.fe: A micromagnetic finite-element simulation code based on FEniCS*. Journal of Magnetism and Magnetic Materials, 345, Supplement C (2013), pp. 29 – 35. doi:10.1016/j.jmmm.2013.05.051. 11

[Abo13] G. S. Abo, Y. K. Hong, J. Park, J. Lee, W. Lee and B. C. Choi. *Definition of magnetic exchange length*. IEEE Transactions on Magnetics, 49, 8 (2013), pp. 4937–4939. doi:10.1109/TMAG.2013.2258028. 11

[Adam02] J. D. Adam, L. E. Davis, G. F. Dionne, E. F. Schloemann and S. N. Stitzer. *Ferrite devices and materials*. IEEE Transactions on Microwave Theory and Techniques, 50, 3 (2002), pp. 721–737. doi:10.1109/22.989957. 4, 69

[Aharoni96] A. Aharoni. *Introduction to the theory of ferromagnetism*. Oxford University Press (1996). 3, 12, 13, 15, 18, 28, 29, 34

[Alekseev99] A. M. Alekseev, H. Dötsch, N. E. Kulagin, A. F. Popkov and V. T. Synogach. *Microwave excitations of a domain wall in a cubic magnet with induced anisotropy*. Technical Physics, 44, 6 (1999), pp. 657–663. doi:10.1134/1.1259436. 97

[Alexander00] C. Alexander, J. Rantschler, T. J. Silva and P. Kabos. *Frequency- and time-resolved measurements of FeTaN films with longitudinal bias fields*. Journal of Applied Physics, 87, 9 (2000), pp. 6633–6635. doi:10.1063/1.372794. 75

[Argyle00] B. E. Argyle and J. G. McCord. *New laser illumination method for Kerr*

microscopy. Journal of Applied Physics, 87, 9 (2000), pp. 6487–6489. doi:10.1063/1.372746. 47

[Atalay15] S. Atalay, A. O. Kaya, V. S. Kolat, H. Gencer and T. Izgi. *One-dimensional magnonic crystal for magnetic field sensing*. Journal of Superconductivity and Novel Magnetism, 28, 7 (2015), pp. 2071–2075. doi:10.1007/s10948-015-3006-9. 6

[Bean59] C. P. Bean and J. D. Livingston. *Superparamagnetism*. Journal of Applied Physics, 30, 4 (1959), pp. S120–S129. doi:10.1063/1.2185850. 1, 29

[Beld15] W. T. E. van den Beld, N. L. Cadena, J. Bomer, E. L. de Weerd, L. Abelmann, A. van den Berg and J. C. T. Eijkel. *Bidirectional microfluidic pumping using an array of magnetic Janus microspheres rotating around magnetic disks*. Lab on a Chip, 15, 13 (2015), pp. 2872–2878. doi:10.1039/c5lc00199d. 2, 31

[Berkov93] D. V. Berkov, K. Ramstöck and A. Hubert. *Solving micromagnetic problems. Towards an optimal numerical method*. physica status solidi (a), 137, 1 (1993), pp. 207–225. doi:10.1002/pssa.2211370118. 9, 11, 13, 17, 23, 35

[Bhat13] V. Bhat, J. Woods, L. E. D. Long, J. T. Hastings, J. Sklenar, J. B. Ketterson and M. Pechan. *FMR study of Permalloy films patterned into square lattices of diamond antidots*. IEEE Transactions on Magnetics, 49, 3 (2013), pp. 1029–1032. doi:10.1109/TMAG.2012.2230157. 5, 79

[Bonetti15] S. Bonetti, R. Kukreja, Z. Chen, D. Spoddig, K. Ollefs, C. Schöppner, R. Meckenstock, A. Ney, J. Pinto, R. Houanche, J. Frisch, J. Stöhr, H. A. Dürr and H. Ohldag. *Microwave soft x-ray microscopy for nanoscale magnetization dynamics in the 5 -10 GHz frequency range*. Review of Scientific Instruments, 86, 9 (2015), p. 093703. doi:10.1063/1.4930007. 7

[Brown59] W. F. Brown. *Micromagnetics, domains, and resonance*. Journal of Applied Physics, 30, 4 (1959), pp. S62–S69. doi:10.1063/1.2185970. 9

[Chapman83] J. Chapman and G. Morrison. *Quantitative determination of magnetisation distributions in domains and domain walls by scanning transmission electron microscopy*. Journal of Magnetism and Magnetic Materials, 35, 1 (1983), pp. 254 – 260. doi:10.1016/0304-8853(83)90511-5. 7, 47

[Chapman90] J. N. Chapman, I. R. McFadyen and S. McVitie. *Modified differential phase contrast Lorentz microscopy for improved imaging of magnetic structures*. IEEE Transactions on Magnetics, 26, 5 (1990), pp. 1506–1511. doi:10.1109/20.104427. 7, 47

[Chen17] C. Chen, A. Barra, A. Mal, G. Carman and A. Sepulveda. *Voltage induced mechanical/spin wave propagation over long distances*. Applied Physics Letters, 110, 7 (2017), p. 072401. doi:10.1063/1.4975828. 6

[Chikazumi97] Chikazumi. *Physics of ferromagnetism*. Oxford University Press (1997). 1, 21

[Chumak15] A. V. Chumak, V. I. Vasyuchka, A. A. Serga and B. Hillebrands. *Magnon spintronics*. Nature Physics, 11, 6 (2015), pp. 453–461. doi:10.1038/nphys3347. 5, 6, 97

[Chumak17] A. V. Chumak, A. A. Serga and B. Hillebrands. *Magnonic crystals for data processing*. Journal of Physics D: Applied Physics, 50, 24 (2017), p. 244001. doi:10.1088/1361-6463/aa6a65. 6

[Chumakov05] D. Chumakov, J. McCord, R. Schäfer, L. Schultz, H. Vinzelberg, R. Kaltofen and I. Mönch. *Nanosecond time-scale switching of Permalloy thin film elements studied by wide-field time-resolved Kerr microscopy*. Physical Review B, 71 (2005), p. 014410. doi:10.1103/PhysRevB.71.014410. 54, 72

[Conca13] A. Conca, J. Greser, T. Sebastian, S. Klingler, B. Obry, B. Leven and B. Hillebrands. *Low spin-wave damping in amorphous $Co_{40}Fe_{40}B_{20}$ thin films*. Journal of Applied Physics, 113, 21 (2013), p. 213909. doi:10.1063/1.4808462. 19, 22

[Cowburn98] R. P. Cowburn, A. O. Adeyeye and M. E. Welland. *Configurational anisotropy in nanomagnets*. Physical Review Letters, 81 (1998), pp. 5414–5417. doi:10.1103/PhysRevLett.81.5414. 5

[Cramer00] N. Cramer, D. Lucic, R. E. Camley and Z. Celinski. *High attenuation tunable microwave notch filters utilizing ferromagnetic resonance*. Journal of Applied Physics, 87, 9 (2000), pp. 6911–6913. doi:10.1063/1.372883. 4, 69

[Davies16] C. S. Davies and V. V. Kruglyak. *Generation of propagating spin waves from edges of magnetic nanostructures pumped by uniform microwave magnetic field*. IEEE Transactions on Magnetics, 52, 7 (2016), pp. 1–4. doi:10.1109/TMAG.2016.2517000. 6

[Ding04] Y. Ding, T. J. Klemmer and T. M. Crawford. *A coplanar waveguide permeameter for studying high-frequency properties of soft magnetic materials*. Journal of Applied Physics, 96, 5 (2004), pp. 2969–2972. doi:10.1063/1.1774242. 69

[Donahue99] M. Donahue and D. Porter. *OOMMF User's Guide, Version 1.0*. Interagency Report NISTIR 6376, National Institute of Standards and Technology, Gaithersburg, MD (1999). 9

[Donolato11] M. Donolato, A. Torti, N. Kostesha, M. Deryabina, E. Sogne, P. Vavassori, M. F. Hansen and R. Bertacco. *Magnetic domain wall conduits for single cell applications*. Lab on a Chip, 11, 17 (2011), pp. 2976–83. doi:10.1039/C1LC20300B. 1

[Dzyaloshinsky58] I. Dzyaloshinsky. *A thermodynamic theory of „weak" ferromagnetism of antiferromagnetics*. Journal of Physics and Chemistry of Solids, 4, 4 (1958), pp. 241 – 255. doi:10.1016/0022-3697(58)90076-3. 3

[Ehresmann11] A. Ehresmann, D. Lengemann, T. Weis, A. Albrecht, J. Langfahl-Klabes, F. Gollner and D. Engel. *Asymmetric magnetization reversal of stripe-patterned exchange bias layer systems for controlled magnetic*

particle transport. Advanced Materials, 23, 46 (2011), pp. 5568–73. doi:10.1002/adma.201103264. 1

[Eickenberg13] B. Eickenberg, F. Wittbracht, P. Stohmann, J. R. Schubert, C. Brill, A. Weddemann and A. Hutten. *Continuous-flow particle guiding based on dipolar coupled magnetic superstructures in rotating magnetic fields*. Lab on a Chip, 13, 5 (2013), pp. 920–927. doi:10.1039/c2lc41316g. 2

[Fidler00] J. Fidler and T. Schrefl. *Micromagnetic modelling - the current state of the art*. Journal of Physics D: Applied Physics, 33, 15 (2000), p. R135. doi:10.1088/0022-3727/33/15/201. 11

[Fischer15] P. Fischer and H. Ohldag. *X-rays and magnetism*. Reports on Progress in Physics, 78, 9 (2015), p. 094501. doi:10.1088/0034-4885/78/9/094501. 7

[Foerster17] M. Foerster, F. Macià, N. Statuto, S. Finizio, A. Hernández-Mínguez, S. Lendínez, P. V. Santos, J. Fontcuberta, J. M. Hernàndez, M. Kläui and L. Aballe. *Direct imaging of delayed magneto-dynamic modes induced by surface acoustic waves*. Nature Communications, 8, 1 (2017), p. 407. doi:10.1038/s41467-017-00456-0. 6, 98

[Frommberger04] M. Frommberger, J. McCord and E. Quandt. *High-frequency properties of FeCoSiB thin films with crossed anisotropy*. IEEE Transactions on Magnetics, 40, 4 (2004), pp. 2703–2705. doi:10.1109/TMAG.2004.832139. 76

[Gijs04] M. A. M. Gijs. *Magnetic bead handling on-chip: new opportunities for analytical applications*. Microfluidics and Nanofluidics, 1, 1 (2004), pp. 22–40. doi:10.1007/s10404-004-0010-y. 31

[Gilbert04] T. L. Gilbert. *A phenomenological theory of damping in ferromagnetic materials*. IEEE Transactions on Magnetics, 40, 6 (2004), pp. 3443–3449. doi:10.1109/TMAG.2004.836740. 9, 23

[Graczyk17] P. Graczyk and M. Krawczyk. *Coupled-mode theory for the interaction between acoustic waves and spin waves in magnonic-phononic crystals:*

Propagating magnetoelastic waves. Physical Review B, 96, 2 (2017), p. 024407. doi:10.1103/PhysRevB.96.024407. 6, 110

[Harward14] I. Harward, R. E. Camley and Z. Celinski. *On-wafer magnetically tunable millimeter wave notch filter using M-phaseBa hexagonal ferrite/Pt thin films on Si*. Applied Physics Letters, 105, 17 (2014), p. 173503. doi:10.1063/1.4900519. 4, 69

[Helou13] M. Helou, M. Reisbeck, S. F. Tedde, L. Richter, L. Bar, J. J. Bosch, R. H. Stauber, E. Quandt and O. Hayden. *Time-of-flight magnetic flow cytometry in whole blood with integrated sample preparation*. Lab on a Chip, 13 (2013), pp. 1035–1038. doi:10.1039/C3LC41310A. 2

[Hengst14] C. Hengst, M. Wolf, R. Schäfer, L. Schultz and J. McCord. *Acoustic-domain resonance mode in magnetic closure-domain structures: A probe for domain-shape characteristics and domain-wall transformations*. Physical Review B, 89 (2014), p. 214412. doi:10.1103/PhysRevB.89.214412. 4

[Herzer97] G. Herzer. *Magnetic Hysteresis in Novel Magnetic Materials*. Springer, Dordrecht (1997). 4

[Heyderman06] L. J. Heyderman, F. Nolting, D. Backes, S. Czekaj, L. Lopez-Diaz, M. Kläui, U. Rüdiger, C. A. F. Vaz, J. A. C. Bland, R. J. Matelon, U. G. Volkmann and P. Fischer. *Magnetization reversal in cobalt antidot arrays*. Physical Review B, 73 (2006), p. 214429. doi:10.1103/PhysRevB.73.214429. 5

[Holländer17] R. B. Holländer, C. Müller, M. Lohmann, B. Mozooni and J. McCord. *Component selection in time-resolved magneto-optical wide-field imaging for the investigation of magnetic microstructures*. Journal of Magnetism and Magnetic Materials, 432 (2017), pp. 283 – 290. doi:10.1016/j.jmmm.2017.01.091. 7, 48, 51, 53, 55, 57, 59, 62, 64, 66

[Holländer18] R. B. Holländer, C. Müller, J. Schmalz, M. Gerken and J. McCord. *Magnetic domain walls as broadband spin wave and elastic magnetisation wave emitters*. Scientific Reports, 8, 1 (2018), p. 13871.

doi:10.1038/s41598-018-31689-8. 7, 98, 99, 100, 101, 103, 105, 106, 108, 109, 112, 114

[Hu11] X. K. Hu, S. Sievers, A. Müller, V. Janke and H. W. Schumacher. *Classification of super domains and super domain walls in permalloy antidot lattices*. Phys Rev B, 84 (2011), p. 024404. doi:10.1103/PhysRevB.84.024404. 5

[Hu15] X. Hu, R. Abedini-Nassab, B. Lim, Y. Yang, M. Howdyshell, R. Sooryakumar, B. B. Yellen and C. Kim. *Dynamic trajectory analysis of superparamagnetic beads driven by on-chip micromagnets*. Journal of Applied Physics, 118, 20 (2015), p. 203904. doi:10.1063/1.4936219. 2, 31, 36

[Hubert69] A. Hubert. *Stray-field-free magnetization configurations*. physica status solidi (b), 32, 2 (1969), pp. 519–534. 19

[Hubert08] A. Hubert and R. Schäfer. *Magnetic domains: the analysis of magnetic microstructures*. Springer Science & Business Media (2008). 3, 10, 13, 17, 18, 20, 22, 50, 51, 52, 56, 101

[Inoue11] M. Inoue, A. Baryshev, H. Takagi, P. B. Lim, K. Hatafuku, J. Noda and K. Togo. *Investigating the use of magnonic crystals as extremely sensitive magnetic field sensors at room temperature*. Applied Physics Letters, 98, 13 (2011), p. 132511. doi:10.1063/1.3567940. 6

[Kaidatzis16] A. Kaidatzis, R. P. del Real, R. Alvaro, J. L. Palma, J. Anguita, D. Niarchos, M. Vázquez, J. Escrig and J. M. García-Martín. *Magnetic properties engineering of nanopatterned cobalt antidot arrays*. Journal of Physics D: Applied Physics, 49, 17 (2016), p. 175004. doi:10.1088/0022-3727/49/17/175004. 5

[Kerr77] J. Kerr. *On rotation of the plane of polarization by reflection from the pole of a magnet*. The London, Edinburgh, and Dublin Philosophical Magazine and Journal of Science, 3, 19 (1877), pp. 321–343. doi:10.1080/14786447708639245. 48

[Khitun12] A. Khitun. *Multi-frequency magnonic logic circuits for parallel data processing*. Journal of Applied Physics, 111, 5 (2012), p. 054307. doi:10.1063/1.3689011. 6

[Kim01] S.-K. Kim, J. B. Kortright and S.-C. Shin. *Vector magnetization imaging in ferromagnetic thin films using soft X-rays*. Applied Physics Letters, 78, 18 (2001), pp. 2742–2744. doi:10.1063/1.1370120. 7, 47

[Kittel48] C. Kittel. *On the theory of ferromagnetic resonance absorption*. Physical Review, 73 (1948), pp. 155–161. doi:10.1103/PhysRev.73.155. 25

[Kittel49] C. Kittel. *Physical theory of ferromagnetic domains*. Reviews of Modern Physics, 21 (1949), pp. 541–583. doi:10.1103/RevModPhys.21.541. 21

[Korosi68] A. Korosi and B. M. Fabuss. *Viscosity of liquid water from 25 to 150 degree measurements in pressurized glass capillary viscometer*. Analytical Chemistry, 40, 1 (1968), pp. 157–162. doi:10.1021/ac60257a011. 37

[Kos02] A. B. Kos, T. J. Silva and P. Kabos. *Pulsed inductive microwave magnetometer*. Review of Scientific Instruments, 73, 10 (2002), pp. 3563–3569. doi:10.1063/1.1505657. 69, 70

[Kruglyak10] V. Kruglyak, S. Demokritov and D. Grundler. *Magnonics*. Journal of Physics D: Applied Physics, 43, 26 (2010), p. 264001. doi:10.1088/0022-3727/43/26/260301. 97

[Kuanr03] B. Kuanr, Z. Celinski and R. E. Camley. *Tunable high-frequency band-stop magnetic filters*. Applied Physics Letters, 83, 19 (2003), pp. 3969–3971. doi:10.1063/1.1625424. 4, 69, 119

[Kuanr05] B. K. Kuanr, I. R. Harward, R. T. Deiotte, R. E. Camley and Z. Celinski. *Magnetically tunable micro-strip band-stop filter: Design optimization and characterization*. Journal of Applied Physics, 97, 10 (2005), p. 10Q103. doi:10.1063/1.1853837. 4, 69

[Landau35] L. D. Landau and E. Lifshitz. *On the theory of the dispersion of magnetic permeability in ferromagnetic bodies*. Physikalische Zeitschrift der Sowjetunion, 8 (1935), p. 153. 9, 11

[Lenk11] B. Lenk, H. Ulrichs, F. Garbs and M. Münzenberg. *The building blocks of magnonics*. Physics Reports, 507, 4 (2011), pp. 107–136. doi:10.1016/j.physrep.2011.06.003. 97

[Li15] C. Li, G. Chai, C. Yang, W. Wang and D. Xue. *Tunable zero-field ferromagnetic resonance frequency from S to X band in oblique deposited CoFeB thin films*. Scientific Reports, 5 (2015), p. 17023. doi:10.1038/srep17023. 4, 69

[Liang14] C.-Y. Liang, S. M. Keller, A. E. Sepulveda, A. Bur, W.-Y. Sun, K. Wetzlar and G. P. Carman. *Modeling of magnetoelastic nanostructures with a fully coupled mechanical-micromagnetic model*. Nanotechnology, 25, 43 (2014), p. 435701. doi:10.1088/0957-4484/25/43/435701. 17

[Lim14] B. Lim, V. Reddy, X. Hu, K. Kim, M. Jadhav, R. Abedini-Nassab, Y.-W. Noh, Y. T. Lim, B. B. Yellen and C. Kim. *Magnetophoretic circuits for digital control of single particles and cells*. Nature Communications, 5 (2014), p. 3846. doi:10.1038/ncomms4846. 2, 31, 39

[Lohman17] M. Lohman, B. Mozooni and J. McCord. *Homogeneous microwave field emitted propagating spin waves: Direct imaging and modeling*. Journal of Magnetism and Magnetic Materials (2017). doi:10.1016/j.jmmm.2017.06.053. 6, 97

[Lord67] A. E. Lord. *Elastic wave radiation from simply-vibrating 180° magnetic domain walls*. Acta Acustica united with Acustica, 18, 4 (1967), pp. 187–192. 6

[M15] micromod M. *www.micromod.de* (2015). 38

[McCord15] J. McCord. *Progress in magnetic domain observation by advanced magneto-optical microscopy*. Journal of Physics D: Applied Physics,

48, 33 (2015), p. 333001. doi:10.1088/0022-3727/48/33/333001. 7, 47, 56, 57, 60

[Medina10] J. D. L. T. Medina, L. Piraux and A. Encinas. *Tunable zero field ferromagnetic resonance in arrays of bistable magnetic nanowires*. Applied Physics Letters, 96, 4 (2010), p. 042504. doi:10.1063/1.3295706. 4

[Middelhoek67] S. Middelhoek and D. Wild. *Review of Wall Creeping in Thin Magnetic Films*. IBM Journal of Research and Development, 11, 1 (1967), pp. 93–105. doi:10.1147/rd.111.0093. 1

[Moriya60] T. Moriya. *New Mechanism of Anisotropic Superexchange Interaction*. Physical Review Letters, 4 (1960), pp. 228–230. doi:10.1103/PhysRevLett.4.228. 3

[Mozooni14] B. Mozooni, T. von Hofe and J. McCord. *Picosecond wide-field magneto-optical imaging of magnetization dynamics of amorphous film elements*. Physical Review B, 90 (2014), p. 054410. doi:10.1103/PhysRevB.90.054410. 48, 51, 53, 61

[Mozooni15] B. Mozooni and J. McCord. *Direct observation of closure domain wall mediated spin waves*. Applied Physics Letters, 107, 4 (2015). doi:10.1063/1.4927598. 6, 48

[Mushenok17] F. B. Mushenok, R. Dost, C. S. Davies, D. A. Allwood, B. J. Inkson, G. Hrkac and V. V. Kruglyak. *Broadband conversion of microwaves into propagating spin waves in patterned magnetic structures*. Applied Physics Letters, 111, 4 (2017), p. 042404. doi:10.1063/1.4995991. 6, 97

[Néel88] L. Néel. *Selected Works of Louis Néel*. Gordon and Breach Science Publishers, New York London Paris Montreux Tokyo Melbourne (1988). 5, 79

[Neudecker06] I. Neudecker, G. Woltersdorf, B. Heinrich, T. Okuno, G. Gubbiotti and C. Back. *Comparison of frequency, field, and time domain ferromagnetic*

resonance methods. Journal of Magnetism and Magnetic Materials, 307, 1 (2006), pp. 148 – 156. doi:10.1016/j.jmmm.2006.03.060. 95

[Neudert05a] A. Neudert, J. McCord, D. Chumakov, R. Schäfer and L. Schultz. *Small-amplitude magnetization dynamics in Permalloy elements investigated by time-resolved wide-field Kerr microscopy*. Physical Review B, 71 (2005), p. 134405. doi:10.1103/PhysRevB.71.134405. 47

[Neudert05b] A. Neudert, J. McCord, R. Schäfer and L. Schultz. *Subnanosecond vortex transformation in ferromagnetic film elements observed by stroboscopic wide-field Kerr microscopy*. Journal of Applied Physics, 97, 10 (2005), p. 10E701. doi:10.1063/1.1850832. 47

[Nikitin15] A. A. Nikitin, A. B. Ustinov, A. A. Semenov, A. V. Chumak, A. A. Serga, V. I. Vasyuchka, E. Lähderanta, B. A. Kalinikos and B. Hillebrands. *A spin-wave logic gate based on a width-modulated dynamic magnonic crystal*. Applied Physics Letters, 106, 10 (2015), p. 102405. doi:10.1063/1.4914506. 6

[O'Handley00] R. C. O'Handley. *Modern magnetic materials: principles and applications*. John Wiley & Sons, Inc. (2000). 12, 13

[Oogane06] M. Oogane, T. Wakitani, S. Yakata, R. Yilgin, Y. Ando, A. Sakuma and T. Miyazaki. *Magnetic damping in ferromagnetic thin films*. Japanese Journal of Applied Physics, 45, 5R (2006), p. 3889. doi:10.1143/JJAP.45.3889. 4

[Oseen27] C. Oseen. *Neuere Methoden und Ergebnisse in der Hydrodynamik*. Akademische Verlagsgesellschaft m.b.H. (1927). 37

[Pankhurst03] Q. A. Pankhurst, J. Connolly, S. K. Jones and J. Dobson. *Applications of magnetic nanoparticles in biomedicine*. Journal of Physics D: Applied Physics, 36, 13 (2003), p. R167. doi:10.1088/0022-3727/36/13/201. 31

[Parkin90] S. S. P. Parkin, N. More and K. P. Roche. *Oscillations in exchange coupling and magnetoresistance in metallic superlattice structures:*

Co/Ru, Co/Cr, and Fe/Cr. Physical Review Letters, 64 (1990), pp. 2304–2307. doi:10.1103/PhysRevLett.64.2304. 3

[Parkin08] S. S. P. Parkin, M. Hayashi and L. Thomas. *Magnetic domain-wall racetrack memory*. Science, 320, 5873 (2008), pp. 190–194. doi:10.1126/science.1145799. 3

[Parkin15] S. Parkin and S.-H. Yang. *Memory on the racetrack*. Nature Nanotechnology, 10 (2015), p. 195. doi:10.1038/nnano.2015.41. 3

[Pechan01] M. J. Pechan, R. L. Compton, D. Bennett, L. C. Chen, C. J. Palmstrom and S. J. Allen. *Magnetic anisotropy and interlayer coupling in $Fe_{0.5}Co_{0.5}$(100) films on GaAs(100)*. Journal of Applied Physics, 89, 11 (2001), pp. 7514–7516. doi:10.1063/1.1354592. 11

[Pierce11] D. T. Pierce. *Perspective on probing metallic ferromagnetism with electrons (invited)*. Journal of Applied Physics, 109, 7 (2011), p. 07E106. doi:10.1063/1.3537960. 7, 47

[Pirro15] P. Pirro, T. Koyama, T. Brächer, T. Sebastian, B. Leven and B. Hillebrands. *Experimental observation of the interaction of propagating spin waves with Néel domain walls in a Landau domain structure*. Applied Physics Letters, 106, 23 (2015), p. 232405. doi:10.1063/1.4922396. 97

[Pivetal15] J. Pivetal, D. Royet, G. Ciuta, M. Frenea-Robin, N. Haddour, N. M. Dempsey, F. Dumas-Bouchiat and P. Simonet. *Micromagnet arrays for specific single bacterial cell positioning*. Journal of Magnetism and Magnetic Materials, 380 (2015), pp. 72–77. doi:10.1016/j.jmmm.2014.09.068. 1

[Queitsch06] U. Queitsch, J. McCord, A. Neudert, R. Schäfer, L. Schultz, K. Rott and H. Brückl. *Domain wall induced modes of high-frequency response in ferromagnetic elements*. Journal of Applied Physics, 100, 9 (2006), p. 093911. doi:10.1063/1.2365382. 4, 47

[Rave87] W. Rave, R. Schäfer and A. Hubert. *Quantitative observation of magnetic domains with the magneto-optical Kerr effect*. Journal

of Magnetism and Magnetic Materials, 65, 1 (1987), pp. 7 – 14. doi:10.1016/0304-8853(87)90304-0. 47

[Rave90] W. Rave and A. Hubert. *Refinement of the quantitative magnetooptic domain observation technique*. IEEE Transactions on Magnetics, 26, 5 (1990), pp. 2813–2815. doi:10.1109/20.104884. 47

[Rave93] W. Rave, P. Reichel, H. Brendel, M. Leicht, J. McCord and A. Hubert. *Progress in quantitative magnetic domain observation*. IEEE Transactions on Magnetics, 29, 6 (1993), pp. 2551–2553. doi:10.1109/20.280957. 47, 56

[Roy10] P. E. Roy, T. Trypiniotis and C. H. W. Barnes. *Micromagnetic simulations of spin-wave normal modes and the resonant field-driven magnetization dynamics of a* 360° *domain wall in a soft magnetic stripe*. Physical Review B, 82 (2010), p. 134411. doi:10.1103/PhysRevB.82.134411. 97

[Saib05] A. Saib, M. Darques, L. Piraux, D. Vanhoenacker-Janvier and I. Huynen. *Unbiased microwave circulator based on ferromagnetic nanowires arrays of tunable magnetization state*. Journal of Physics D: Applied Physics, 38, 16 (2005), p. 2759. doi:10.1088/0022-3727/38/16/003. 4, 69

[Sajjad17] U. Sajjad, R. B. Holländer, F. Klingbeil and J. McCord. *Magnetomechanics of superparamagnetic beads on a magnetic merry-go-round: from micromagnetics to radial looping*. Journal of Physics D: Applied Physics, 50, 13 (2017), p. 135003. doi:10.1088/1361-6463/aa5cef. 2, 15, 31, 32, 36, 40, 42, 43, 45

[Salahun02] E. Salahun, P. Quéffélec, G. Tanné, A.-L. Adenot and O. Acher. *Correlation between magnetic properties of layered ferromagnetic/dielectric material and tunable microwave device applications*. Journal of Applied Physics, 91, 8 (2002), pp. 5449–5455. doi:10.1063/1.1461066. 4, 69

[Sandler99] G. M. Sandler, H. N. Bertram, T. J. Silva and T. M. Crawford. *Determination of the magnetic damping constant in NiFe films*. Journal of

Applied Physics, 85, 8 (1999), pp. 5080–5082. doi:10.1063/1.370096. 75

[Scheinfein90] M. R. Scheinfein, J. Unguris, M. H. Kelley, D. T. Pierce and R. J. Celotta. *Scanning electron microscopy with polarization analysis (SEMPA)*. Review of Scientific Instruments, 61, 10 (1990), pp. 2501–2527. doi:10.1063/1.1141908. 7, 47

[Schlömann64] E. Schlömann. *Generation of spin waves in nonuniform magnetic fields. I. conversion of electromagnetic power into spin wave power and vice versa*. Journal of Applied Physics, 35, 1 (1964), pp. 159–166. doi:10.1063/1.1713058. 104, 114, 118

[Schoenstein05] F. Schoenstein, P. Aublanc, H. Pagès, S. Queste, V. Barentin, A.-L. Adenot, N. Malléjac and O. Acher. *Influence of the domain structure on the microwave permeability of soft magnetic films and multilayers*. Journal of Magnetism and Magnetic Materials, 292, Supplement C (2005), pp. 201 – 209. doi:10.1016/j.jmmm.2004.10.113. 4

[Serga10] A. A. Serga, A. V. Chumak and B. Hillebrands. *YIG magnonics*. Journal of Physics D: Applied Physics, 43, 26 (2010), p. 264002. doi:10.1088/0022-3727/43/26/264002. 6

[Shampine97] L. Shampine and M. Reichelt. *The MATLAB ODE Suite*. SIAM Journal on Scientific Computing, 18, 1 (1997), pp. 1–22. doi:10.1137/S1064827594276424. 38

[Shampine99] L. Shampine, M. Reichelt and J. Kierzenka. *Solving Index-1 DAEs in MATLAB and Simulink*. SIAM Review, 41, 3 (1999), pp. 538–552. doi:10.1137/S003614459933425X. 38

[Shimokhin91] I. A. Shimokhin. *On the Gilinskii branch of the spectrum of excitations of a domain wall in uniaxial ferromagnetics*. physica status solidi (b), 167, 1 (1991), pp. 243–250. doi:10.1002/pssb.2221670126. 97

[Silva99] T. J. Silva, C. S. Lee, T. M. Crawford and C. T. Rogers. *Inductive measurement of ultrafast magnetization dynamics in thin-film permal-*

loy. Journal of Applied Physics, 85, 11 (1999), pp. 7849–7862. doi:10.1063/1.370596. 26, 70, 74

[Silverman90] M. P. Silverman and J. Badoz. *Light reflection from a naturally optically active birefringent medium*. Journal of the Optical Society of America A, Optics and Image Science, 7, 7 (1990), pp. 1163–1173. doi:10.1364/JOSAA.7.001163. 104

[Soldatov17] I. V. Soldatov and R. Schäfer. *Selective sensitivity in Kerr microscopy*. Review of Scientific Instruments, 88, 7 (2017), p. 073701. doi:10.1063/1.4991820. 47

[Song09] Y.-Y. Song, C. L. Ordóñez-Romero and M. Wu. *Millimeter wave notch filters based on ferromagnetic resonance in hexagonal barium ferrites*. Appl. Phys. Lett., 95, 14 (2009), p. 142506. doi:10.1063/1.3246170. 4, 69

[Stancil09] D. D. Stancil and A. Prabhakar. *Spin waves - theory and applications*. Springer US (2009). 23, 26, 27

[Stoner48] E. Stoner and E. Wohlfarth. *A mechanism of magnetic hysteresis in heterogeneous alloys*. Philosophical Transactions of the Royal Society of London A: Mathematical, Physical and Engineering Sciences, 240, 826 (1948), pp. 599–642. doi:10.1098/rsta.1948.0007. 14

[Sun02] N. X. Sun, S. X. Wang, T. J. Silva and A. B. Kos. *High-frequency behavior and damping of FeCoN-based high-saturation soft magnetic films*. IEEE Transactions on Magnetics, 38, 1 (2002), pp. 146–150. doi:10.1109/TMAG.2002.988927. 24, 25

[Trützschler16] J. Trützschler, K. Sentosun, B. Mozooni, R. Mattheis and J. McCord. *Magnetic domain wall gratings for magnetization reversal tuning and confined dynamic mode localization*. Scientific Reports, 6 (2016), p. 30761. doi:10.1038/srep30761. 6, 97

[Tsai99] C. S. Tsai, J. Su and C. C. Lee. *Wideband electronically tunable microwave bandstop filters using iron film-gallium arsenide waveguide*

structure. IEEE Transactions on Magnetics, 35, 5 (1999), pp. 3178–3180. doi:10.1109/20.801120. 4, 69

[Tsai05] C. S. Tsai, G. Qiu, H. Gao, L. W. Yang, G. P. Li, S. A. Nikitov and Y. Gulyaev. *Tunable wideband microwave band-stop and band-pass filters using* YIG / GGG - GaAs *layer structures*. IEEE Transactions on Magnetics, 41, 10 (2005), pp. 3568–3570. doi:10.1109/TMAG.2005.855191. 4, 69

[Urs16] N. O. Urs, B. Mozooni, P. Mazalski, M. Kustov, P. Hayes, S. Deldar, E. Quandt and J. McCord. *Advanced magneto-optical microscopy: Imaging from picoseconds to centimeters - imaging spin waves and temperature distributions (invited)*. AIP Advances, 6, 5 (2016), p. 055605. doi:10.1063/1.4943760. 47

[Vansteenkiste14] A. Vansteenkiste, J. Leliaert, M. Dvornik, M. Helsen, F. Garcia-Sanchez and B. V. Waeyenberge. *The design and verification of mumax3*. AIP Advances, 4, 10 (2014), p. 107133. doi:10.1063/1.4899186. 9, 11, 13, 23, 35

[Vavassori02] P. Vavassori, G. Gubbiotti, G. Zangari, C. T. Yu, H. Yin, H. Jiang and G. J. Mankey. *Lattice symmetry and magnetization reversal in micron-size antidot arrays in permalloy film*. Journal of Applied Physics, 91, 10 (2002), pp. 7992–7994. doi:10.1063/1.1453321. 5

[Wagner16] K. Wagner, A. Kákay, K. Schultheiss, A. Henschke, T. Sebastian and H. Schultheiss. *Magnetic domain walls as reconfigurable spin-wave nanochannels*. Nature Nanotechnology, 11, 5 (2016), pp. 432–436. doi:10.1038/nnano.2015.339. 6, 97

[Wang15] X. guang Wang, G. hua Guo, Z. xiong Li, D. wei Wang, Y. zhuang Nie and W. Tang. *Spin-wave propagation in domain wall magnonic crystal*. Europhysics Letters, 109, 3 (2015), p. 37008. doi:10.1209/0295-5075/109/37008. 6

[Weiler11] M. Weiler, L. Dreher, C. Heeg, H. Huebl, R. Gross, M. S. Brandt and S. T. B. Goennenwein. *Elastically driven ferromagnetic resonance*

in nickel thin films. Physical Review Letters, 106 (2011), p. 117601. doi:10.1103/PhysRevLett.106.117601. 98

[Whitehead17] N. J. Whitehead, S. A. R. Horsley, T. G. Philbin, A. N. Kuchko and V. V. Kruglyak. *Theory of linear spin wave emission from a Bloch domain wall*. Physical Review B, 96 (2017), p. 064415. doi:10.1103/PhysRevB.96.064415. 97

[Wiele16] B. Van de Wiele, S. J. Hämäläinen, P. Baláž, F. Montoncello and S. van Dijken. *Tunable short-wavelength spin wave excitation from pinned magnetic domain walls*. Scientific Reports, 6 (2016), p. 21330. doi:10.1038/srep21330. 6, 97

[Winter61] J. M. Winter. *Bloch wall excitation. Application to nuclear resonance in a Bloch wall*. Physical Review, 124, 2 (1961), pp. 452–459. doi:10.1103/PhysRev.124.452. 6, 97

[Wintz16] S. Wintz, V. Tiberkevich, M. Weigand, J. Raabe, J. Lindner, A. Erbe, A. Slavin and J. Fassbender. *Magnetic vortex cores as tunable spin-wave emitters*. Nature Nanotechnology, 11, 11 (2016), pp. 948–953. doi:10.1038/nnano.2016.117. 6, 97

[Yang15a] S.-H. Yang, K.-S. Ryu and S. Parkin. *Domain-wall velocities of up to 750 m/s driven by exchange-coupling torque in synthetic antiferromagnets*. Nature Nanotechnology, 10 (2015), p. 221. doi:10.1038/nnano.2014.324. 3

[Yang15b] X. Yang, M. Liu, B. Peng, Z. Y. Zhou, T. X. Nan, H. J. Sun and N. X. Sun. *A wide-band magnetic tunable bandstop filter prototype with FeGaB / Al_2O_3 multilayer films*. Applied Physics Letters, 107, 12 (2015), p. 122408. doi:10.1063/1.4931757. 4, 69

Acknowledgments

- At first I would like to thank Prof. Dr.-ing. Jeffrey McCord for supervising my thesis throughout different times. I'm truly thankful for my amazing time in his group and everything that I learned during my years in Kiel. I want to express my huge gratitude for his advice, support and understanding.
- I thank Prof. Dr. Martina Gerken and Julius Schmalz for the mechanical FEM simulations on the elastic wave emission by magnetic domain walls.
- Also, I want to thank Prof. Dr.-Ing. Eckhard Quandt and his group for their expertise and depositing my FeCoSiB samples. Especially, I want to thank Dr. Dirk Meyners and Dr.-ing. Christine Kirchhof.
- I thank Dr. Roland Mattheis for thin film preparation and Dr. Ingolf Mönch for help with the sample preparation of the CoFeB stripes.
- I want to thank Dr.-ing. Enno Lage, Dr.-ing. Onur Urs, Cai Müller, Umer Sajjad and Finn Klingbeil for their invaluable inputs to my thesis.
- I thank Dr.-ing. Enno Lage for his experienced advice, support and his humor.
- I thank Dr.-ing. Onur Urs for his experience, his constant support and his kindness.
- I thank Cai Müller for his always present assistance, his open and broad mind, which I learned to appreciate a lot, TR-MOKEing together and so much more.
- I thank Finn Klingbeil for his persistence, intelligence and his great support on the microbeads project.
- I thank Umer Sajjad for the experimental results on the microbead motion, his help on the sample fabrication, his insights and many nice discussions.

- I thank Babak Mozooni for introducing me to TR-MOKE.
- I thank Farzaneh Karimian for her good mood and many questions.
- I want to thank my (former) colleagues Matic Jovičević Klug, Simon Jarausch, Findan Block, Fasheng Qiu and Julia Trützschler for their countless help and having an amazing time.
- Also, I want to thank the master and bachelor students Mathis Lohmann, Robert Veith, Frederik Woltering, Finn Klingbeil and Findan Block for their valuable results and having a great time.
- I thank Sandra Robien for her help and advice in and around the lab.
- Furthermore, I want to thank Matthias Burmeister, Berndt Neumann and the workshop staff for everything they prepared for my work, their precision and experience.
- The funding by the German Research Council(DFG, grant no. MC9/15-1, grant no. MC9/10-2 and Collaborative Research Center CRC 1261) is greatly acknowledged.
- I want to thank my (non-magnetic) friends, who always supported me: my Kiel people Jens Nielsen, Sören Nielsen, Elena Nielsen, Andy Hansen, Bastian Bossen, Nico Gaida and Momme Thomsen, my Munich people Marc Wüstrich, Patrick Kilian, Hendrik Fink, Mathias Block, Christopher Husmann and family Fuchs, my Flensburg people Marlon Schlotfeldt and Johnlef Kösterke, my Hamburg people Martin Hansen and Ove Thomsen and finally my Montreal people Felix Fuchs and Stephanie Shousha.
- At the end I want to thank my parents and my sisters. I'm happy for having such a great and supportive family.
- I want to thank anybody, who did not make it into this list. Please accept my best thanks.

Thank you for your support.